TECHNISCHE
UNIVERSITÄT
DRESDEN

Fakultät Maschinenwesen Institut für Werkstoffwissenschaft

Professur Materialwissenschaft und Nanotechnologie

SIMULATION OF ELECTRIC FIELD-ASSISTED NANOWIRE GROWTH FROM AQUEOUS SOLUTIONS

DISSERTATION

zur Erlangung des akademischen Grades

Doktoringenieur (Dr.-Ing.)

vorgelegt

der Fakultät Maschinenwesen

der Technischen Universität Dresden

von

Dip.-Ing. Markus Pötschke

geboren am 09.05.1985 in Dresden

Tag der Einreichung	26.09.2014
Tag der Verteidigung	04.06.2015
Erster Gutachter	Herr Prof. Dr. rer. nat. G. Cuniberti, TU Dresden
Zweiter Gutachter	Herr Prof. Dr. R. M. Metzger, Univ. of Alabama
Vorsitzender der Promotionskommision	Herr Prof. Dr.-Ing. habil M. Gude, TU Dresden

ERKLÄRUNG

a) Hiermit versichere ich, dass ich die vorliegende Arbeit ohne unzulässige Hilfe Dritter und ohne Benutzung anderer als der angegebenen Hilfsmittel angefertigt habe; die aus fremden Quellen direkt oder indirekt übernommenen Gedanken sind als solche kenntlich gemacht.

b) Bei der Auswahl und Auswertung des Materials sowie bei der Herstellung des Manuskripts habe ich Unterstützungsleistungen von folgenden Personen erhalten:

   - Dr. Arezoo Dianat (Abschnitt 2.7.1)
   - Dr. Alexander Nerowski (Abschnitte 2.3.3 und 2.7.3)

   Weitere Personen waren an der geistigen Herstellung der vorliegenden Arbeit nicht beteiligt. Insbesondere habe ich nicht die Hilfe eines kommerziellen Promotionsberaters in Anspruch genommen. Dritte haben von mir keine geldwerten Leistungen für Arbeiten erhalten, die in Zusammenhang mit dem Inhalt der vorgelegten Dissertation stehen.

c) Die Arbeit wurde bisher weder im Inland noch im Ausland in gleicher oder ähnlicher Form einer anderen Prüfungsbehörde vorgelegt und ist auch noch nicht veröffentlicht worden.

d) Die Promotionsordnung der Fakultät Maschinenwesen an der TU Dresden vom 01.07.2001 wird anerkannt.

KURZFASSUNG

Ziel der vorliegenden Arbeit ist es, mittels physikalischer und chemischer Modelle die Mechanismen des Nanodrahtwachstums aus wässrigen Lösungen zu erforschen und daraus eine optimierte Prozesskontrolle abzuleiten. Dabei werden zwei Verfahren des Nanodrahtwachstums näher betrachtet: Dies sind die dielektrophoretische Assemblierung von neutralen Molekülen oder Metallclustern sowie die gerichtete elektrochemische Nanodrahtabscheidung (engl. directed electrochemical nanowire assembly), bei der metallhaltige Ionen im elektrischen Wechselfeld an der Nanodrahtspitze zunächst reduziert und anschließend als Metallatome abgeschieden werden.

Zur Beschreibung der Transport- und Wachstumsprozesse werden Kontinuumsmodelle eingesetzt. Darüber hinaus hat es sich als notwendig erwiesen, elektrokinetische Fluidströmungen zu berücksichtigen, um die experimentellen Beobachtungen zu reproduzieren. Die auftretenden partiellen Differenzialgleichungen werden mittels der Finiten Elemente Methode (FEM) numerisch gelöst.

Die Auswirkungen der Prozessparameter auf das Nanodrahtwachstum werden durch den Vergleich von experimentellen Ergebnissen mit Parameterstudien analysiert. Die Auswertung hat ergeben, dass für das dielektrophoretische Wachstum ein durch Wechselfeldelektroosmose (engl. AC electro-osmosis) angetriebener Fluidstrom die Drahtwachstumsgeschwindigkeit und -morphologie maßgeblich beeinflusst. Im Falle der gerichteten elektrochemischen Nanodrahtabscheidung lässt sich die Drahtmorphologie über das angelegte elektrische Wechselsignal steuern. Unter Verwendung des Wachstumsmodells ist ein optimiertes Signal generiert worden, dessen Parametrisierung eine gezielte Anpassung auf den chemischen Ausgangsstoff und den gewünschten Drahtdurchmesser erlaubt.

ABSTRACT

The present work is aimed at investigating the mechanisms of nanowire growth from aqueous solutions through a physical and chemical modeling. Based on this modeling, deriving an optimized process control is intended. The work considers two methods of nanowire growth. The first is the dielectrophoretic nanowire assembly from neutral molecules or metal clusters. Secondly, in the directed electrochemical nanowire assembly metal-containing ions are reduced in an AC electric field in the vicinity of the nanowire tip and afterwards deposited at the nanowire surface.

To describe the transport and growth processes, continuum models are employed. Furthermore, it has been necessary to consider electro-kinetic fluid flows to match the experimental observations. The occurring partial differential equations are solved numerically by means of finite element method (FEM).

The effect of the process parameters on the nanowire growth are analyzed by comparing experimental results to a parameter study. The evaluation has yielded that an AC electro-osmotic fluid flow has a major influence on the dielectrophoretic nanowire assembly regarding the growth velocity and morphology. In the case of directed electrochemical nanowire assembly, the nanowire morphology can be controlled by the applied AC signal shape. Based on the nanowire growth model, an optimized AC signal has been designed, whose parametrization allows to adjust to the chemical precursor and the desired nanowire diameter.

TABLE OF CONTENTS

LIST OF FIGURES

LIST OF TABLES

LIST OF SYMBOLS

A		surface area.
	A_d	cross-section area of a one-dimensional system with a dimension factor d.
	A_i	area of ith finite element triangle.
α		polarizability.
	α_0	electronic polarizability.
B		constant in Vogel–Fulcher–Tammann equation.
β		dimensionless coefficient describing the charge density.
C		total capacity; constant in Vogel–Fulcher–Tammann equation.
	C_l	capacity of Stern layer.
c		concentration of neutral particles, i.e. metal clusters or neutral complexes.
	c_0	initial concentration.
	c_1	cation concentration.
	c_2	anion concentration.
	c_a1	concentration of metal-rich anions.
	c_a2	concentration of metal-free anions.
	c_b	bulk concentration.
	c_cl	concentration of chloride ions.
	c_max	maximum ion concentration.

	c_x	concentration of $[\mathrm{PtCl}_x(\mathrm{H_2O})_{4-x}]^{2-x}$-species.
χ		dimensionless coefficient describing the body force.
D		diffusion coefficient.
	D_i	diffusion coefficient of *i*th concentration species.
d		thickness of Stern layer; dimension factor.
	d_w	nanowire diameter.
δ		crowding layer thickness.
ΔG_r		reaction free enthalpy.
	ΔG_r^0	reaction free enthalpy under standard conditions.
E		electric field strength.
	E_A	activation energy.
	E_A^0	activation energy in the absence of an electric field.
	$\mathbf{E}$	electric field vector.
	E_c	critical electric field.
	E_max	maximal occurring electric field.
	E_φ	tangential component of the electric field.
	E_t	electric field threshold.
	E_z	axial component of the electric field.
e		Elementary charge.
	$\mathbf{e}_i$	*i*th unit vector of the global coordinate system.
ε		electric permittivity.
	ε_0	electric permittivity of vacuum.
	ε_l	electric permittivity of Stern layer.
	ε_r	relative electric permittivity of the solution.
η		dynamic viscosity; axis in a local coordinate system.
	η_0	viscosity constant in Vogel–Fulcher–Tammann equation.
F		Faraday constant.

f	frequency.
$\mathbf{f}$	body force vector.
f_z	z-component of the body force.
γ	dimensionless coefficient describing the diffusion.
G_B	binding free enthalpy.
h	typical length scale of a mesh.
h_d	homogeneous solution of Laplace equation in a one-dimensional system with a dimension factor d.
i	index variable.
$\imath$	imaginary unit.
j	particle flux.
$\mathbf{j}$	particle flux vector of neutral particles, i.e. metal clusters or neutral complexes.
$\mathbf{j}_1$	cation particle flux.
$\mathbf{j}_2$	anion particle flux.
$\mathbf{j}_\mathrm{a1}$	particle flux of metal-rich anions.
$\mathbf{j}_\mathrm{a2}$	particle flux of metal-free anions.
K	Clausius–Mosotti factor.
k	index variable; geometric scaling factor.
k_B	Boltzmann constant.
k_r	reaction rate constant.
k_x	xth reaction rate constant; notational abbreviation.
k'_x	backward reaction rate constant to k_x.
κ	dimensionless coefficient describing the fluid viscosity.
l	index variable.
ℓ_B	Bjerrum length.
ℓ	nanowire length; characteristic system length; displacement length; length of finite element.

	$\ell_{\max}$	maximal length of finite element.
	$\ell_{\min}$	minimal length of finite element.
λ	characteristic length scale of the double layer potential drop.	
	λ_{D}	Debye length.
	λ_{D}^{*}	Debye length at maximum ion concentration.
M	mobility.	
m_{Pt}	atomic mass of platinum.	
μ	chemical potential; dipole moment.	
	μ_1	chemical potential of cations.
	μ_2	chemical potential of anions.
	μ_{a1}	chemical potential of metal-rich anions.
	μ_{a2}	chemical potential of metal-free anions.
N	number of time steps per half period.	
	N_{τ}	number of time steps per period.
	N_{x}	number of line segments.
n	number of Fourier modes.	
	$\mathbf{n}$	normal vector (outward oriented).
Ω	overall simulation domain.	
	$\partial\Omega$	domain boundary of the overall simulation domain.
	Ω_{B}	bulk zone, i.e. complement to the electrochemical double layer.
	Ω_{I}	inner layer of the electrochemical double layer.
	Ω_{O}	outer layer of the electrochemical double layer.
	Ω_{s}	overall domain of the electrochemical double layer.
ω	angular frequency.	
	ω_{p}	characteristic ion relocation frequency.
	ω_{T1}	lower transition frequency which marks the transition to quasi-static behavior.
	ω_{T2}	upper transition frequency associated to the charge relaxation time.

p		pressure.
φ		electric potential.
	$\hat{\varphi}$	normalized electric potential.
	φ_{asym}	asymptotic electric potential in the bulk zone of the electrolyte.
	φ_{c}	critical potential.
ψ		generic external potential.
	ψ_{DEP}	dielectric potential.
Q		total amount of charge in the electrochemical double layer.
	Q_0	charge on the nanowire electrode.
q		factor in the geometric sequence of finite element tiling.
r		radius coordinate.
	r_0	integration constant.
	r_1	radius of nanoelectrode; nanowire radius.
	r_2	radius of the counter-electrode.
	r_{b1}	double layer cut-off radius near the nanoelectrode.
	r_{b2}	double layer cut-off radius near the counter-electrode.
	r_{c}	radius of the critical potential.
	r_{d}	desired nanowire radius.
	r_{s}	radius of the depletion volume.
Re		Reynold's number.
ρ		charge density.
	ρ_{m}	mass density.
	ρ_{Pt}	mass density of platinum.
T		absolute temperature.
	$\mathcal{T}$	period time, reciprocal frequency.
t		time.
	Δt	rising time.

	Δt_{t}	threshold holding time.
τ		time step for numerical simulation.
u		generic ansatz function.
	u^{n+1}	current function value of u.
	δu	prediction error of the future function value of u.
	u^{n+1}	actual future function value of u.
	$\widehat{u}^{n+1}$	an estimation of the future function value of u.
	u_i	nodal values of u.
	$u_{i,k}$	nodal values of u.
V		voltage.
	V_0	voltage amplitude.
	V_{d}	voltage drop caused by the electrochemical double layer.
	V_{o}	offset-voltage caused by the electrochemical double layer.
	V_{p}	particle volume.
	V_{Pt}	Volume of a platinum atom in solid conditions.
	V_{s}	volume of particle-depleted solution.
	V_{t}	threshold voltage.
	V_{w}	nanowire volume.
v		fluid velocity.
	$\mathbf{v}$	fluid velocity vector.
	v_{g}	nanowire growth velocity.
	v_i	ith component of the fluid velocity.
	v_{r}	radial component of the fluid velocity.
	v_{z}	axial component of the fluid velocity.
w		test function.
	w_{c_i}	test function associated to c_i.
	w_{p}	test function associated to p.

	w_{φ}	test function associated to φ.
	w_{v_i}	test function associated to v_i.
$\mathbf{x}$	position vector in global coordinates.	
	x_{k}	node coordinates.
Ξ	generic PDE function.	
ξ	axis in a local coordinate system.	
z	absolute charge number; axial axis in cylinder coordinate system.	
	z_1	cation charge number.
	z_2	anion charge number.

LIST OF ABBREVIATIONS

AC	alternating current.
ACEO	AC electro-osmosis.
CP2K	molecular dynamics and density function theory software.
DC	direct current.
DENA	directed electrochemical nanowire assembly.
DEP	dielectrophoresis.
EDDS	ethylenediamine-N,N′-disuccinic acid.
EDTA	ethylenediaminetetraacetic acid.
FEM	finite element method.
MO	molecular orbital.
NEFEM	NURBS enhanced finite element method.
NTA	nitrilotriacetic acid.
NURBS	non uniform rational B-splines.
ODE	ordinary differential equation.
PDE	partial differential equation.
PNP	Poisson–Nernst–Planck equation.
RMS	root mean square value.

1 INTRODUCTION

1.1 MOTIVATION

“Nanowires are extremely thin wires with a diameter on the order of a few nanometers and with lengths orders of magnitude larger than its diameter” [1]. Such nanowires have been fabricated from metallic [2] and semi-conducting [3] materials. In the recent past, particularly *metallic* nanowires have attracted great interest due to their versatile applications in optical and electronic devices, and particularly in sensing. Examples of successful applications include optical resonators [4, 5], electrical interconnects [6–8], gas sensors [9–11], chemical sensors [12–14], and biochemical sensors [15]. Additionally, by oxidization of for example copper or indium nanowires, it is possible to convert metallic nanowires to semi-conducting nanowires as well [16, 17].

Nanostructures in general and nanowires in particular offer a strikingly large surface to volume ratio. This makes the application of nanowires as sensors exceptionally favorable, because the sensing happens at the interface of the functionalized nanowire and the environment. Likewise, sensor structures on the nanoscale allow the detection of even traces of an analyte [18], due to very few molecules at the wire interface having a recognizable effect on the electric properties of the device. Moreover, the demand for mobile sensing solutions, where weight but also power consumption play a crucial role, drives the ongoing miniaturization process. The utilization of nanowires for this purpose has the advantage that they can be arranged as an array, where each nanowire has a different functionalization and is thus capable of detecting different analytes. Such highly integrated devices can be employed when the sample size is extremely small.

Historically, *metallic* nanowires were first accessible from photolithographic methods [11, 19, 20]. In this class of manufacturing processes, a substrate is coated with photoresist and afterwards selectively exposed with photons or electrons. In a developing step either the exposed (positive resist) or the unexposed (negative resist) areas of the photo resist are dissolved. Then, in a physical vapor deposition process, the patterned photoresist is covered by a thin metallic layer. In the subsequent lift-off step the remaining photoresist

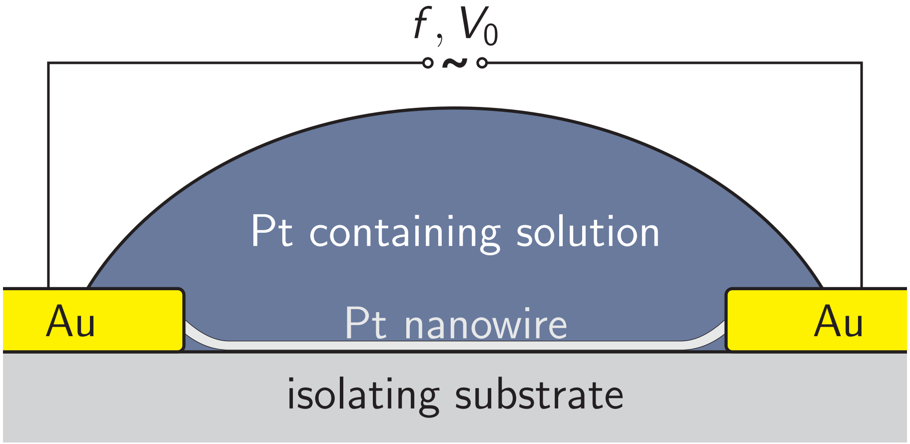

Figure 1.1: Schematic experimental setup for growing nanowires from a solution. In the dielectrophoretic nanowire assembly, a solution containing metal clusters or metal-containing neutral complexes is employed. The directed electrochemical nanowire assembly requires a solution of metallic cations or complex anions with a metallic center. The lithographically prepared gold electrodes have a gap distance of a few µm. Upon applying an AC voltage to the electrodes, nanowires grow in typically less than a minute.

is dissolved, which mechanically removes that part of the metal layer that is not in direct contact with the substrate.

Optical and electron-beam lithography belong to the group of top-down processes, in which a nanoscale structure is crafted from a macroscopic object like a wafer. In contrast, the methods described in the following are from the group of bottom-up techniques, in which the nanostructures are generated by the controlled assembly of even smaller building blocks.

A well-established bottom-up nanowire synthesis is the dielectrophoretic assembly of metal-containing, electrically neutral complexes [21] or metal clusters [22, 23] from an aqueous solution. To grow nanowires, a substrate with two electrodes is covered in drop of such a solution and an AC voltage is applied to the electrodes, cf. Figure 1.1. Due to the inhomogeneity of the electric field between the electrodes, a dielectrophoretic (DEP) force [24] arises, which attracts the polarizable metal clusters or complexes to the electrodes. The metal clusters or complexes, arriving at the electrode, nucleate and form the wire. With this technique a large number of nanowires grow in parallel on the substrate from electrode to electrode. However, Bhatt and Velev [23] found that under certain experimental conditions also free-standing volume-wires grow.

For the directed electrochemical nanowire assembly (DENA) a similar electrode setup as that used for dielectrophoretic nanowire assembly is employed (Figure 1.1), but with a different solution, i.e. one that contains metallic cations [2, 25] or complex anions with a metallic center [26]. After applying an AC voltage to the electrodes, an electrochemical reaction converts the metal-containing ions to metal, which is deposited as nanowires.

Additionally, further techniques have been developed to grow *metallic* nanowires. In template-based nanowire synthesis, nanowires are grown at existing nanostructures of similar size and shape. These templates can be macromolecules like DNA [27] and polypeptides [28] but may also be fabricated using a top-down approach [29, 30]. In a similar fashion, thin metallic wires can be grown at step edges of vicinal surfaces by a chemical vapor deposition (CVD) process [31, 32]. Unfortunately, these ultrathin nanowires cannot be removed from the surfaces on which they are deposited [33], which hinders their technical application. Furthermore, Shui and Li [34] demonstrated the production of tangles of platinum nanowires by means of electrospinning.

For mass-market application of nanowires, a fast, high-yield, and foremost cheap way of manufacturing nanowires and integrating them into devices is needed. Lithographic methods provide an excellent control over the positioning and geometry of the fabricated nanowires. Also a wide range of materials, including semiconductors, is available for the manufacturing process. However, to generate nanostructures with optimal resolution, electron beams have to be used in the exposure step. This process has an extremely low throughput and requires expensive equipment and hence the fabricated nanowires are costly.

The nanowire synthesis from molecular templates and electrospinning has a high throughput in the nanowire generation. The positioning of nanowires on the substrate and their contacting to the electrodes is a highly complicated process.

The field-assisted nanowire synthesis from an aqueous solution, by either dielectrophoretic particle assembly or directed electrochemical nanowire assembly, has the advantage of a high throughput such that many nanowires grow in parallel within a few minutes. Moreover, the growth of nanowires and their connection to the electrode happens in a single-step process at ambient conditions. Hence, the field-assisted growth of nanowires from aqueous solutions has the largest potential for an industrial-scale application. However, the nanowires grown with this technique often show branches and kinks, which have negative effects on their applications, e.g. lower sensitivity of sensors, reduced maximum integration density, or being less suitable as a waveguide [35]. Consequently, obtaining a precise control over the morphology of the growing nanowires is the major remaining challenge.

The morphology of solution-grown micro- and nanowires was observed to strongly depend on the AC voltage [22], the AC frequency [23, 25, 26], the ion [23] and cluster concentration [22, 23], the cluster size [22], and the viscosity of the solution [23]. To systematically optimize the parameter set to grow thin, straight, and unbranched *metal* nanowires from solution, a theoretical modeling framework is badly needed. However, so far, only few attempts have been made to model the multiphysical processes involved in the solution-based nanowire growth.

1.2 STATE OF THE ART

To simulate the dielectrophoretic cluster assembly Bhatt and Velev [23] implemented a cellular automaton based on a Finite Element Method (FEM) scheme. Each nanowire is resembled by a connected group of cells, to which an infinite conductivity is attributed. A voltage is applied to the two electrodes and by means of an FEM scheme the electric field in the remaining cells is calculated. All cells with an electric field above 80 % of the maximum value are added to the nanowire. The steps of field calculation and geometry updates are repeated until the nanowire connects the two electrodes. The simulation produces nanowire morphologies that show a high resemblance to the experimentally grown nanowires.

Xiong et al. [36] calculated the trajectories of metallic nanoparticles under the influence of a dielectrophoretic force. The analysis illustrated that surrounding nanoparticles are attracted particularly to the nanowire tip, which leads to the assembly of nanowire networks. From the comparison of branched and unbranched wire models it is concluded that branching is an inherent phenomenon in this type of nanoparticle assembly.

Ranjan et al. [37] suggested that the assembly of a nanowire from metal cations in an aqueous solution can be modeled similar to the dielectrophoretic assembly of metallic nanoparticles, since the metal cations and the counter-ion cloud form a polarizable entity [38]. A finite element calculation based on this assumption revealed that the energy difference caused by the dielectrophoretic attraction is several orders of magnitude below the thermal activation. Thus the ordering effect of the dielectrophoretic force is only minor. The authors explain that due to a field enhancement within the double layer and due to an atomically rough nanowire surface the electric field may locally be much higher than estimated. They argue that if the electric field is increased by several orders of magnitude, the dielectrophoretic assembly becomes plausible.

The group of Flanders claims in several works [2, 39, 40] that “dendritic solidification is an important mechanism in the DENA process”. In the modeling they consider the consumption of metal-cations due to the metal deposition. Based on the assumptions that first the metal cations are provided purely by diffusive transport and that second at the beginning of each AC period a uniform ion concentration is restored, the time average of the nanowire growth velocity is calculated. A connection between the nanowire-growth velocity and the nanowire-tip radius is drawn by employing results from solidification theory. The presented model, however, is flawed since first the ion concentration in a diluted aqueous solution is orders of magnitude lower than in a melt and thus solidification theory is not applicable. Second, with reference to Debye-Hückel theory, the authors argue that the influence of the electric field on the ion transport can be neglected. Considering that the application of Debye-Hückel theory requires a small, time-independent voltage, the reasoning does not hold for the large-amplitude and high-frequency voltage case that was studied in the experiments. Yet, by the unsubstantiated claim that the initial concentration profile is restored after each AC period, the AC frequency of the afore neglected electric field is found to have a large influence on the theoretically predicted nanowire growth velocity. For the above mentioned reasons, the hypothesized model of dendritic solidification, being an important mechanism in the DENA, is highly questionable.

1.3 OBJECTIVE

The objective of this work is to develop a theoretical modeling that describes the growth of nanowires from aqueous solutions. As discussed previously, there are two different methods to grow nanowires from an aqueous solution: the dielectrophoretic assembly of cluster or complexes and the directed electrochemical nanowire assembly. For each of these methods, a model describing the transport of metal species through the solution and the deposition at the nanowire surface is needed. Moreover, the electric potential has to be considered, since the electric field is one of the major driving forces for the transport. To verify the overall model, simulation results are compared to experimental measurements.

Based on the modeling and simulation results, it is aimed to provide well-founded suggestions on how to optimize the nanowire growth process to grow nanowires with smaller diameters and an improved morphology. This includes a quantitative proposal for the most important process parameters, AC frequency, AC voltage, and concentrations of the wire-forming species. Furthermore, the potential for optimization of the two assessed nanowire growth mechanisms, dielectrophoretic and directed electrochemical nanowire assembly, is to be compared.

As expounded in the motivation section, a multitude of applications rely on nanowires made from various metals. Up to now, the list of metals, for which a nanowire growth from an aqueous solution has been demonstrated, includes Ag, Au, Co, Cu, In, Ni, Pb, Pd, Pt, and Zn [2, 16, 41]. Interestingly, the most suitable process parameters as determined by experiments are broadly scattered. Accordingly, a secondary goal of this dissertation is to determine, whether and under which circumstances further metals are suitable to grow metallic nanowires from solution. And if so, which of the two investigated growth mechanisms is more suitable.

1.4 ELECTROCHEMICAL FOUNDATIONS

1.4.1 The basics of the electrochemical double layer

It is known that at the interface of an uncharged electrode and an electrolyte a compact double layer (aka Helmholtz double layer) forms, which consists of two thin layers. The reason for the formation of such double layers is that the ions in the electrolyte have different adsorption enthalpies and thus one ion type is preferably adsorbed at the electrode. The electrolyte layer, which contains these adsorbed ions, is the inner Helmholtz layer. Due to the preference of one ion type, the inner layer has a non-vanishing total charge. An equivalent surplus of counter-ions is accumulated in the directly neighboring outer Helmholtz layer due to Coulomb attraction between cations and anions. The thickness of both layers is typically in the order of 0.2 nm [42]. The separation of charges in the double layer induces an electric field and hence also a potential difference across the double layer. This potential difference is known as ζ-potential and is a quantitative measure for the affinity of the electrolyte system to the electrode surface. In aqueous solutions, typical values for the ζ-potential are in the range of 10 mV to 100 mV.

A second type of double layer, a diffuse or Gouy–Chapman double layer, can be created when the electrode is charged, i.e. an external voltage is applied to an electrode pair. Particularly, if the amount of charges on the electrode is large, the previously discussed compact double layer acts as a thin electro-neutral spacer. In the adjacent diffuse layer a cloud of ions is accumulated, which has the opposite charge to that of the electrode. Diffusion of and Coulomb repulsion among these ions cause the diffuse double layer to be much wider than the compact double layer.

In 1923 Debye and Hückel [43] developed a quantitative model to describe the diffuse double layer. They considered a linearized version of the Poisson–Boltzmann equation to calculate the ion concentrations in the double layer. Based on these calculations, it was possible to derive an expression for the double layer thickness, which is nowadays known as Debye length λ_D. The Debye length depends on the permittivity of the electrolyte, the temperature, the ion concentration and their charge number.

When an AC voltage is applied to the electrodes, the polarity of the diffuse layer is changed periodically. The corresponding relocation of ions is described by the Poisson–Nernst–Planck equation [44]. In later works, Bazant et al. [45, 46] extended this model towards large ion concentrations by employing a modified Poisson–Nernst–Planck equation. Under certain circumstances, the dynamic excitation of ionic motion gives rise to a new electrochemical-layer structure. Suh and Kang [47, 48] reported that for a sufficiently large AC frequency the dynamic repolarization spawns several additional diffuse layers. These diffuse layers differed in the predominant ion type and a so-called middle layer was found to oscillate at twice the excitation frequency.

1.4.2 AC electro-osmotic fluid flow on the micro- and nanoscale

As discussed in the previous section, the application of an AC voltage to an electrode pair, which has been dipped in an electrolyte, causes the formation of a dynamic multi-layer structure. As some of these layers have a net induced charge, the electric field in the vicinity of the electrodes induces a Coulomb force in these layers. If the electric field has a non-vanishing component tangential to the multi-layers, a shear force evolves. In a liquid electrolyte the tangential forces cause a fluid motion, which is the AC electro-osmosis (ACEO). More precisely, Bazant [49] defined: "AC electro-osmosis is a nonlinear electrokinetic phenomenon of induced-charge electro-osmotic flow around electrodes applying an alternating voltage".

Since the discovery of the ACEO by Ramos et al. [50], many experimental [51, 52] and theoretical [53–57] studies have been conducted to deepen the understanding of this effect. ACEO is applied in fluid pumping and mixing [55, 58] and to trap molecules [59] or entire cells [60]. The slip velocity approximation is the central simplification, used in most theoretical investigations of AC electro-osmotic fluid flow [56, 57, 61]. The underlying assumptions for this approximation are: a thin double layer with only a small polarization and a chemically inert, binary, symmetric electrolyte. Then, the forces, which drive the AC electro-osmotic fluid flow, are localized very close to the electrode surface. This allows the calculation of differences in fluid velocity difference across the thin double layer, which is used as a boundary condition for the Stokes equation. Compared to calculating the accelerating forces and solving the full Navier-Stokes equation, the slip velocity approximation offers huge savings in computation time and effort.

1.5 MODELING APPROACHES

To model the growth of nanowires, it is necessary to simulate, among others, the transport of wire-forming species in the solution. There are three classes of models available for this task: atomistic models, stochastic models, and continuum models.

In atomistic models, the location and state of each atom or molecule in the considered domain is traced over time. In the context of this work, molecular dynamics (MD) is the most reasonable choice to capture the motion of ions and metal clusters, their interactions with the solvent (water), and their assembly to nanowires. To reduce the computational effort, in MD methods, the inter- and intramolecular interactions are modeled with semi-empirical pseudo potentials and force-fields. Starting from an initial molecular configuration, the total force on each molecule is evaluated and the resulting trajectories of the molecules are calculated.

The advantage of atomistic models is a highly detailed description of the transport processes and in particular the interaction between different molecules in the solution. This comes at the cost of huge computational effort, which severely limits the number of atoms and the simulation time-frame. The actual limit for a feasible simulation depends on the molecule interaction potentials, but for the long-range coulomb interactions a typical simulation deals with much less than a million atoms and a time interval in the order of a few fs [62–64]. Hence, using MD one can neither simulate the entire system nor a practically meaningful simulation-time. Nevertheless, in a multi-scale model MD can be used to find effective material descriptions, which are then fed into the parametrization of a continuum model.

The most prominent of the stochastic models is the Monte Carlo (MC) simulation. A MC simulation of the nanowire growth from solution could focus on tracing either metal clusters or metal-containing ions in the solution, while the solvent is not considered in detail. The location of the metal clusters or ions is described by discrete positions (e.g. on a lattice) and movement is given as the transition between two neighboring, discrete positions. Since in such a model the atomistic interactions and the molecule locations cannot be described exactly, a probability is assigned to all possible transitions and to the unchanged state. The influence of external forces changes these probabilities such that energetically favorable transitions become more likely and others less likely. The transport of the wire-forming species is then given by the sequence of transitions over time. Due to the randomness within the MC simulation, the results of many runs have to be compared and statistically evaluated.

In comparison to the MD, MC provides only an effective description of the local, molecular interaction, but is computationally much faster, since dramatically fewer interactions on the molecular level need to be considered. Consequently, it is possible to model larger simulation volumes. By employing a discrete lattice with a grid spacing significantly larger than the typical molecule displacement for a single MD step, comparatively larger time steps can be used in the MC approach. However, the grid spacing cannot be chosen arbitrarily large, because otherwise an artificial upper bound for the concentration is introduced. Overall, the increase in simulation volume and time interval still is insufficient to capture the growth of nanowires.

In a continuum model, the atomic resolution of matter is disregarded and instead a homogeneous substitute, the continuum, is considered. For the example of particle transport through a solution, this means that not the position and motion of individual particles, but the ensemble-averaged concentration (particle number per volume) and flux (particle current density) of many similar particles are studied. Since in an average description one cannot deduce a unique state of all atoms and molecules, all interactions between them are expressed as a statistical average, usually with the help of partial differential equations (PDEs). In the present example, these PDEs express the flux in terms of the concentration profile and the forces acting on the particles. The set of all PDEs describes a deterministic model for the time evolution of the system.

The continuum model does not provide details about the micro-state of the solution, but in return this method offers the best computational performance. This includes the possibility to exploit the geometric symmetry of the setup in order to reduce the computational cost (details about this are discussed in section 2.2). The finite element method (FEM) is a highly flexible and efficient tool to numerically solve the PDEs obtained from a continuum model. Thus, it is possible to study many aspects of the growth of nanowires at reasonable computation costs.

As reasoned above, in this work, the simulation of the nanowire growth from solution is investigated by means of continuum models, which are solved with a FEM scheme. In chapter 2 of the thesis, the models for dielectrophoretic complex or metal cluster assembly and for the directed electrochemical nanowire assembly are developed and the results are discussed. The numeric details of how the involved PDEs have been solved are presented in chapter 3.

2 MODELING

2.1 AQUEOUS SOLUTIONS USED FOR NANOWIRE GROWTH

The two different nanowire growth mechanisms considered in this work, DEP and DENA (see section 1.1), require two different types of aqueous precursor solutions. The solution to grow DEP wires is obtained by dissolving K_2PtCl_4 in deionized water to a concentration in the range from 10 µM to 1 mM. During an aging phase, the $[PtCl_4]^{2-}$ ions in the solution are hydrolyzed. More experimental details about the preparation and handling of these types of solution can be found e.g. in Ref [21] and its supporting information.

For the hydrolysis of $[PtCl_4]^{2-}$ two main routes are known. For low pH solutions, Elding [65, 66] described a stepwise substitution of chloride ions by water molecules. The resulting chloro-aqua-platinate (II) complexes have the form $[PtCl_x(H_2O)_{4-x}]^{2-x}$, where $0 \leq x \leq 4$. This ligand exchange is accompanied by a change of the complex's overall charge. The planar structure of the $[PtCl_x(H_2O)_{4-x}]^{2-x}$ complexes gives rise to a conformation isomerism, i.e. $[PtCl_2(H_2O)_2]$ exists in a cis as well as a trans form. The formation of cis$-[PtCl_2(H_2O)_2]$ is particularly interesting, as it is electrically neutral, but has a remanent dipole. Therefore, under the influence of an applied inhomogeneous electric field, a dielectrophoretic force acts on the complexes [24], which attracts the complexes to the wire tip. This process is considered to be an integral step in the nanowire growth mechanism and therefore, for this scheme the name dielectrophoretic nanowire growth is attributed [22, 23].

At high pH, a hydrolysis by exchanging the chloride ions with hydroxy ions is discussed by Wu et al. [67]. This type of hydrolysis does not change the overall complex charge, as one monovalent anion ligand is replaced by another. The produced complexes are of the type $[PtCl_x(OH)_{4-x}]^{2-}$ with $0 \leq x \leq 4$.

The pH of the solution determines, which type of hydrolysis reaction is dominant under the experimental conditions. For an aged K_2PtCl_4 solution with a 10 µM concentration a pH of 8.6 was measured [21]. This intermediate pH is significantly lower than a pH of 14

Table 2.1: Reaction rate constants of the ligand exchange according to Elding [65, 66]

x	1	2c	2t	3c	3c	4
k_x (1/s)	2.8×10^{-7}	3×10^{-7}	10^{-4}	6×10^{-5}	2.8×10^{-8}	3.6×10^{-5}
k'_x (1/sM)	2.66×10^{-2}	2×10^{-3}	0.46	7.5×10^{-2}	4.6×10^{-5}	2.8×10^{-3}

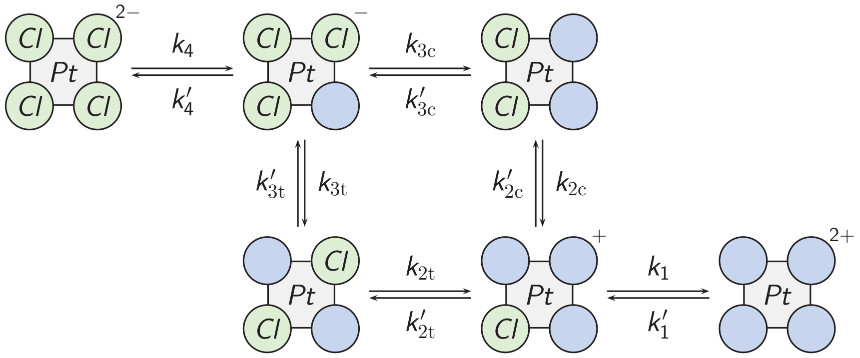

Figure 2.1: $[PtCl_x(H_2O)_{4-x}]^{2-x}$ hydrolysis scheme according to Elding [65, 66]. All shown complexes have a planar structure and therefore a cis and a trans conformer exist of $PtCl_2(H_2O)_2$. The reaction constants are given in Table 2.1.

as adjusted by Wu et al., but also much higher than the pH for the acidic conditions used by Elding. To transfer the results to this intermediate pH level, the hydrolysis mechanism is considered in detail.

For bimolecular ligand exchange reactions, collision theory predicts a reaction rate proportional to the concentration of the replacing ligand. For the $[PtCl_x(H_2O)_{4-x}]^{2-x}$-route, the replacing ligand is water, which is present in large excess. Also the concentration of water is quasi unaffected by the change of pH value. However, for a hydrolysis according to $[PtCl_x(OH)_{4-x}]^{2-}$-route, an exchange of hydroxy ions is needed, whose concentration is directly linked to the pH. Thus, for the intermediate pH as observed in the experiments, the reaction rate for the hydroxy-hydrolysis should be around 5 orders of magnitude smaller than reported by Wu and coworkers. Therefore, in the following, only the dissociation model developed by Elding [65, 66] is used for the simulation of the hydrolysis of K_2PtCl_4, cf. Figure 2.1. The corresponding reaction equations describe the hydrolysis.

$$[\mathrm{PtCl_4}]^{2-} + \mathrm{H_2O} \rightleftharpoons [\mathrm{PtCl_3(H_2O)}]^{-} + \mathrm{Cl}^{-} \tag{2.1}$$

$$[\mathrm{PtCl_3(H_2O)}]^{-} + \mathrm{H_2O} \rightleftharpoons \mathrm{cis}-[\mathrm{PtCl_2(H_2O)_2}] + \mathrm{Cl}^{-} \tag{2.2}$$

$$[\mathrm{PtCl_3(H_2O)}]^{-} + \mathrm{H_2O} \rightleftharpoons \mathrm{trans}-[\mathrm{PtCl_2(H_2O)_2}] + \mathrm{Cl}^{-} \tag{2.3}$$

$$\mathrm{cis}-[\mathrm{PtCl_2(H_2O)_2}] + \mathrm{H_2O} \rightleftharpoons [\mathrm{PtCl(H_2O)_3}]^{+} + \mathrm{Cl}^{-} \tag{2.4}$$

$$\mathrm{trans}-[\mathrm{PtCl_2(H_2O)_2}] + \mathrm{H_2O} \rightleftharpoons [\mathrm{PtCl(H_2O)_3}]^{+} + \mathrm{Cl}^{-} \tag{2.5}$$

$$[\mathrm{PtCl(H_2O)_3}]^{+} + \mathrm{H_2O} \rightleftharpoons [\mathrm{Pt(H_2O)_4}]^{2+} + \mathrm{Cl}^{-} \tag{2.6}$$

To model the hydrolysis reactions, the concentration of $[PtCl_x(H_2O)_{4-x}]^{2-x}$ is labeled with c_x, where the indices $2\mathrm{c}$ and $2\mathrm{t}$ distinguish the cis and trans species, respectively.

Mathematically, the stepwise ligand exchange reactions can be described as a system of first order differential equations and one algebraic equation to balance the chloride concentration, c_{Cl}.

$$c_{\mathrm{Cl}} = c_3 + 2\, c_{2\mathrm{c}} + 2\, c_{2\mathrm{t}} + 3\, c_1 + 4\, c_0, \tag{2.7a}$$

$$\frac{\mathrm{d}}{\mathrm{d}t} c_4 = k_4'\, c_3\, c_{\mathrm{Cl}} - k_4\, c_4, \tag{2.7b}$$

$$\frac{\mathrm{d}}{\mathrm{d}t} c_3 = k_{3c}'\, c_{2c}\, c_{\mathrm{Cl}} - k_{3c}\, c_3 + k_{3t}'\, c_{2t}\, c_{\mathrm{Cl}} - k_{3t}\, c_3 - k_4'\, c_3\, c_{\mathrm{Cl}} + k_4\, c_4, \tag{2.7c}$$

$$\frac{\mathrm{d}}{\mathrm{d}t} c_{2\mathrm{c}} = k_{2c}'\, c_1\, c_{\mathrm{Cl}} - k_{2c}\, c_{2c} - k_{3c}'\, c_{2c}\, c_{\mathrm{Cl}} + k_{3c}\, c_3, \tag{2.7d}$$

$$\frac{\mathrm{d}}{\mathrm{d}t} c_{2\mathrm{t}} = k_{2t}'\, c_1\, c_{\mathrm{Cl}} - k_{2t}\, c_{2t} - k_{3t}'\, c_{2t}\, c_{\mathrm{Cl}} + k_{3t}\, c_3, \tag{2.7e}$$

$$\frac{\mathrm{d}}{\mathrm{d}t} c_1 = k_1'\, c_0\, c_{\mathrm{Cl}} - k_1\, c_1 - k_{2c}'\, c_1\, c_{\mathrm{Cl}} + k_{2c}\, c_{2c} - k_{2t}'\, c_1\, c_{\mathrm{Cl}} + k_{2t}\, c_{2t}, \tag{2.7f}$$

$$\frac{\mathrm{d}}{\mathrm{d}t} c_0 = k_1\, c_1 - k_1'\, c_0\, c_{\mathrm{Cl}}. \tag{2.7g}$$

The rate constants, k_x for the chloride elimination and k_x' for the reattachment reaction, are given in Table 2.1. As initial condition, a solution with only tetra-chloroplatinate ions ($x = 4$) was used. The equation system was solved numerically using *ode45* function of MATLAB® . Figure 2.2a shows the time evolution of the various chloroplatinate ions and Figure 2.2b compares the different initial concentrations c_0. It is found that particularly for low total ion concentrations there is a time interval in which the vast majority of complexes have been converted to cis$-[PtCl_2(H_2O)_2]$. These complexes are electrically neutral, which is of importance in the further modeling. After about 48 h the fraction of cis$-[PtCl_2(H_2O)_2]$ peaks at around 92 % for $c_0 = 10\,\mu$M, cf. Figure 2.2a. The production of cis$-[PtCl_2(H_2O)_2]$ is strongly preferred against the trans conformer, which is known as trans effect [68]. For a larger initial concentration, the solution does not go through a state with predominantly neutral complexes. Therefore, in the experiments the remaining platinate ions were removed using ion exchangers.

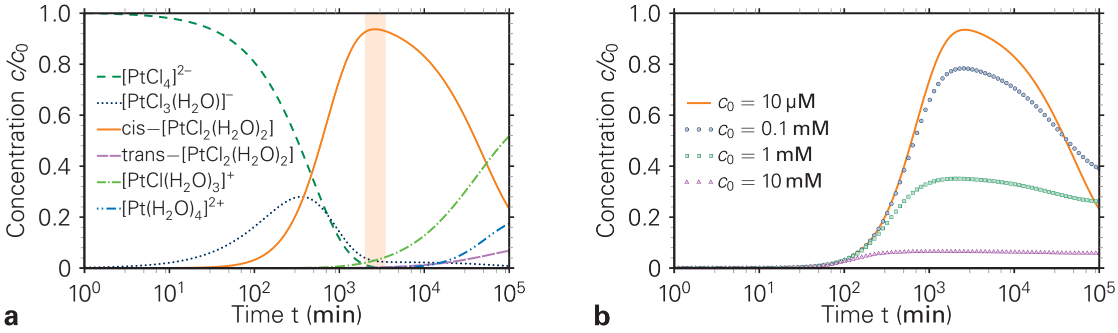

Figure 2.2: (a) Starting from an initial $[PtCl_4]^{2-}$-concentration of $c_0 = 10\,\mu$M, the time-dependent concentration of all considered species during the hydrolysis is simulated. The neutral cis$-[PtCl_2(H_2O)_2]$ species exhibits a maximum concentration of more than 90 % from 2000 min to 3500 min. (b) The size and location of that maximum cis$-[PtCl_2(H_2O)_2]$ concentration strongly depends on the initial K_2PtCl_4 concentrations.

Solutions produced in the described manner were characterized using TEM [21] and Pt clusters of around 23 nm diameter with a narrow diameter distribution were found, cf.

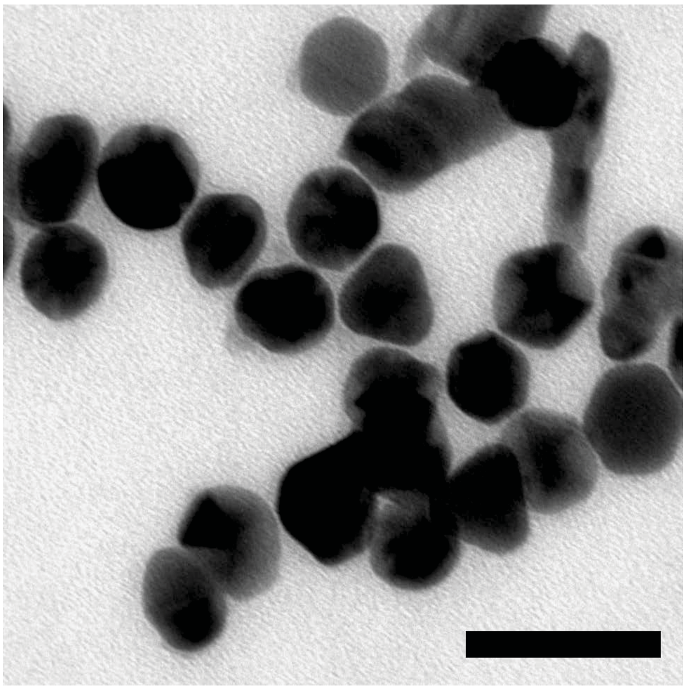

Figure 2.3: This TEM image shows the platinum clusters found in a 10 µM K_2PtCl_4 solution, which was aged for 27 h. The scale bar is 50 nm and the measured cluster diameter is about 23 nm. Reprinted with permission from the supporting information of [21]. Copyright 2012 American Chemical Society.

Figure 2.3. It is presumed that a photo-induced auto-catalysis leads to a cluster formation similarly as described by Shironita et al. [69]. Despite the finding of metallic clusters in the solution, wires potentially grown from their assembly also belong to the category of dielectrophoretically grown wires, as metallic clusters are highly polarizable and thus are also subject to the dielectrophoretic force.

To grow nanowires according to the DENA mechanism, a different solution is required. It is prepared by diluting a H_2PtCl_6 stock-solution to a concentration of e.g. 24 mM [26] or 200 µM [70]. The hexa-chloro-platinate (IV) complexes undergo a hydrolysis similar to the tetra-chloro-platinate (II) complexes above [71]. Employing only freshly prepared solutions ensures that platinum only occurs in the form of $[PtCl_6]^{2-}$, $[PtCl_5(H_2O)]^{-}$, and $[PtCl_5(OH)]^{2-}$. The fact that all of these ions are negatively charged is of special importance for the growth mechanism, which is addressed in section 2.7.3 in detail.

2.2 GEOMETRIC CONSIDERATION OF THE NANOWIRE GROWTH

To understand the mechanism of nanowire growth and the modeling based thereon, it is informative to analyze the solution region, from which the wire-forming species originate. The volume of solution that is depleted during the nanowire growth can be estimated by balancing the particles taking part in the nanowire growth. To determine the deposited metal volume, the wire cross-section needs to be characterized. AFM line scans suggest

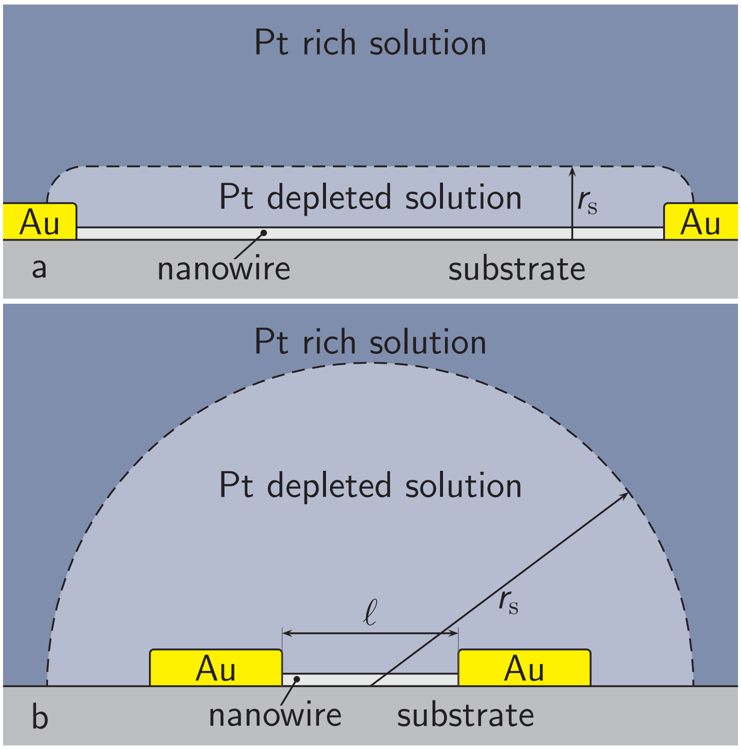

Figure 2.4: Region of origin for the wire forming species. Sketch (a) applies to long wires and highly concentrated growth solutions, sketch (b) is valid for shorter wires and highly diluted solutions.

that idealizing the nanowire cross-section by a semicircle is feasible [38]. The wire volume is then given by

$$V_\mathrm{w} = \frac{\pi}{8}\,\ell\, d_\mathrm{w}^2, \tag{2.8}$$

with the wire length ℓ and diameter d_w. The solution volume, which contains the equivalent amount of platinum in the form of equally distributed particles

$$V_\mathrm{s} = \frac{V_\mathrm{w}}{c_\mathrm{b}\, V_\mathrm{p}} \tag{2.9}$$

depends on the initial particle concentration of the solution c_b and the particle volume V_p. In the case of complexes the particle volume is expressed by the volume of one platinum atom in the metallic bulk, which is determined from the mass density ρ_Pt and the atomic mass m_Pt as $V_\mathrm{p} = m_\mathrm{Pt}/\rho_\mathrm{Pt} = 1.51 \times 10^{-29}\,\mathrm{m}^3$.

The characteristic transport length is the typical distance that a particle travels before it is deposited at the nanowire tip. From the knowledge of the typical transport length, relevant transport mechanisms and time scales for the nanowire growth can be deduced. The characteristic transport length depends on the size and shape of the depletion volume. If $V_\mathrm{s} \ll \ell^3$ the particles originate from the vicinity of the nanowire. Then, the depletion volume has the shape of a tight semi-cylinder around the wire as depicted in Figure 2.4a. However, if $V_\mathrm{s} \gg \ell^3$ the particles in the vicinity are insufficient to form the nanowire and particles from remote locations contribute to the wire assembly as well. The resulting shape of the depletion volume is approximately hemispherical, cf. Figure 2.4b.

From the semi-cylinder volume, $V_s = \pi\, r_\mathrm{s}^2\, \ell/2$, the typical transport length r_s for case a) results as

$$r_\mathrm{s} = \frac{d_\mathrm{w}}{2\,\sqrt{c_\mathrm{b}\,V_\mathrm{p}}}. \tag{2.10}$$

In case b), the volume of the depletion hemisphere, $V_s = 2\,\pi\, r_\mathrm{s}^3/3$, leads to

$$r_\mathrm{s} = \sqrt[3]{\frac{3\,\ell\, d_\mathrm{w}^2}{16\, c_\mathrm{b}\, V_\mathrm{p}}}. \tag{2.11}$$

The dielectrophoretically grown nanowires from an assembly of Pt-complexes ($\ell = 2\,\mu\mathrm{m}$, $c_\mathrm{b} = 10\,\mu\mathrm{M}$, $d_\mathrm{w} = 100\,\mathrm{nm}$ [21]) correspond to case b) of a long-range transport and yield a characteristic transport length of $r_\mathrm{s} = 21.8\,\mu\mathrm{m}$. A transport length in this order of magnitude implies that the transport of particles is an integral part of the overall growth mechanism. Consequently, in section 2.3 and the following, the transport of wire forming particles is considered in more detail.

A second geometric consideration focuses on the shape of the growing nanowires. When conducting the experiments, usually numerous nanowires grow in parallel; they have kinks, branches, and some even stop growing in an early stage, which results in stubs. Figure 2.5a shows a schematic three-dimensional model of typical DEP grown nanowires. The geometry of such nanowires is too complex to perform simulations on them directly. Therefore, two more simplified geometries have been developed to replace them. On a flat substrate, a nanowire with a homogeneous thickness and without any kinks or branches is a semi-cylinder with a smooth, spherical wedge as a cap. Regarding the particle transport the substrate is impenetrable, i.e. the normal component of the flux is identical zero. If the substrate is replaced by the mirror image of the nanowire and the surrounding solution, the symmetry ensures a vanishing normal flux across the mirror plane, too. Thus, by this manipulation the concentration profile and the particle flux in the original geometry are unaffected.

A similar argument holds for the electrostatic problem. The dielectric constant of water ($\varepsilon_\mathrm{r} = 80$) is one order of magnitude larger than that of common substrate materials like silicon ($\varepsilon_\mathrm{r} = 12.1$) with an oxide layer ($4.41 \leq \varepsilon_\mathrm{r} \leq 4.6$) or silicate glass ($\varepsilon_\mathrm{r} = 3.81$) [72]. At phase boundaries like at the substrate surface, the normal component of the dielectric flux and the tangential component of the electric field is continuous. Because of the large step in the dielectric constant at the interface, the normal component of the dielectric flux is very small compared to its tangential component. Therefore, by introducing the mirror symmetry, only a small error in the order of the negligible normal dielectric flux is introduced.

The advantage of introducing the mirror symmetry is that the nanowire, despite growing on a substrate, can be equivalently modeled as a free-standing, axially symmetric wire,

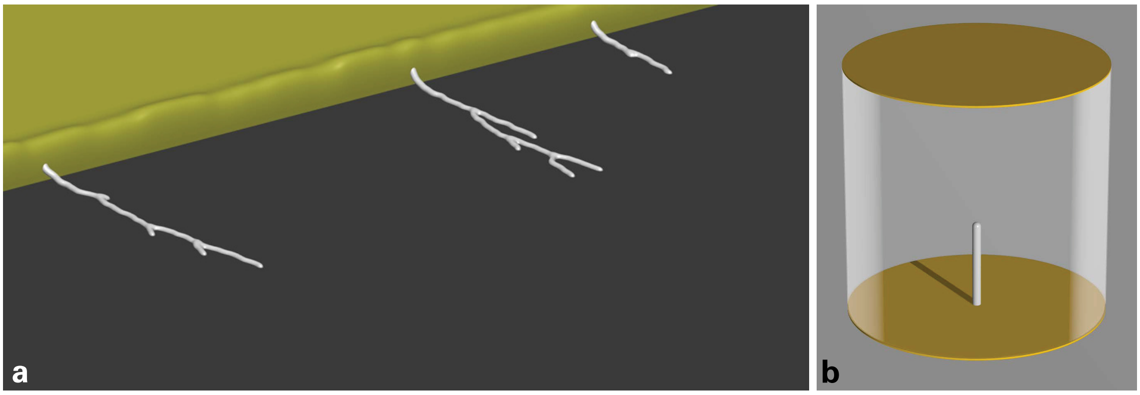

Figure 2.5: Panel (a) shows a schematic image of platinum nanowires grown from a lithographically manufactured gold electrode. The nanowires grow in groups, are kinked and branched, and bend towards the substrate at which the are attached. Panel (b) depicts an idealized, single, free-standing nanowire, which is used in the further simulations as a geometric simplification of the setup shown in panel (a).

cf. Figure 2.5b. This modified geometry, in contrast to the original one, can be modeled efficiently in a cylindrical coordinate system by the radius r and the axial coordinate z. When the partial differential equations are solved by means of FEM, the increased symmetry results in a dramatic reduction of degrees of freedom, which brings the computational effort to a manageable level.

The local physics of the particle transport mechanisms at the nanowire tip is determined by the curvature of the electrode. An even simpler geometric model, which preserves these curvature effects, is to replace the nanowire by a sphere of the same diameter. In spherical coordinates, this model has only a radial dimension. Due to the simplicity of this one-dimensional model, analytical solutions for various equations can be derived. From the experimental fact that most nanowires have a homogeneous diameter over their length (cf. experimental images in Figure 2.9), it can be concluded that growth happens mainly at the tip and not so much on the circumference. Fro this reason, the one-dimensional relations should apply at least qualitatively. The geometric parametrization of both spherical and cylindrical models is given in Figure 2.6.

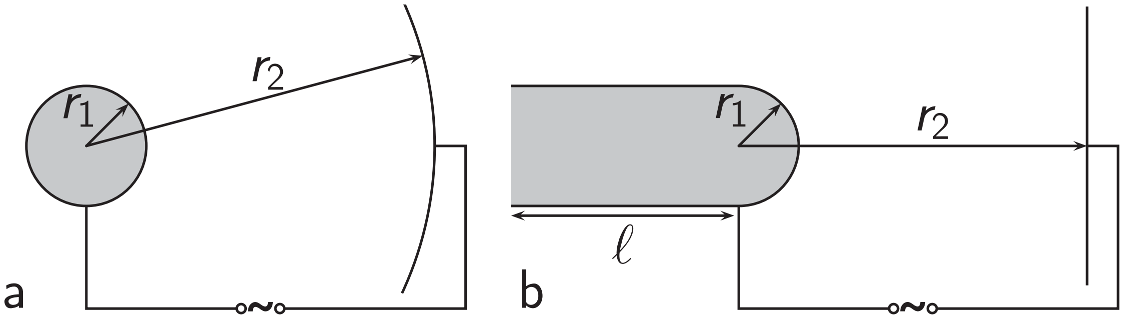

Figure 2.6: Spherical (a) and cylindrical (b) nanowire approximation with parametrization, which are used as electrode geometries in the modeling.

2.3 DIELECTROPHORETIC NANOWIRE GROWTH MODEL

2.3.1 Particle transport under the influence of dielectrophoresis

To grow nanowires by the dielectrophoretic mechanism, a solution with neutral complex molecules or metal clusters is employed, cf. section 2.1. Under the influence of an external electric field, the clusters and complexes are polarized. If the applied electric field is non-uniform, a dielectrophoretic force acts on the dipoles [24]. Since the electric field around nanoelectrodes is particularly large and inhomogeneous, the particles are strongly attracted to the tip of the growing nanowire. In the case of complexes arriving at the nanowire tip, they are first adsorbed and afterwards electrochemically reduced to metallic platinum, which is attached to the wire surface.

$$\mathrm{PtCl_2(H_2O)_2 \rightarrow Pt\,(s) + Cl_2(g) + 2\,H_2O} \tag{2.12}$$

The oxidized chlorine either leaves the system in the form of small gas bubbles or is solved in water and reacts ultimately according to

$$\mathrm{Cl_2(g) + H_2O \rightleftarrows HCl + HClO.} \tag{2.13}$$

The arriving metal clusters are accumulated at the nanowire tip as well. Due to the strong DEP forces the hydration and/or chloride shell of the metal clusters is penetrated until the metal surfaces are in direct contact. Then, in a sintering-like process, the clusters are permanently attached to the wire. Due to the high curvature and the large electric activation this process can already happen at ambient conditions [73].

In a continuum model, the distribution of particles is described by their concentration c and the their transport by the particle flux $\mathbf{j}$, cf. section 1.5. These quantities are linked by the continuity equation

$$\frac{\partial}{\partial t} c = -\nabla \cdot \mathbf{j}, \tag{2.14a}$$

Under the influence of an external potential ψ a migration contributes to the particle flux. Additionally, the particles are subject to diffusion, so that the overall particle flux is thus given by

$$\mathbf{j} = -D\,\nabla c - M\,c\,\nabla\psi, \tag{2.14b}$$

where M is the mobility and D is the diffusion coefficient of the particles. The Einstein–Smoluchowski–equation, $M = D/(k_\mathrm{B} T)$, relates the mobility to the diffusion coefficient by the Boltzmann constant k_B and the absolute temperature T. According to Stokes' law, $M = 1/(6\,\pi\,\eta\,r_\mathrm{p})$, the mobility of small spheres, e.g. complexes or metal clusters, depends strongly on their radius r_p and the viscosity of the medium η. Hence, for the diffusion coefficient of small particles holds

$$D = \frac{k_\mathrm{B} T}{6\,\pi\,\eta\,r_\mathrm{p}}. \tag{2.15}$$

To obtain the boundary conditions of Equation 2.14, it is assumed that particles, which arrive at the nanowire surface, react instantly. Consequently, at this boundary the concentration is $c = 0$. Moreover, during the whole process of nanowire growth only a negligible fraction of the initial particles is consumed, so sufficiently far from the electrode ($r \gg r_\mathrm{s}$) the initial concentration is preserved, $c = c_\mathrm{b}$. At the cut-off boundaries of the simulation cell (only relevant for axially symmetric wire geometry) the normal component of the particle flux vanishes, $\mathbf{j} \cdot \mathbf{n} = 0$.

According to Ref. [24], for a given electric potential φ, the external potential for the dielectrophoretic attraction is

$$\psi_\mathrm{DEP} = -\alpha\,(\nabla\varphi)^2/2, \tag{2.16}$$

where α is the polarizability of the particles. From the Clausius–Mossotti relation, the polarizability of metal clusters is derived [24]

$$\alpha = 4\,\pi\,\varepsilon\,\mathfrak{Re}[K(f)]\,r_\mathrm{p}^3, \tag{2.17}$$

with $\varepsilon = \varepsilon_\mathrm{r}\,\varepsilon_0$ as the medium dielectric constant. The Clausius–Mossotti factor for metallic particles is $K = 1$ in the considered frequency range. The polarizability of molecules has two contributions: the induction of transient dipoles and the alignment of remanent intrinsic molecular dipoles μ [74],

$$\alpha = \alpha_0 + \mu^2/(3\,k_\mathrm{B}\,T). \tag{2.18}$$

In contrast to trans$-$PtCl$_2$, cis$-$PtCl$_2$ has a non-vanishing molecular dipole. However, the dipole moment of cis$-$[PtCl$_2$(H$_2$O)$_2$] has not been reported in the literature. Therefore, the dipole moment of the chemically similar complex cis$-$[PtCl$_2$(NH$_3$)$_2$] is used as an approximate estimate. From *ab initio* calculations it was determined to be $\mu \approx 10\,\mathrm{D}$ [75]. The electronic polarizability of a molecule α_0 typically is smaller than $1 \times 10^{-38}\,\mathrm{Cm^2/V}$ [76] and as such negligible compared to the orientation polarizability. Therefore, the overall polarizability of cis$-$PtCl$_2$ is approximated by $\alpha \approx \mu^2/3k_\mathrm{B}T \approx 1 \times 10^{-37}\,\mathrm{Cm^2/V}$.

Additionally to the clusters and complexes the solution contains K$^+$ and Cl$^-$ ions from the dissociation and hydrolysis of K$_2$PtCl$_4$ and possibly substitute ions from the optional application of the ion exchanger. Under the influence of the external electric potential the ions are redistributed, which creates a space charge density ρ. In the presence of a space charge density the electric potential is given by the Poisson equation

$$\nabla^2\varphi = -\frac{\rho}{\varepsilon}, \tag{2.19}$$

However, in the experimentally relevant limit of small ion concentrations and large frequencies, the charge density is negligible (a proof is given in section 2.5.3 on page 34) and Equation 2.19 simplifies to

$$\nabla^2\varphi = 0. \tag{2.20}$$

The electric potential is subject to the boundary conditions $\varphi = V_0\,\sin(2\,\pi\,f\,t)$ at the nanowire electrode and $\varphi = 0$ at the counter electrode. On the unattributed cut-off boundaries of the simulation cell, a vanishing normal derivative of the electric potential is required, $\nabla\varphi \cdot \mathbf{n} = 0$.

2.3.2 Calculation of the nanowire growth velocity

The aforementioned particle transport equations are solved for the entire solution volume. As the solid wire forms, the size and shape of the simulation domain changes, which is known as a moving boundary problem. In general, moving boundary problems are numerically more challenging than fixed boundary problems. Therefore, in the following it is shown that the approximation as a fixed boundary problem is justified.

The velocity of boundary movement is the nanowire growth velocity v_g, given through the balance of the total volume of all deposited particles with the increased wire volume

$$v_\mathrm{g} = V_\mathrm{p}\, \mathbf{j} \cdot \mathbf{n}. \tag{2.21}$$

The velocity of individual particles movement through the solution is expressed as $\mathbf{v}_\mathrm{p} = \mathbf{j}(r)/c(r)$, which leads to

$$v_\mathrm{g} = V_\mathrm{p}\, c\, \mathbf{v}_\mathrm{p} \cdot \mathbf{n}. \tag{2.22}$$

In highly diluted solutions, particularly close to the electrode, where the particles are consumed in the deposition reaction, the platinum volume fraction in the solution is $V_\mathrm{p}c \ll 1$. Thus, from Equation 2.22 follows that the normal particle velocity at the interface is several orders of magnitude larger than the nanowire growth velocity. Thus, the movement of the boundary due to nanowire growth has a negligible influence on the solution of the PDEs. Hence, in all following simulations a fixed boundary problem is considered.

In a first step, Equations 2.14 and 2.20 with their respective boundary conditions are considered for the spherical electrode geometry, cf. Figure 2.6a on page 15. The analytical solution of the electric potential for $r_2 \gg r_1$ is

$$\varphi(r, t) = \frac{V_0\, r_1}{r} \sin(2\, \pi\, f\, t). \tag{2.23}$$

From a time-dependent electric potential results also a time-dependent dielectric potential, cf. Equation 2.16. Since the dominant eigenfrequencies of Equation 2.14 are much smaller than the oscillation frequency of the applied AC voltage, it is justified to consider the time average of ψ in the calculations. The stationary limit of Equation 2.14b in spherical coordinates then reads

$$\begin{aligned} \frac{\partial}{\partial r}\left[r^2\, D \left(-\frac{\partial c}{\partial r} - c\, \frac{\partial \tilde{\psi}}{\partial r} \right) \right] &= 0, \\ \tilde{\psi}(r) &= -\frac{\alpha\, (V_0\, r_1)^2}{4\, k_\mathrm{B} T\, r^4}. \end{aligned} \tag{2.24}$$

After integrating Equation 2.24, the resulting linear, first order ordinary differential equation (ODE) can be solved by separation of variables. Its analytical solution with respect to the boundary conditions is then given by

$$c(r) = c_\mathrm{b} \frac{\int_{r_1}^{r} \mathrm{d}r' \exp[\tilde{\psi}(r') - \tilde{\psi}(r)]/r'^2}{\int_{r_1}^{r_2} \mathrm{d}r' \exp[\tilde{\psi}(r') - \tilde{\psi}(r_2)]/r'^2}. \tag{2.25}$$

Table 2.2: Simulation parameters for the dielectrophoretic nanowire assembly of complex molecules and platinum clusters

symb.	value	description
f	100 kHz	AC frequency
V_0	4 V	voltage amplitude
r_1	50 nm	electrode radius, cf. Figure 2.6
r_2	1.1 µm	counter electrode radius cf. Figure 2.6
ℓ	0.4 µm	nanowire length, cf. Figure 2.6b
T	293 K	absolute temperature
η	1.0 mPa s	dynamic viscosity of water [77]
V_{Pt}	$1.51 \times 10^{-29}\,\mathrm{m}^3$	volume of one platinum atom $V_{\mathrm{Pt}} = m_{\mathrm{Pt}}/\rho_{\mathrm{Pt}}$
c_{b}	10 µM	initial K_2PtCl_4 concentration
ε_{r}	80	relative dielectric constant
cis – $PtCl_2(H_2O)_2$ specific parameters		
r_{p}	≈ 0.5 nm	complex radius incl. hydration shell [78]
D	$4.3 \times 10^{-10}\,\mathrm{m}^2/\mathrm{s}$	diffusion coefficient, cf. Equation 2.15
α	$1 \times 10^{-37}\,\mathrm{Cm}^2/\mathrm{V}$	polarizability, cf. Equation 2.18
Pt cluster specific parameters		
r_{p}	11.5 nm	cluster diameter, cf. Figure 2.3
D	$1.9 \times 10^{-11}\,\mathrm{m}^2/\mathrm{s}$	diffusion coefficient, cf. Equation 2.15
α	$1.37 \times 10^{-32}\,\mathrm{Cm}^2/\mathrm{V}$	polarizability, cf. Equation 2.17

From Equation 2.14b the magnitude of the radial particle flux is obtained as

$$j_r(r) = \frac{D\, c_{\mathrm{b}} \exp\left[\tilde{\psi}(r_2)\right]/r^2}{\int_{r_1}^{r_2} \mathrm{d}r' \, \exp\left[\tilde{\psi}(r')\right]/r'^2}. \tag{2.26}$$

Due to the lack of quantitative evidence whether the aqueous solution as prepared contains platinum mainly in the form of neutral complexes or in the form of clusters, the two extreme cases of only complexes and only clusters are compared. If the clusters are grown from complexes in advance of the experiment, the total amount of platinum is unchanged, i.e. $c_{\mathrm{b}}\, V_{\mathrm{p}} = \mathit{const}$. Therefore, the growth velocity in both cases is given by

$$v_{\mathrm{g}}(r_{\mathrm{p}}) = \frac{D(r_{\mathrm{p}})\, c_{\mathrm{Pt}}\, V_{\mathrm{Pt}}}{r_1^2 \int_{r_1}^{r_2} \mathrm{d}r' \exp\left[\tilde{\psi}(r')\right]/r'^2}. \tag{2.27}$$

The used simulation parameters are summarized in Table 2.2. In the case of only complexes the growth velocity $v_{\mathrm{g}} = 0.83$ nm/s is computed, whereas the opposite case of only clusters with a radius of 11.5 nm yields $v_{\mathrm{g}} = 0.57$ nm/s. A simultaneous deposition of clusters and complexes should yield an intermediate growth velocity.

Owing to uncertainties in the particle size estimation and preparation, it is useful to analyze its influence on the nanowire growth velocity more generally. For a sufficiently large counter electrode radius of $r_2 \gtrsim r_{\mathrm{s}} = \mathcal{O}(20\,\mu\mathrm{m})$ the electric field near the second electrode becomes negligibly small. Then, there holds $\exp[\tilde{\psi}(r_2)] \approx 1$ and Equation 2.27 is rewritten to

$$\frac{k_1}{v_\mathrm{g}(r_\mathrm{p})} = \int_{r_1}^{r_2} \mathrm{d}r' \, r_\mathrm{p} \, \exp\left(k_2 \, r_\mathrm{p}^3/r'^4\right)/r'^2, \tag{2.28}$$

with the abbreviations $k_1 = k_\mathrm{B} T \, c_\mathrm{Pt} \, V_\mathrm{Pt}/(6 \, \pi \, \eta \, r_1^2)$ and $k_2 = -\pi \, \varepsilon \, (V_0 \, r_1)^2/(k_\mathrm{B} T)$. The derivative of Equation 2.28 with respect to r_p yields

$$\frac{\partial}{\partial r_\mathrm{p}} \frac{k_1}{v_\mathrm{g}(r_\mathrm{p})} = \int_{r_1}^{r_2} \mathrm{d}r' \left[\frac{1}{r'^2} + \frac{3 \, k_2 \, r_\mathrm{p}^3}{r'^6}\right] \exp\left(k_2 \, r_\mathrm{p}^3/r'^4\right), \tag{2.29}$$

which after partial integration becomes

$$\frac{\partial}{\partial r_\mathrm{p}} \frac{k_1}{v_\mathrm{g}(r_\mathrm{p})} = \frac{1}{4} \int_{r_1}^{r_2} \mathrm{d}r' \, \frac{1}{r'^2} \exp\left(k_2 \, r_\mathrm{p}^3/r'^4\right) - \frac{3}{4} \left[\frac{1}{r'} \exp\left(k_2 \, r_\mathrm{p}^3/r'^4\right)\right]_{r_1}^{r_2}. \tag{2.30}$$

The argument of the exponential in Equation 2.30 equals $\tilde{\psi}(r)$ and evaluates to $\tilde{\psi}(r_1) \ll -1$ at the inner electrode. Hence, the term $\exp[\tilde{\psi}(r_1)]$ can be neglected. By back-substituting with Equation 2.27 one obtains

$$\frac{\partial}{\partial r_\mathrm{p}} \frac{k_1}{v_\mathrm{g}(r_\mathrm{p})} = \frac{1}{4 r_\mathrm{p}} \frac{k_1}{v_\mathrm{g}(r_\mathrm{p})} - \frac{3}{4 \, r_2}, \tag{2.31}$$

which has the analytical solution

$$\frac{k_1}{v_\mathrm{g}(r_\mathrm{p})} = k_3 \, r_\mathrm{p}^{1/4} - \frac{r_\mathrm{p}}{r_2}. \tag{2.32}$$

For the simulation parameters given in Table 2.2, it can be verified that $k_1/v_\mathrm{g}(r_\mathrm{p}) \gg r_\mathrm{p}/r_2$ and finally, after neglecting r_p/r_2 the relation $v_\mathrm{g}(r_\mathrm{p}) \propto r_\mathrm{p}^{-1/4}$ is obtained. Consequently, a deviation of cluster size by a few nanometers has hardly an effect on the growth velocity.

For a more accurate estimation of the wire growth velocity, the cylindrical electrode geometry is considered, cf. Figure 2.6b on page 15. The numerical solution of Equation 2.14 and the resulting nanowire growth velocity according to Equation 2.21 in the stationary limit are shown in Figure 2.7. The tip growth velocity for this setup using Pt complexes is obtained as 0.64 nm/s, which is close to the estimation obtained from the simpler spherical model.

2.3.3 Comparison of measured and calculated nanowire growth velocities

Wire morphology Figure 2.7 shows that a model considering only diffusion and dielectrophoretic migration leads to a rather uniform distribution of the nanowire growth velocity along the wire circumference. Presumably, this causes the wire to grow significantly in width, which changes their morphology to a clubbed shape. In some experiments [79] such morphologies have been observed as shown in Figure 2.8. Remarkably, the

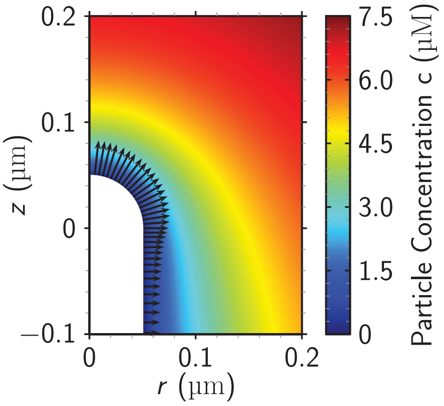

Figure 2.7: Particle concentration near the nanowire tip and wire growth velocity along the wire surface (arrows) with a maximum of 0.64 nm/s along the z-axis.

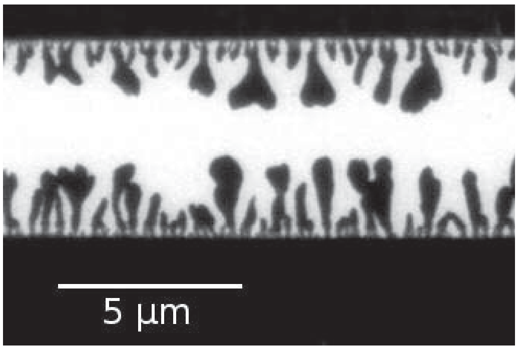

Figure 2.8: The TEM image shows the morphology of assembled nanostructures grown by dielectrophoresis from gold clusters. Reprinted with permission from the supporting information of [79]. Copyright 2007 American Chemical Society.

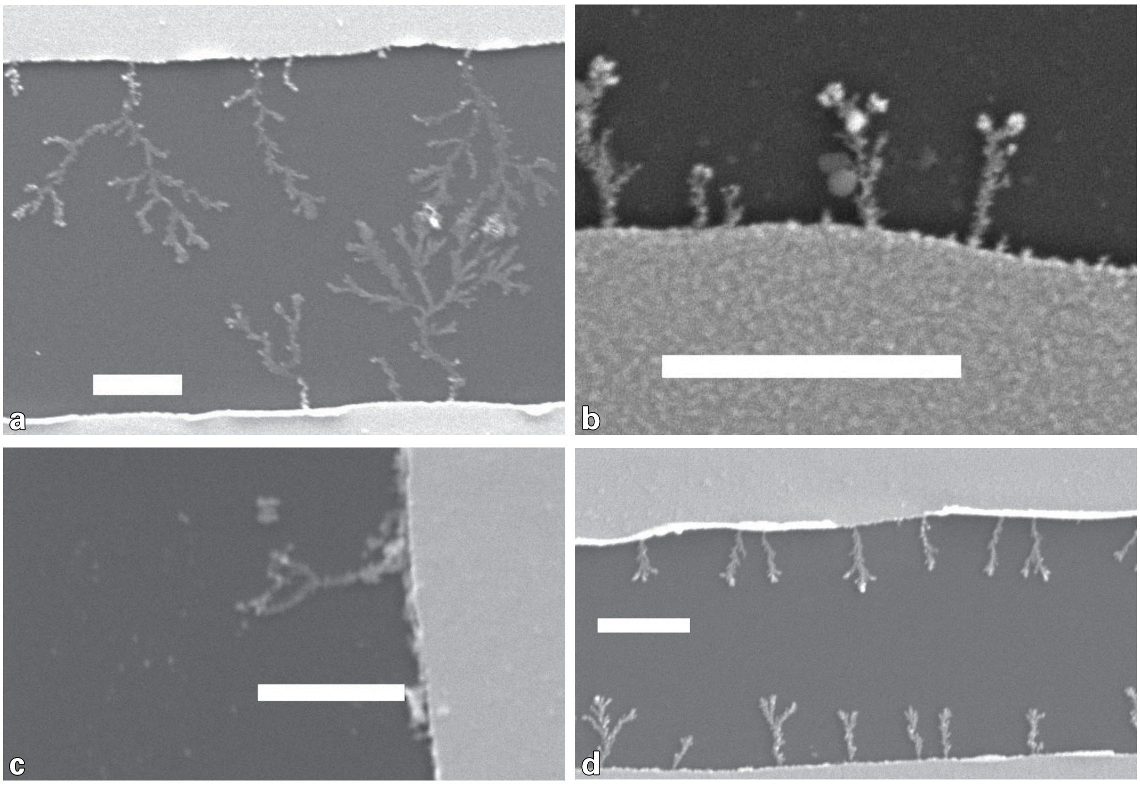

Figure 2.9: A variety of nanowire morphologies is grown from an aged K_2PtCl_2-solution at room temperature (a,b). The temperature influence is shown in panels (c) $T = 289\,K$ and (d) $T = 316\,K$. The scale bars are 1 µm. Growth parameters: $V_0 = 4\,V$, $f = 100\,kHz$, $c_b = 10\,\mu M$; Reprinted with permission from [21]. Copyright 2012 American Chemical Society.

nanostructures in Figure 2.8 are very densely packed, which hints at a large particle concentration in the assembly zone. Regarding the discussion of particle origin (Figure 2.4 on page 13) this means that the particles are transported over only comparatively short distances.

For comparison Figure 2.9 shows an overview of wire morphologies grown by A. Nerowski. In all panels significantly fewer nanowires than in Figure 2.8 have grown. Despite their variety of wire morphologies, in each picture, most of the nanowire segments have a homogeneous thickness. Consequently, the particle concentration in the assembly zone should have been much smaller in these experiments. Therefore, the particles that are necessary for the wire assembly should originate from much farther regions.

Experimental determination of the nanowire growth velocity To determine the experimental nanowire growth velocities for a comparison with theoretical predictions, one has to overcome several difficulties. Foremost, the shape and morphology of the grown wires show a broad variety, cf. Figure 2.9. For a substantial quantitative analysis, it is essential to distinguish between these morphologies as the growth velocities differ greatly due to the different underlying growth mechanisms. In the following, only nanowires with a homogeneous thickness and with few or no branches are considered.

The average growth velocity is given as the nanowire length divided by the growth time. The length of a kinked and possibly branched nanowire is defined as the longest path along the traverse of straight wire segments. The nanowire growth time is approximated by the total experimenting time, since the wire nucleation time is negligible in comparison [21].

Temperature dependence The temperature dependence of the nanowire growth velocity is shown in Figure 2.10. Two clearly distinct behaviors are revealed with a transition temperature at about 301 K. For the high-temperature branch the thermal activation is larger which facilitates the reaction. For a sufficiently fast reaction rate, the nanowire growth process is only limited by the amount of molecules transported to the wire surface. In agreement with Equation 2.27, the growth velocity is then proportional to the diffusion coefficient

$$v_{\mathrm{g}}(T) \propto D(T) = \frac{k_{\mathrm{B}} T}{6\,\pi\,\eta(T)\,r_{\mathrm{p}}}. \tag{2.33}$$

The temperature dependence of the viscosity of water can be described by the Vogel–Fulcher–Tammann equation [80]

$$\eta(T) = \eta_0 \exp\left(\frac{B}{T - C}\right), \tag{2.34}$$

an empirical law ($\eta_0 = 28.86\,\mu\mathrm{Pa\,s}$, $B = 513.4\,\mathrm{K}$, $C = 148.5\,\mathrm{K}$), which resembles the tabulated viscosities of water [77] with less than $0.25\,\%$ error. The high-temperature branch of the measured nanowire growth velocities is fitted to this model, Equation 2.33.

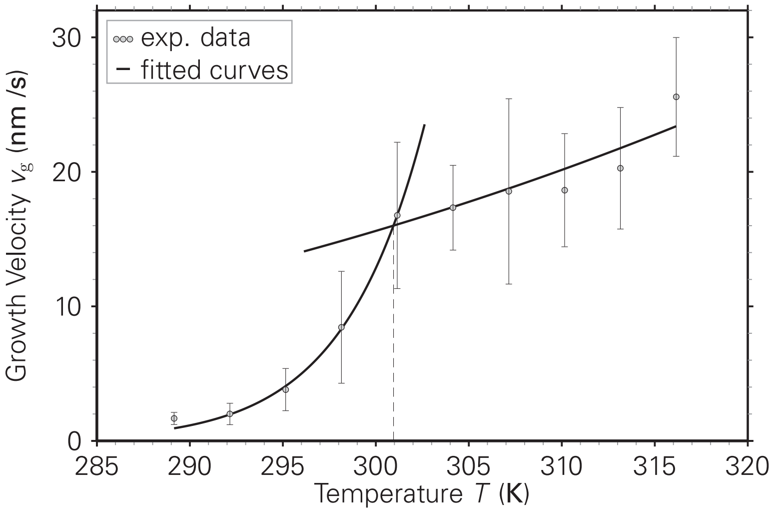

Figure 2.10: Measured nanowire growth velocity as a function of the temperature (K_2PtCl_4 concentration 10 µM). The lines are fits according to Equations 2.33 and 2.35. Reprinted with permission from [21]. Copyright 2012 American Chemical Society.

The low-temperature branch suggests that platinum deposition is limited by a small reaction rate. Under this prerequisite the overall growth velocity is determined by the reaction rate, whose temperature dependence is assumed to obey an Arrhenius function

$$v_\mathrm{g}(T) \propto \exp\left(\frac{-E_\mathrm{A}}{k_\mathrm{B} T}\right). \tag{2.35}$$

The activation energy E_A involved in the fit is determined as $E_\mathrm{A} = 1.80\,\mathrm{eV}$.

Concentration dependence The dependence of the nanowire growth velocity on the K_2PtCl_4 concentration is depicted in Figure 2.11. For the two temperatures considered, 298 K and 316 K, the curves are unexpectedly different. The high-temperature curve is linear in the whole measurable range, whereas the low-temperature curve saturates into a plateau for higher concentrations. To analyze, whether the saturation of the growth velocity above 88 µM is caused by a transition from transport- to reaction-limited growth as before, the concentration dependence of the growth velocity is investigated. From Equation 2.27 follows immediately that in the transport-limited case the nanowire growth velocity is proportional to the K_2PtCl_4-concentration for cluster and complexes, equally. In the case of reaction-limitation by a thermally activated process, according to collision theory the reaction turnover is also proportional to the concentration. This means that $v_\mathrm{g}/c_\mathrm{2c}$ should depend only on the temperature. From the fits in Figure 2.10 a $v_\mathrm{g}/c_\mathrm{2c}$-ratio of 0.84 nm/sµM for $T = 298\,\mathrm{K}$ and of 2.2 nm/sµM for $T = 316\,\mathrm{K}$ is read. In comparison, the linear segments of Figure 2.11 yield 0.5 nm/sµM for $T = 298\,\mathrm{K}$ and of 2 nm/sµM for $T = 316\,\mathrm{K}$. The high-temperature values show a good agreement, but at 298 K a relatively large difference is observed. It is concluded that the low-temperature curve is influenced by an additional mechanism other than the transport limitation discussed so far. Instead, this phenomenon is attributed to an increased amount of K^+ and Cl^- ions,

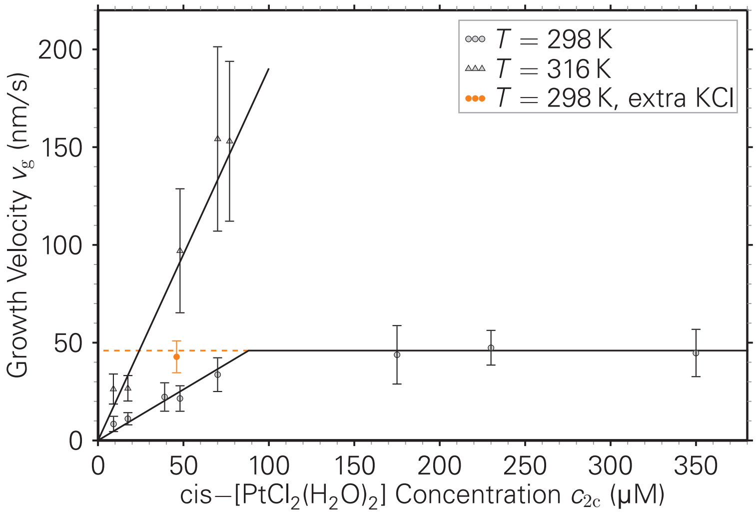

Figure 2.11: Measured nanowire growth velocity as a function of the cis−[$PtCl_2(H_2O)_2$] concentration at the temperatures 298 K and 316 K. The lines are linear fits through the origin and a fitted constant for 298 K and above 88 µM. Reprinted with permission from [21]. Copyright 2012 American Chemical Society.

introduced by adding K_2PtCl_4 to the solution. Among others, a possible explanation for the observations is a catalytic effect of additional potassium ions, which increases the reaction rate. Similar effects have also been observed for different materials [81, 82]. The presumed boost in the reaction rate should saturate at a certain potassium concentration, similar as reported by Peter et al. [83]. A second possibility is an increased AC electro-osmotic fluid flow, which is discussed thoroughly in section 2.6. The induced fluid flow is thought to boost the transport of complexes and/or clusters, which thereby allows for a growth velocity above the transport limit discussed here.

To prove the claim that the additional potassium (and/or chloride) ions are responsible for the increased wire growth velocity, an additional experiment was conducted, in which extra KCl was added to the solution. The ion excess caused the nanowire growth velocity to increase to the plateau level within the standard deviation. The extension of the plateau to much lower concentrations, cf. Figure 2.11, is a strong indicator supporting this idea. In this view, the 316 K curve shows the linear, transport-limited growth behavior and the 298 K curve shows in fact the influence of cointroduced ions on the nanowire growth velocity.

Summary Analyzing various nanowire morphologies grown under different experimental conditions revealed that wire morphologies grown with large particle concentrations in the assembly zone are in good agreement with the simulated distribution of the nanowire growth velocity along the wires circumference.

The presented model, covering particle transport through diffusion and dielectrophoretic migration, is in good qualitative agreement with experimentally measured nanowire growth velocities. Particularly the results in the high-temperature regime fit well to the transport-limited growth kinetics. From the low-temperature behavior it is concluded that the limitation of the growth reaction happens by a thermally activated process. The corresponding activation energy of 1.80 eV was determined by a fit and is in a reasonable range for electrochemical reactions.

Quantitatively, however, the theoretical growth velocities are about 20 times smaller than those from experiment. Considering that the modeling uncertainties of the boundary conditions were estimated by conservative assumptions, this result is even more astonishing. To solve this quantitative contradiction and the issue of morphological differences, an additional material transport mechanism is necessary. For instance an electro-kinetic fluid motion as considered by Gierhart et al. [79] could be responsible for larger experimental growth velocities.

2.4 FLUID FLOW CAUSED BY DIELECTROPHORESIS

As proposed in section 2.3, the discrepancy between simulated and measured nanowire growth velocity could be due to a fluid flow, which propels the transport of wire-forming species, i.e. complexes or metal clusters. When considering an additional fluid flow, the total flux (Equation 2.14b on page 16) is extended by a convective contribution to

$$\mathbf{j} = -D\,\nabla c - \frac{D\,c}{k_\mathrm{B}\,T}\,\nabla\psi + c\,\mathbf{v}, \tag{2.36}$$

where $\mathbf{v}$ is the fluid velocity vector. The boundary conditions are unaffected by this extension. For the electric potential (Equation 2.20) and its boundary conditions no adaptations are required. To model the fluid velocity, the Navier–Stokes equation for incompressible fluids is employed

$$\rho_\mathrm{m}\left(\frac{\partial\mathbf{v}}{\partial t} + (\mathbf{v}\cdot\nabla)\,\mathbf{v}\right) = -\nabla p + \eta\,\Delta\mathbf{v} + \mathbf{f}, \tag{2.37a}$$

$$\nabla\cdot\mathbf{v} = 0, \tag{2.37b}$$

with pressure p and the mass density ρ_m. As a further simplification, ρ_m is assumed to be independent of the ion (salt) concentration. The body force, $\mathbf{f}$, describes the external forces acting on the fluid. In this section, the scenario that DEP is the major drive for the presumed fluid flow is discussed. In fact, the DEP force acts only on the dielectric particles in the solution, which drives their motion relative to the fluid. In the stationary limit, the DEP force equals the drag force, which in turn acts on neighboring fluid molecules. By momentum transfer, the forces are propagated to the entire fluid. In the continuum description, the body force is therefore given by

$$\mathbf{f} = -c\,\nabla\psi_\mathrm{DEP} = \frac{\alpha\,c}{2}\,\nabla\,(\nabla\varphi)^2\,. \tag{2.38}$$

The boundary conditions of the flow problem are chosen as no-slip condition ($\mathbf{v} = 0$) at the electrodes and at the system cut-off boundaries. Thus, the system is closed (no in/out flow) and the pressure can only be determined up to a constant offset. To remove

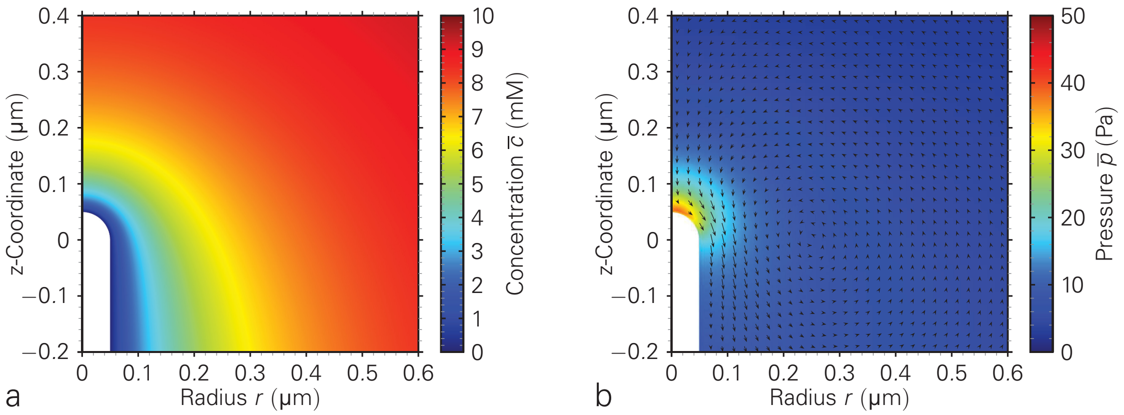

Figure 2.12: Numerical solution of the stationary transport of Pt-complexes in the vicinity of the nanowire tip. The model includes diffusion, migration and fluid flow due to the dielectrophoretic attraction, Equation 2.36. In comparison to the model without fluid flow, the stationary concentration profile of Pt-complexes (a) is nearly unchanged. The fluid flow (b) shows a vortex at $z \approx 0$ and $r \approx 250\,\mathrm{nm}$ with a maximum fluid velocity of about 50 µm/s in the vicinity of the nanowire tip. The fluid pressure is strongly localized at the nanowire tip.

this degree of freedom, the pressure at one point on the counter electrode is fixed to zero.

In the following, the discussion of the axially symmetric nanowire geometry (cf. Figure 2.6b on page 15) is continued and an additional DEP induced fluid flow is included in the model. To simplify the calculations, as before, all system variables are discussed in the asymptotic, time-average limit. To characterize the Reynolds number of this flow problem, the characteristic system length of the geometry is estimated by $\ell \approx 100\,\mathrm{nm}$. Utilizing the simulation parameters given in Table 2.2 on page 19, from preparatory simulations the fluid flow velocity is known to fulfill $v < 0.1\,\mathrm{mm/s}$, which yields

$$Re = \rho_\mathrm{m}\, v\, \ell/\eta \lesssim 10^{-5}. \tag{2.39}$$

Since the Reynolds number is very small, the inertial term in Equation 2.37 can be neglected, such that the time-average of the Navier–Stokes equation is given by

$$\eta\, \Delta\bar{\mathbf{v}} = \nabla\bar{p} - \bar{\mathbf{f}}, \tag{2.40}$$

in which the bar denotes the time-average.

Again, the two cases of platinum complexes on the one hand and platinum clusters on the other hand are discussed. Figure 2.12 shows for the platinum complexes the spatial concentration distribution as well as fluid flow velocities and the pressure field. Comparing Figure 2.7 with Figure 2.12a no difference can be observed. In fact, the concentration profiles differ by no more than 0.2 %. Also the boost of the particle flux and thus the increase of the nanowire growth velocity by the fluid flow is negligible.

Similarly, in the case of clusters, the fluid flow driven by the dielectrophoretic force is too small (in the order of 1 nm/s) to affect the stationary concentration profile of the clusters, and thereby the simulated nanowire growth velocity.

In summary, a fluid flow caused by a dielectrophoretic attraction of clusters or complexes is by far too slow to explain the observed discrepancies between theory and experiments. An alternative source of fluid motion could be the AC electro-osmosis, which is discussed in section 2.6. To calculate the AC electro-osmotic fluid flow, a detailed model of the ion transport in AC electric fields is developed first.

2.5 ION TRANSPORT UNDER HIGH AC ELECTRIC FIELDS

2.5.1 Model equations for ion transport

The consideration of the ion transport serves two purposes. First, it is necessary to determine the time-dependent space charge density and its implications on the electric field. Both quantities form the foundation to calculate the AC electro-osmotic fluid flow, which is presumed to resolve the contradiction between theory and experiments concerning the DEP based nanowire growth velocities (cf. section 2.4). The second application is the DENA type of nanowire growth itself. Different from the DEP mechanism, during the directed electrochemical nanowire assembly ions form the nanowire, cf. section 2.1. The transport of these precursor ions is governed by the model equations presented in this section.

The transport of ions in the solution is driven by migration and diffusion, as in section 2.3.2. To increase the clarity of presentation, equations 2.14a and 2.14b are repeated

$$\frac{\partial}{\partial t} c_i = -\nabla \cdot \mathbf{j}_i, \tag{2.41a}$$

$$\mathbf{j}_i = -\frac{D_i}{k_\mathrm{B} T} c_i \nabla(\mu_i + z_i\, e\, \varphi), \tag{2.41b}$$

in which the particle potential has been substituted with $\psi = z_i\, e\, \varphi$. The diffusion flux has been rewritten to a migration due to gradients in the chemical potential μ_i. The index $i = 1, 2$ labels cations and anions, z_i is the respective charge number, and e is the elementary charge. Due to the evolving ion fluxes within the solution a charge density $\rho = F \sum z_i\, c_i$ occurs, which enters the Poisson equation

$$\nabla^2 \varphi = -\frac{\rho}{\varepsilon} = -\frac{F}{\varepsilon}(z_1\, c_1 + z_2\, c_2). \tag{2.41c}$$

The set of PDEs, Equation 2.41, is known as Poisson–Nernst–Planck (PNP) equations.

Due to the small curvature radii, already at moderate applied voltages,the electric field at the nanowire tip often exceeds 1×10^8 V/m. In the limit of such high electric fields, the ion concentration in the vicinity of the nanoelectrode can easily surpass the bulk concentration c_b by several orders of magnitude [84, 85]. To establish a physically inspired upper limit to the ion concentration in the solution, a chemical potential of the form

$$\mu_i = k_\mathrm{B} T \log \frac{c_i}{c_\mathrm{max} - (c_1 + c_2)} \tag{2.42}$$

is adopted. The term in the denominator (introduced by Bikerman [86]) considers the volume exclusion effect at high ion concentrations. The value of the maximum concentration c_{max} in Equation 2.42 is not well known. A wide range of approximations exists for c_{max} and the corresponding mean spacing of crowded ions $a_{\mathrm{c}} = c_{\mathrm{max}}^{-1/3}$. One could estimate a_{c} by the diameter of an ion with its solvation shell, which is typically in the order of 0.5 nm [78]. However, due to ion-ion correlations the Bjerrum length ($\ell_{\mathrm{B}} = e^2/(4\,\pi\,\varepsilon\,k_{\mathrm{B}}\,T)$) could be appropriate as well [85]. For water at ambient conditions this yields $\ell_{\mathrm{B}} \approx 0.7$ nm. In all following calculations, the value of $c_{\mathrm{max}} = 9.3$ M is used, which corresponds to the solubility of potassium chloride at 293 K [87]. The respective mean ion spacing is about 0.6 nm and thus at an intermediate level.

The dielectric property of aqueous solutions is modeled by the dielectric constant of water, $\varepsilon_{\mathrm{r}} = 80$. For low ion concentrations this assumption is justified: according to an empirical relation by Stogryn [88], a salt concentration of up to 0.1 N changes the dielectric constant only about 2.6 %. However, for concentrations in the order of c_{max} the dielectric constant is considerably reduced. Similarly, for large electric field strength $\gtrsim 5 \times 10^8$ V/m the dielectric constant is also known to decrease [89, 90]. Given the relatively simple modeling of the ion crowding and the discussed parameter uncertainties, the results have to be considered with caution, when a pronounced double layer is formed.

To determine the flux boundary conditions the ions are assumed to be chemically inert, which results in blocking electrodes, $\mathbf{j}_i \cdot \mathbf{n} = 0$. The model is further simplified by two assumptions: first, all occurring ion types have approximately the same diffusion coefficient $D_1 \approx D_2$, and second the electrolyte shall be binary, which means $z = z_1 = -z_2$. In the case of a KCl solution, this assumption is well-fulfilled and allows for a very efficient numerical simulation scheme, as presented in sections 3.3 and 3.4. The value of $D = 4.3 \times 10^{-10}$ m^2/s is estimated by employing Equation 2.15 and as an upper estimate for the hydrodynamic radius of the ions with its hydration shell $r_{\mathrm{p}} = 0.5$ nm is used [78].

For a first simplified view on the subject, the spherical electrode geometry (cf. Figure 2.6a on page 15) is reused. The AC voltage $V(t) = V_0 \sin(2\,\pi\,f\,t)$ is applied to the inner electrode, whereas the outer electrode is grounded. The resulting boundary conditions for the Poisson equation are

$$\varphi(r_1, t) = V(t), \quad \varphi(r_2, t) = 0. \tag{2.43}$$

These conditions differ from those used in several other studies [46, 48, 56], in which a mixed boundary condition is chosen to account for an additional capacity owing to the presence of a compact double layer or thin oxide layer on the electrode surface. Considering the case of a growing noble metal nanowire, the occurring interface phase is expected to consist of chloride or oxide with a thickness in the order of one monolayer. The capacity corresponding to a thin dielectric layer (d, thickness; ε_{l}, relative dielectric constant of the layer) at the electrode surface is given by

$$C_{\mathrm{l}} = 4\,\pi\,\varepsilon_0\,\varepsilon_{\mathrm{l}}\,r_1^2/d. \tag{2.44}$$

The capacity of the electrolyte volume in the considered spherical setup is

$$C = 4\,\pi\,\varepsilon_0\,\varepsilon_\mathrm{r}\frac{r_1\,r_2}{r_2 - r_1}. \tag{2.45}$$

In a series circuit of C_l and C, the thin layer capacity is omissible as long as $d\,\varepsilon_\mathrm{r} \ll r_1\,\varepsilon_\mathrm{l}$, which is well-fulfilled for the monolayer assumption.

Starting from some initial conditions for the ion concentration profiles, e.g. $c_1 = c_2 = c_\mathrm{b}$, after some transient time the system approaches an asymptotic periodic regime, which is characterized by

$$c_1(r,t) = c_2(r,t - \mathcal{T}/2), \tag{2.46}$$

where $\mathcal{T} = 1/f$ is the oscillation period of the applied voltage. In all simulations carried out, this asymptotic regime was determined. The numerical details of how the PNP equations, Equation 2.41, were solved numerically are presented in sections 3.3 and 3.4.

2.5.2 Spatiotemporal solution of the PNP equations

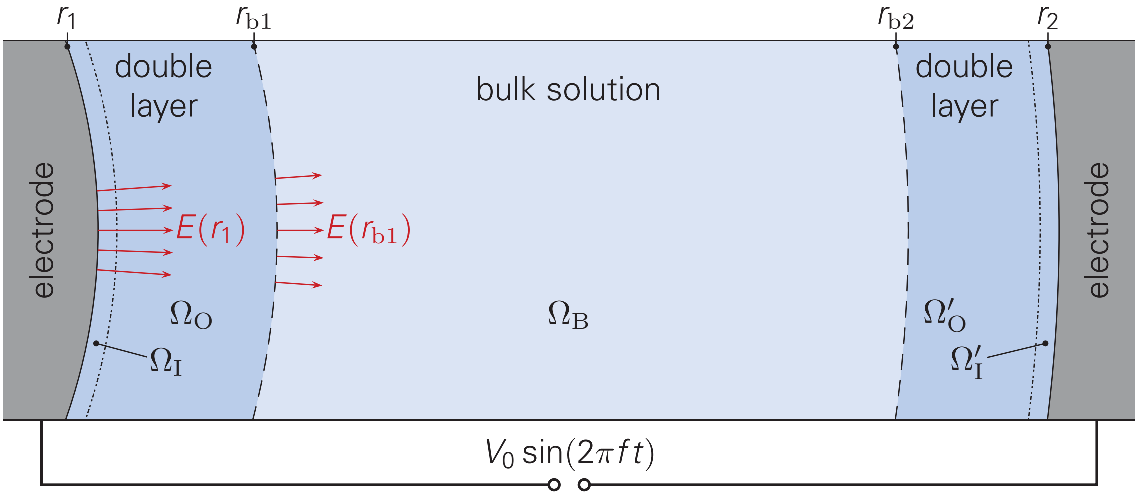

Figure 2.13: Under the influence of an AC electric field, a dynamical double layer forms at the electrode surfaces. Dotted lines mark the very thin inner layers Ω_I at the electrode surfaces with high accumulation of attracted ions. Within the much thicker outer layers Ω_O (dashed lines), the repelled ions are strongly depleted. The bulk zone Ω_B between the radii $r_{\mathrm{b}1}$ and $r_{\mathrm{b}2}$ is practically charge-neutral. Besides the electric field decay $\propto 1/r^2$, the electric field at radius $r_{\mathrm{b}1}$ is additionally reduced due to screening by the double layer.

In this section, the analytical and numerical solutions of the PNP equations are presented and important measures for their characterization are derived. These results are the input for the simulation of the AC electro-osmotic fluid flow, cf. section 2.6. Hence, major insights from this section are used later to optimize the nanowire assembly schemes through DEP and ACEO.

The solution of the PNP equations have a typical spatial pattern. Figure 2.13 schematically shows the formation of the dynamical double layer near the electrode surfaces. The boundaries of the double layers are denoted by r_{b1} and r_{b2}, respectively. The bulk zone between these radii is practically charge-neutral since both ion species have a concentration very close to the bulk concentration. The charged region near the nanoelectrode, $r_1 < r < r_{\mathrm{b1}}$, consists of a very thin inner layer with a high concentration of attracted ions and an outer layer with a depletion of the repelled ions. For low frequencies, the ion concentration in the inner layer can be several orders of magnitude larger than the bulk value. When the concentration reaches $c_{\max}$, additional, attracted ions increase the layer thickness rather than the ion concentration, similar to the DC observations by Lopez et al. [91].

Figure 2.14 shows the asymptotic concentration profiles near the inner nanoelectrode at different points of time with respect to the oscillation period $\mathcal{T} = 1/f$. The simulation parameters were chosen as $f = 100\,\mathrm{kHz}$ and a bulk concentration of $c_{\mathrm{b}} = 0.1\,\mathrm{mM}$ in panels (a) and (b), and of $c_{\mathrm{b}} = 1\,\mathrm{mM}$ in panel (c). In the first half-period ($t = 1/8\,\mathcal{T}$ and $t = 3/8\,\mathcal{T}$) the applied voltage is positive. During that time, the cations in the solution are repelled up to about 200 nm. The depleted region of the solution corresponds to the outer layer, Ω_{O} in Figure 2.13. In the second half period ($t = 5/8\,\mathcal{T}$ and $7/8\,\mathcal{T}$) the voltage is negative and the cations are attracted to the electrode. For $c_{\mathrm{b}} = 0.1\,\mathrm{mM}$ a layer of a few angstrom thickness forms at the electrode, in which the cation concentration surpasses the bulk concentration by several orders of magnitude. For higher bulk concentrations, crowding of ions occurs at the electrode surface as shown in Figure 2.14c. The thickness of the corresponding high-concentration layer reaches in this case about 1 nm. In Figure 2.13 this radius range corresponds to the inner layer, Ω_{I}. The anions show the same concentration profiles as the cations, only with a time shift of $\mathcal{T}/2$, cf. Equation 2.46.

The highly different ion concentrations result in a large space charge density ρ near the electrodes, which causes a strong screening of the electric field in the bulk zone. Commonly, this effect is expressed by a voltage drop V_{d} at the electric double layer. To analyze this voltage drop, the Poisson equation, Equation 2.41c, for the three important one-dimensional systems, plate capacitor ($d = 0$), the cylinder capacitor ($d = 1$), and the spherical capacitor ($d = 2$),

$$\frac{\partial}{\partial r}\left[r^d \frac{\partial}{\partial r}\varphi(r)\right] = -r^d \frac{\rho(r)}{\varepsilon} \tag{2.47}$$

is solved with respect to the boundary conditions Equation 2.43. Integration of Equation 2.47 yields

$$-\frac{\partial}{\partial r}\varphi(r) = E(r) = r^{-d}\left(Q_0 + \int_{r_1}^{r} \mathrm{d}r' r'^d \frac{\rho(r')}{\varepsilon}\right), \tag{2.48}$$

with the integration constant Q_0. In a physical interpretation, Q_0 is proportional to the amount of charges, which reside on the inner electrode, outside of the solution volume. After a second integration of Equation 2.48, the electric potential φ is obtained, for which the first boundary condition $\varphi(r_1) = V(t)$ is applied directly, such that

$$\varphi(r) = V(t) - \int_{r_1}^{r} \mathrm{d}r'' \left[r''^{-d}\left(Q_0 + \int_{r_1}^{r''} \mathrm{d}r'\, r'^d\, \frac{\rho(r')}{\varepsilon}\right)\right]. \tag{2.49}$$

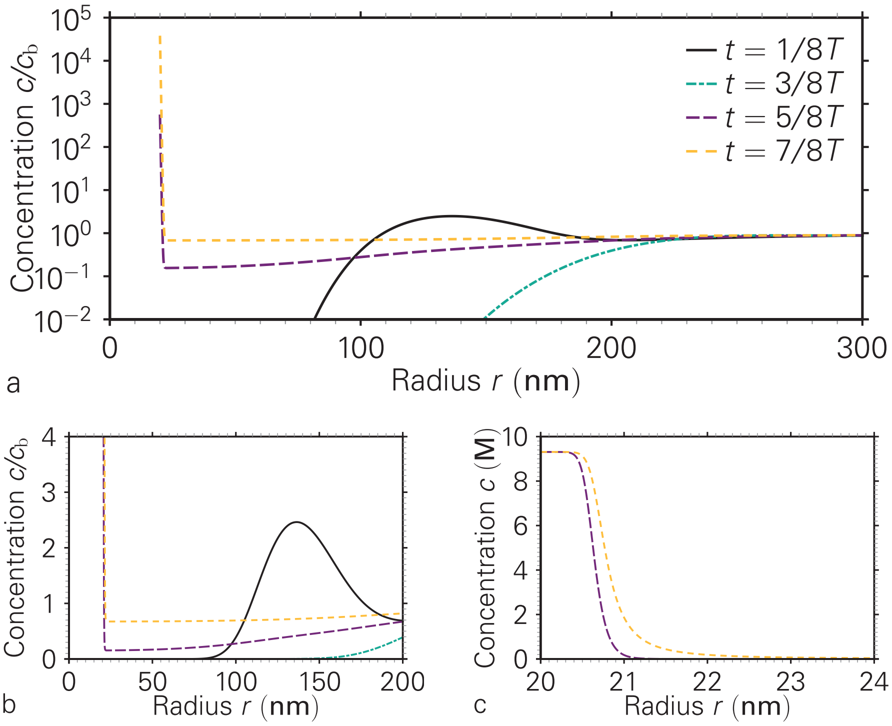

Figure 2.14: Asymptotic periodic cation concentration profiles around a spherical nanoelectrode resulting from an applied harmonic voltage signal, $V(t) = V_0 \sin(2\pi t/T)$. Panels (a) and (b) show the versatile concentration profiles for $c_\mathrm{b} = 0.1\,\mathrm{mM}$. In the first half period the cations are repelled from the electrode. In the second half period the cations accumulate in the inner layer of a few Angstrom thickness. For the case of a higher bulk concentration of $c_\mathrm{b} = 1\,\mathrm{mM}$, panel (c), a concentration plateau at $c = c_\mathrm{max}$ develops due to ion crowding at the electrode surface. Parameters: $V_0 = 5\,\mathrm{V}$, $r_1 = 20\,\mathrm{nm}$, $r_2 = 2\,\mathrm{\mu m}$, $f = 100\,\mathrm{kHz}$.

The nested integrals in Equation 2.49 cover a triangular-shaped integration domain in the $r' \times r''$ space. With the due adaption of the integration boundaries the two can be commutated

$$\varphi(r) = V(t) - Q_0 \int_{r_1}^{r} \mathrm{d}r'' r''^{-d} - \int_{r_1}^{r} \mathrm{d}r' \int_{r'}^{r} \mathrm{d}r'' \left(\frac{r'}{r''}\right)^{d} \frac{\rho(r')}{\varepsilon}. \tag{2.50}$$

To simplify the notation the homogeneous solution of the potential with respect to d is introduced as $h_d(r) = \int_{r_1}^{r} \mathrm{d}r'\, r'^{-d}$,

$$\varphi(r) = V(t) - Q_0\, h_d(r) - \int_{r_1}^{r} \mathrm{d}r'\, r'^{d} \left[h_d(r) - h_d(r')\right] \frac{\rho(r')}{\varepsilon}. \tag{2.51}$$

From the second boundary condition, $\varphi(r_2) = 0$, and employing the electrical neutrality of the whole electrolyte

$$\int_{r_1}^{r_2} \mathrm{d}r'\, r'^{d} \rho(r') = 0, \tag{2.52}$$

Q_0 can be determined as

$$Q_0 = \frac{V(t)}{h_d(r_2)} + \int_{r_1}^{r_2} \mathrm{d}r'\, r'^{d} \frac{h_d(r')}{h_d(r_2)} \frac{\rho(r')}{\varepsilon}, \tag{2.53}$$

which finally yields

$$\begin{aligned}\varphi(r) = V(t)\,\frac{h_d(r_2) - h_d(r)}{h_d(r_2)} - \frac{h_d(r)}{h_d(r_2)} \int_{r_1}^{r_2} \mathrm{d}r'\, r'^d\, h_d(r')\, \frac{\rho(r')}{\varepsilon} \\ - \int_{r_1}^{r} \mathrm{d}r'\, r'^d \left[h_d(r) - h_d(r')\right] \frac{\rho(r')}{\varepsilon}.\end{aligned} \tag{2.54}$$

The first term on the r.h.s. of Equation 2.54 is referred to as external potential that can be observed in e.g. vacuum or a solid dielectric. The second term is caused by additionally induced charges on the electrode, resulting from interactions with the space charge density. Both, first and second term of the potential, have the form of the homogeneous (general) solution of the Laplace equation (= Poisson equation without charge density). For the spherical capacitor ($d = 2$) this is a $1/r$ dependence, for a plate capacitor ($d = 0$) this is the well-known linear dependence. The last term exhibits a complex radial dependence and reflects the particular solution of the Poisson equation, i.e. it is the potential change immediately caused by the space charges.

The electric potential in the charge-free bulk zone, $r_{\mathrm{b1}} < r < r_{\mathrm{b2}}$, is of particular interest. In this region there holds $\rho = 0$ so that the integrals over this domain vanish. Equation 2.54 can therefore be simplified to

$$\varphi_{\mathrm{asym}}(r, t) = \frac{h_d(r_2) - h_d(r)}{h_d(r_2)} \left[V(t) - V_{\mathrm{d}}(t)\right] + V_{\mathrm{o}}(t), \tag{2.55}$$

with

$$V_{\mathrm{d}}(t) = h_d(r_2) \int_{r_1}^{r_{\mathrm{b1}}} \mathrm{d}r'\, r'^d\, \frac{-\rho(r')}{\varepsilon} + \int_{r_1}^{r_{\mathrm{b1}}} \mathrm{d}r'\, r'^d\, h_d(r') \frac{-\rho(r')}{\varepsilon} + \int_{r_{\mathrm{b2}}}^{r_2} \mathrm{d}r'\, r'^d\, h_d(r')\, \frac{-\rho(r')}{\varepsilon} \tag{2.56a}$$

$$V_{\mathrm{o}}(t) = h_d(r_2) \int_{r_1}^{r_{\mathrm{b1}}} \mathrm{d}r'\, r'^d\, \frac{-\rho(r')}{\varepsilon} + \int_{r_{\mathrm{b2}}}^{r_2} \mathrm{d}r'\, r'^d\, h_d(r')\, \frac{-\rho(r')}{\varepsilon} \tag{2.56b}$$

In the limit of a thin double layer ($r_2 - r_{\mathrm{b2}} \ll r_2 - r_1$), $h_d(r)$ can be linearized near the electrodes $h_d(r) \approx h_d(r_i) + (r - r_i)/r_i^d$. Together with the charge balance, Equation 2.52, this yields

$$V_{\mathrm{d}}(t) \approx \int_{r_1}^{r_{\mathrm{b1}}} \mathrm{d}r'\, \frac{r'^d}{r_1^d}\,(r' - r_1)\, \frac{-\rho(r')}{\varepsilon} + \int_{r_{\mathrm{b2}}}^{r_2} \mathrm{d}r'\, \frac{r'^d}{r_2^d}\,(r' - r_2)\, \frac{-\rho(r')}{\varepsilon}, \tag{2.57a}$$

$$V_{\mathrm{o}} \approx \int_{r_{\mathrm{b2}}}^{r_2} \mathrm{d}r'\, \frac{r'^d}{r_2^d}\,(r' - r_2)\, \frac{-\rho(r')}{\varepsilon}. \tag{2.57b}$$

For plate capacitors ($d = 0$) the charge density is antisymmetric at the electrodes, $\rho(r - r_1, t) = -\rho(r_2 - r, t)$, which results in a symmetric voltage drop $V_{\mathrm{o}} = V_{\mathrm{d}}/2$. In contrast, for nanoelectrodes ($d > 0$) the voltage drop over the double layers is highly asymmetric, i.e. $V_{\mathrm{o}} \ll V_{\mathrm{d}}$. Correspondingly, the potential outside the charge layer behaves like the external potential, but with a different apparent voltage. Typically, the voltage drop has a phase shift relative to the externally applied voltage. Consequently, the voltage drop does not lower the applied voltage at all times. However, the RMS-value of the superimposed voltage is reduced. The nonlinear character of the PNP equations gives rise to additional higher-order oscillations in $V_{\mathrm{d}}(t)$. The spatial dependence of the potentials in Equation 2.54 and Equation 2.55 for the spherical case ($d = 2$) at time $t = 3/8\,\mathcal{T}$ are compared in Figure 2.15a. The asymptotic potential approximation is valid for $r \gtrsim 200\,\mathrm{nm}$.

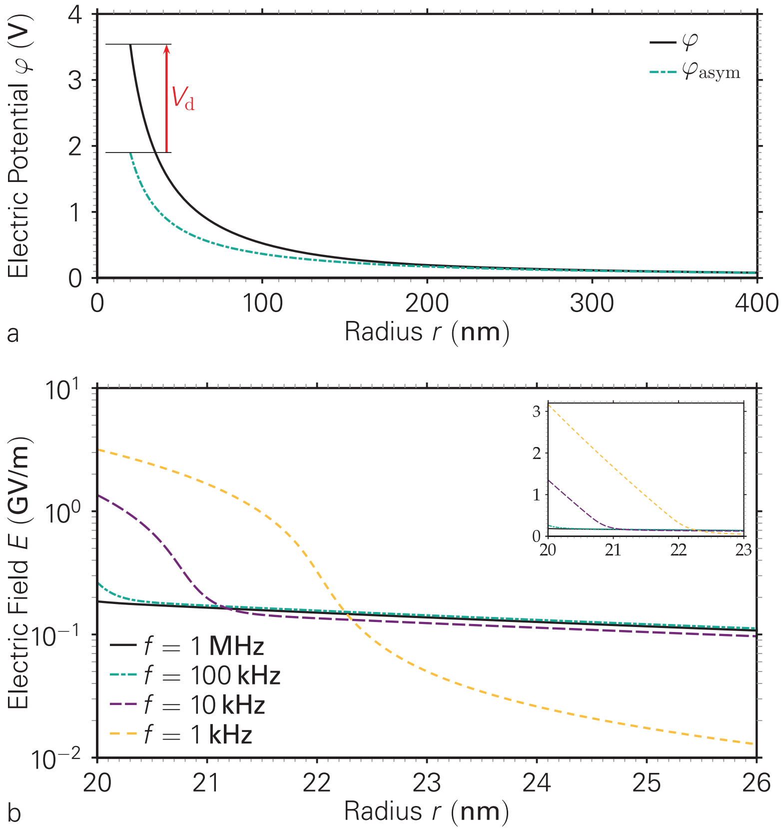

Figure 2.15: (a) Comparison of the electric potentials φ and φ_asym for $f = 100\,\mathrm{kHz}$ according to Equation 2.54 and Equation 2.55, respectively. The potential difference at $r = r_1$ corresponds to the potential drop V_d. The curves practically agree for $r > r_\mathrm{b1} \approx 200\,\mathrm{nm}$. (b) Radial dependence of electric field strength for various frequencies. At a high frequency of $f = 1\,\mathrm{MHz}$, the induced charge is very small so that the curve practically agrees with the external electric field. The inset reveals a nearly linear decay of the electric field close to the electrode at low frequencies, which reflects a plateau in the counter-ion concentration and corresponding charge density due to ion crowding. Parameters: $t = 3/8\,\mathcal{T}$, $c_\mathrm{b} = 0.1\,\mathrm{mM}$, $V_0 = 5\,\mathrm{V}$, $r_1 = 20\,\mathrm{nm}$.

The interpretation of the three potential contributions of Equation 2.54 can be transferred to the electric field as well

$$E(r) = \frac{1}{r^d\, h_d(r_2)} \left[V(t) + \int_{r_1}^{r_2} \mathrm{d}r'\, r'^d\, h_d(r')\, \frac{\rho(r')}{\varepsilon} + h_d(r_2) \int_{r_1}^{r} \mathrm{d}r'\, r'^d\, \frac{\rho(r')}{\varepsilon} \right]. \tag{2.58}$$

As before, the three terms of the sum in Equation 2.58 have a physical interpretation: the first is the external electric field, the second is the field enhancement due to additional charges on the electrodes, which guarantee the potential boundary conditions. The third corresponds to the field screening due to the space charge density in the solution. Since these modifications of the electric potential and field occur for all three types of one-dimensional systems, it is concluded that this is a general property of the underlying PNP equations and not of the geometry.

The spatial distribution of the electric field in the spherical case is compared in Figure 2.15b for different space charge density resulting from a variation of the frequency. For very high frequencies the space charge density is found to be negligible in the asymptotic limit. Therefore, the curve for $f = 1\,\mathrm{MHz}$ is visually indistinguishable from the external electric field, cf. Equation 2.58. At lower frequencies the space charge density is more prominent and thus the second and third term of Equation 2.58 become important. The field enhancement is noticeable only in the immediate vicinity of the electrode. At frequencies of 1 kHz and 10 kHz, the nearly linear decay of the field strength (cf. inset in Figure 2.15b) within a thin layer of a few nanometer thickness is due to the nearly constant charge density within the corresponding ion crowding zone (Figure 2.14c). Outside this zone, the electric field is strongly diminished due to screening.

2.5.3 Frequency dependence of the ion transport

As suggested by Figure 2.15b, the ion distribution and thus the resulting electric field and potential have a strong dependence on the applied AC frequency. In fact, the frequency is the single-most important parameter to adjust the ion concentrations in the dynamical double layer and thereby also the electric field and potential in the whole electrolyte. Consequently, the detailed understanding of the frequency effects is crucial for the assessment of the AC electro-osmotic fluid flows and the mechanism of direct electrochemical nanowire assembly.

To introduce the topic, the frequency dependence of the total electric field at a spherical electrode is depicted in Figure 2.16. Therein three frequency ranges can be identified. At a very high frequency, the time for accumulation or depletion of ions at the electrode surface is very small. Therefore, the ion concentration at the electrode surface differs only slightly from the bulk value. According to Equation 2.58, this results in a negligible field screening and field enhancement and thus the total electric field equals the external electric field.

On the other hand, in the low-frequency limit, the time for ion transport is sufficient to reach a quasi-stationary concentration profile near the electrode surface. This charge

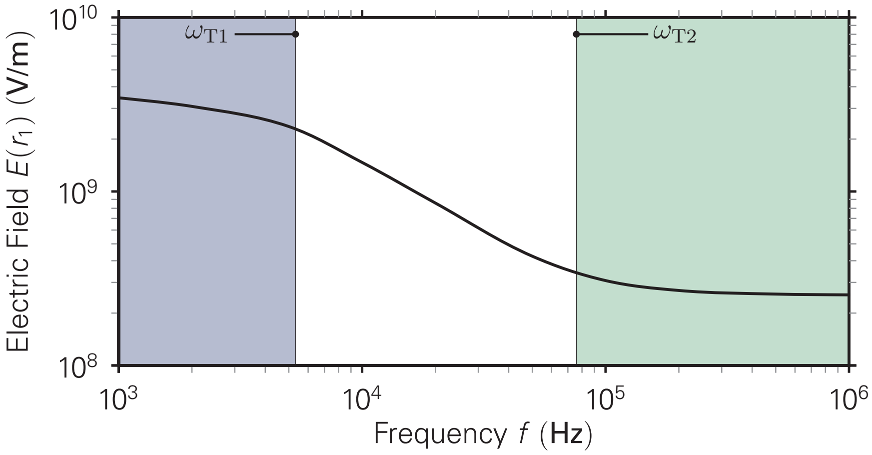

Figure 2.16: The frequency behavior of the first harmonic amplitude of the total electric field at the nanowire tip exhibits three regions. Below the lower transition frequency ω_{T1}, a strong field enhancement leads to field strengths much higher than the external electric field. Above the upper transition frequency ω_{T2}, the field enhancement does not take place and the total electric field equals the external electric field. In the intermediate region between the two transition frequencies, the total electric field at the nanowire tip drops with 10 dB/decade.

accumulation is accompanied by a nearly complete field screening within the bulk zone and a strong field enhancement at the electrode surface, see Equation 2.58.

The intermediate frequency range is characterized by a complex interplay of ion accumulation and its effect on the electric field, examples of which are shown in Figure 2.14. To describe the frequency behavior, two characteristic frequencies are introduced to separate the three frequency ranges: the lower transition frequency ω_{T1} and the upper transition frequency ω_{T2}, cf. Figure 2.16. In the following, the two transition frequencies and analytical expressions for several electric variables are derived. Thereafter, the more complex effects of the frequency on the charge density are discussed.

High-frequency behavior

To determine the upper transition frequency ω_{T2}, the total charge Q that is attracted to the double layer is considered (cf. Figure 2.13). Denoting the double layer volume by $\Omega_{\mathrm{s}} = \Omega_{\mathrm{I}} \cup \Omega_{\mathrm{O}}$ and its boundaries by $\partial\Omega_{\mathrm{s}}$, the total charge is given by

$$Q = \int_{\Omega_{\mathrm{s}}} \mathrm{d}V \, \rho = \int_{\Omega_{\mathrm{s}}} \mathrm{d}V \, \nabla \cdot \varepsilon \, \mathbf{E} = \oint_{\partial\Omega_{\mathrm{s}}} \mathrm{d}A \, \mathbf{n} \cdot \varepsilon \, \mathbf{E}. \tag{2.59}$$

For all one-dimensional cases, the integrand in the surface integral in Equation 2.59 is constant. Thus introducing the cross-section area $A_d(r) \propto r^d$ yields

$$Q(t) = \varepsilon \, E(r_{\mathrm{b1}}, t) \, A_d(r_{\mathrm{b1}}) - \varepsilon \, E(r_1, t) \, A_d(r_1). \tag{2.60}$$

On the other hand, the time derivative $\partial Q/\partial t$ is affected by the ion fluxes through the domain boundaries

$$\frac{\partial}{\partial t}Q = \int_{\Omega_\mathrm{s}} \mathrm{d}V \sum_i z_i\, F \frac{\partial}{\partial t} c_i = \int_{\Omega_\mathrm{s}} \mathrm{d}V\, z_i\, F\, \nabla \cdot \mathbf{j}_i = \oint_{\partial\Omega_\mathrm{s}} \mathrm{d}A\, z_i\, F\, \mathbf{n} \cdot \mathbf{j}_i, \tag{2.61}$$

which, with respect to the blocking electrode boundary condition $j_i(r_1) = 0$, simplifies to

$$\frac{\partial}{\partial t}Q(t) = -A_d(r_{\mathrm{b}1})\, F \sum_i z_i\, j_i(r_{\mathrm{b}1}, t). \tag{2.62}$$

Since at $r_{\mathrm{b}1}$ the ion concentrations are practically equal to the bulk concentrations, the diffusive contribution of the ion flux vanishes so that $j_1(r_{\mathrm{b}1}) = -j_2(r_{\mathrm{b}1}) = \frac{D\,z}{k_\mathrm{B} T}\, c_\mathrm{b}\, e\, E(r_{\mathrm{b}1})$, and finally

$$\frac{\partial}{\partial t}Q(t) = -A_d(r_{\mathrm{b}1})\, \frac{2\,D\,z}{k_\mathrm{B}\,T}\, e\, F\, c_\mathrm{b}\, E(r_{\mathrm{b}1}, t). \tag{2.63}$$

Combining the time derivative of Equation 2.60 with Equation 2.63 leads to

$$\frac{\partial}{\partial t}E(r_{\mathrm{b}1}, t) + \omega_{\mathrm{T}2}\, E(r_{\mathrm{b}1}, t) = \left(\frac{r_1}{r_{\mathrm{b}1}}\right)^d \frac{\partial}{\partial t}E(r_1, t), \tag{2.64}$$

where $\omega_{\mathrm{T}2} = 2\,z\,D\,e\,F\,c_\mathrm{b}/(\varepsilon\, k_\mathrm{B}\, T)$ is the upper transition frequency. The Fourier transform of the last equation reads

$$E(r_{\mathrm{b}1}, \omega) = \frac{\imath\,\omega}{\imath\,\omega + \omega_{\mathrm{T}2}} \left(\frac{r_1}{r_{\mathrm{b}1}}\right)^d E(r_1, \omega). \tag{2.65}$$

Equation 2.65 relates the electric field at the electrode surface to the electric field at the interface of the double layer and the bulk solution. The electric field inside the charge-free bulk zone ($r > r_{\mathrm{b}1}$) is proportional to the external electric field (cf. Equation 2.55) and therefore given by

$$E(r, \omega) = \frac{\imath\,\omega}{\imath\,\omega + \omega_{\mathrm{T}2}} \left(\frac{r_1}{r}\right)^d E(r_1, \omega). \tag{2.66}$$

Then from Equation 2.63 results the double layer charge as

$$Q(\omega) = \frac{-A_\mathrm{d}(r_1)\, \varepsilon\, \omega_{\mathrm{T}2}}{\imath\,\omega + \omega_{\mathrm{T}2}} E(r_1, \omega). \tag{2.67}$$

This means that for frequencies much higher than the upper transition frequency $\omega_{\mathrm{T}2}$, the amplitude of the accumulated charges diminish significantly and the phase lags by almost 90°.

Low-frequency approximation

To determine the lower transition frequency $\omega_{\mathrm{T}1}$, the low-frequency solution of the PNP equations is analyzed in more detail. It should be pointed out that in the limit of low frequencies the modified PNP equations (Equation 2.41a-c) converge to the modified

Poisson–Boltzmann equation with steric exclusion as discussed in Refs. [84, 92]. Notably, there are several other modifications like e.g. those in Ref. [93]. The different modifications, however, yield very similar results for the ion distribution.

In the quasi-stationary regime the ion fluxes become negligible

$$\mathbf{j}_i = -\frac{D\,c_i}{k_\mathrm{B}T}\nabla\left(\mu_i + z_i e\,\varphi\right) = 0, \tag{2.68}$$

which requires

$$\mu_i + z_i e\,\varphi = const. \tag{2.69}$$

Provided there is a sufficiently large number of ions in the solution, a complete screening of the electric field is established and hence the bulk region becomes practically field-free. Moreover, the ion concentration in the bulk region is close to the bulk concentration for both ion types. To simplify the model equations, the ion crowding is initially neglected, i.e. $\mu_i \approx k_\mathrm{B}T\,\log\left(c_i/c_\mathrm{b}\right)$. Under these conditions the ion concentration can be expressed as

$$c_i = -c_\mathrm{b}\exp\left(\frac{z_i\,e\,\varphi}{k_\mathrm{B}T}\right). \tag{2.70}$$

Inserting Equation 2.70 into the Poisson equation (Equation 2.41c) yields the well-known, traditional Poisson–Boltzmann equation

$$\nabla\cdot\nabla\varphi = \frac{-\rho}{\varepsilon} = \frac{2\,z\,F\,c_\mathrm{b}}{\varepsilon}\sinh\left(\frac{z\,e\,\varphi}{k_\mathrm{B}T}\right), \tag{2.71}$$

which in its low voltage limit ($|V| \ll k_\mathrm{B}T/e$) is the foundation of Debye–Hückel–theory [43]. For a brief notation, the normalized potential $\hat{\varphi} = z\,e\,\varphi/k_\mathrm{B}T$ and the Debye length $\lambda_\mathrm{D} = \sqrt{\frac{\varepsilon\,k_\mathrm{B}T}{e\,F\,c_\mathrm{b}}}$ are introduced.

$$\nabla\cdot\nabla\hat{\varphi} = \frac{2}{\lambda_\mathrm{D}^2}\sinh\left(\hat{\varphi}\right) \tag{2.72}$$

For large applied voltages the double layer in the quasi-static regime is highly compressed (cf. Figure 2.14 on page 31). If the thickness of the double layer is small compared to the tip radius, the planar approximation ($\nabla^2 \approx \frac{\partial^2}{\partial r^2}$) is applicable for Equation 2.72,

$$\frac{\partial^2}{\partial r^2}\hat{\varphi} = \frac{2}{\lambda_\mathrm{D}^2}\sinh\left(\hat{\varphi}\right). \tag{2.73}$$

After multiplying a common integrating factor of $\frac{\partial}{\partial r}\hat{\varphi}$, the first integration yields

$$\left[\frac{\partial}{\partial r}\hat{\varphi}\right]^2 = 2\left[\frac{2}{\lambda_\mathrm{D}}\sinh\left(\hat{\varphi}/2\right)\right]^2 + k. \tag{2.74}$$

In the bulk zone, i.e. for $r_\mathrm{b1} - r_1 \ll r - r_1 \ll r_2 - r_1$, the electric field and the electric potential vanish, which determines the integration constant as $k = 0$. Root extraction of

Equation 2.74 requires a sign discussion: at the positive electrode a negative potential gradient develops and vice versa, i.e.

$$\frac{\partial}{\partial r}\hat{\varphi} = -\sqrt{2}\frac{2}{\lambda_\mathrm{D}}\sinh\left(\hat{\varphi}/2\right). \tag{2.75}$$

Solving Equation 2.75 by separation of variables gives

$$|\hat{\varphi}| = 4\,\mathrm{atanh}\exp\left(\frac{-\sqrt{2}\,(r-r_0)}{\lambda_\mathrm{D}}\right), \tag{2.76}$$

in which the integration constant r_0 is given through the boundary condition $\hat{\varphi}(r_1) = z\,e\,V/k_\mathrm{B}T$ such that

$$r_0 = r_1 + \frac{\lambda_\mathrm{D}}{\sqrt{2}}\log\tanh\left(\frac{z\,e\,|V|}{4\,k_\mathrm{B}T}\right). \tag{2.77}$$

The distribution found for the electric potential (Equation 2.76) is linked by Equation 2.70 directly to the ion concentrations. Particularly for large applied voltages, a thin layer forms at the electrode, in which the predicted ion concentration is above the previously defined maximum concentration c_max. This is clearly an artifact of the simplified model, which is also the reason for employing the modified chemical potential (Equation 2.42). Nevertheless, in the regions with a predicted ion concentration significantly below c_max, i.e. sufficiently far from the inner electrode, the crowding term in the chemical potential is negligible and the approximation yields good results.

To improve the quality of the analytical solution in the vicinity of to the inner electrode, the spatial region is divided into an inner and an outer subregion. In the inner subregion, a fully crowded layer with an ion concentration of c_max and 0, respectively, is assumed. For the outer subregion the Poisson–Boltzmann model is considered. The radius, which separates the two subregions, is defined as the critical radius r_c. The location of this critical radius cannot be expressed explicitly in advance to the following derivation. However, for the outer region one immediately reobtains the previous solution, Equations 2.70 and 2.76, since the boundary conditions for $r \gg r_\mathrm{b1}$ are unaffected. The integration constant r_0 changes to

$$r_0 = r_c + \frac{\lambda_\mathrm{D}}{\sqrt{2}}\log\tanh\left(\frac{z\,e\,\varphi_\mathrm{c}}{4\,k_\mathrm{B}T}\right). \tag{2.78}$$

Then, in the outer subregion $r \geq r_\mathrm{c}$ the electric potential is known, which determines the electric potential at the interface $r = r_\mathrm{c}$ as critical electric potential

$$\varphi_\mathrm{c} = \frac{k_\mathrm{B}T}{z\,e}\,\mathrm{asinh}\left(\frac{c_\mathrm{max}}{2\,c_\mathrm{b}}\right). \tag{2.79}$$

Therefore, the space charge density can be expressed by

$$\rho = \begin{cases} -z\,F\,c_\mathrm{max}, & \varphi \geq \varphi_\mathrm{c} \\ -2\,z\,F\,c_\mathrm{b}\sinh\left(\frac{z\,e\,\varphi}{k_\mathrm{B}T}\right), & |\varphi| < \varphi_\mathrm{c} \\ z\,F\,c_\mathrm{max}, & \varphi \leq -\varphi_\mathrm{c} \end{cases} \tag{2.80}$$

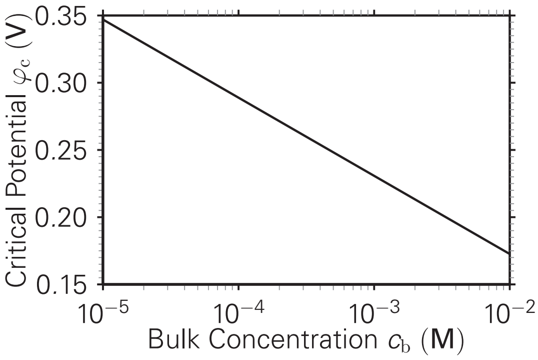

Figure 2.17: Bulk concentration dependence of the critical potential.

In the following, the thickness of and the electric potential within the inner crowding layer are determined. As boundary conditions for the electric potential the applied voltage $\varphi(r_1) = V$ and the critical potential $\varphi(r_c) = \varphi_c$ are used. Figure 2.17 shows the concentration dependence of φ_c. It can be seen that φ_c generally is small compared to typical values of V_0 (e.g. 5 V). In other words, for low frequencies, the major part of the voltage drop occurs over the crowding layer. Additionally, the continuity of the electric field at the interface r_c is required. The electric field in the outer domain, $r \geq r_c$, is given by

$$E(r) = \frac{\sqrt{2}\, 2\, k_B T}{e\, \lambda_D} \frac{\mathrm{sign}(\varphi)}{\sinh\left(\frac{\sqrt{2}\,(r - r_0)}{\lambda_D}\right)}, \tag{2.81}$$

which under the conditions $c_{max} \gg c_b$ and $V > \varphi_c$ determines the critical electric field

$$E_c = E(r_c) \approx \sqrt{\frac{2\, c_{max}}{c_b}} \frac{k_B T}{e\, \lambda_D} = \frac{k_B T}{2\, e\, \lambda_D^*}. \tag{2.82}$$

The term $\lambda_D^* = \sqrt{\frac{2\, c_b}{c_{max}}} \lambda_D = 0.2\,\mathrm{nm}$ is the Debye length corresponding to a solution with ion concentrations of c_{max} and 0, respectively. The associated critical electric field is $E_c = 2.53 \times 10^8\,\mathrm{V/m}$.

Solving the Poisson equation with the space charge density given by Equation 2.80, in the crowding region, $r \leq r_c$, there holds

$$E(r) = E_c - \frac{z\, F\, c_{max}}{\varepsilon} (r - r_c), \tag{2.83}$$

$$\varphi(r) = \varphi_c - \int_{r_c}^{r} \mathrm{d}r'\, E(r') = \varphi_c - E_c\,(r - r_c) + \frac{z\, F\, c_{max}}{2\,\varepsilon} (r - r_c)^2. \tag{2.84}$$

Applying the boundary condition $\varphi(r_1) = V$, the thickness of the crowding layer is given by

$$\delta = r_c - r_1 = \frac{\lambda_D^*}{z} \left[\sqrt{\frac{z\, e\,(V - \varphi_c)}{k_B T} + 1} - 1 \right] \tag{2.85}$$

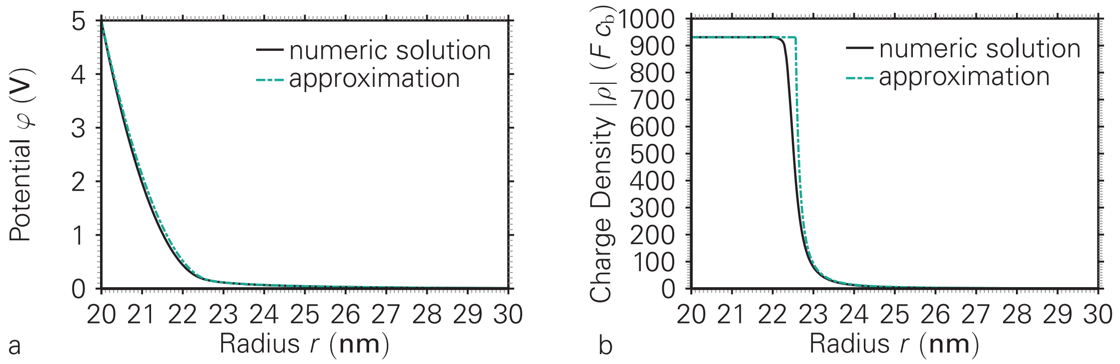

Figure 2.18: The numerical and the approximate, analytical solution of the electric potential (a) and charge density (b) for a spherical setup in the low-frequency regime agree well. The crowding layer thickness from the quasi-static approximation is $\delta = 2.6\,\text{nm}$. Parameters: $V_0 = 5\,\text{V}$, $r_1 = 20\,\text{nm}$, $f = 1\,\text{kHz}$, $c = 20\,\text{mM}$, $t = 0\,\mathcal{T}$.

and the electric field at the inner electrode by

$$E(r_1) = E_\mathrm{c}\sqrt{\frac{z\,e\,(V-\varphi_\mathrm{c})}{k_\mathrm{B}\,T}+1}. \tag{2.86}$$

Figure 2.18 compares the numerical solution of the electric potential and the charge density to their respective analytic, low-frequency relations. The composited charge density is steady but not smooth, unlike the numerical solution. Despite the fact that the crowding layer thickness δ is only one order of magnitude smaller than r_1, the planar approximation employed in the derivation of the low-frequency regime holds very well.

To determine the lower transition frequency, below which the quasi-static regime is observed, the voltage drop across the double layer is reviewed. The space charge density profile has a negligible frequency sensitivity below the lower transition frequency. In addition, the voltage drop across the double layer is proportional to the field screening (compare Equation 2.55 on page 32). Thus, a characteristic screening length λ is defined, such that

$$V_\mathrm{d} = \lambda(\omega)\left[E(r_1) - \frac{\imath\,\omega}{\imath\,\omega+\omega_\mathrm{T2}}\,E(r_1)\right] = \lambda(\omega)\frac{\omega_\mathrm{T2}}{\imath\,\omega+\omega_\mathrm{T2}}E(r_1). \tag{2.87}$$

From Equations 2.55 and 2.66 results

$$V - V_\mathrm{d} = \frac{r_1^d\,h_d(r_2)}{\lambda(\omega)}\frac{\imath\,\omega}{\omega_\mathrm{T2}}\,V_\mathrm{d}, \tag{2.88}$$

which with the abbreviation $\omega_\mathrm{T} = \omega_\mathrm{T2}\,\lambda(\omega)/r_1^d\,h_d(r_2)$ yields the frequency dependence of the electric variables

$$V_\mathrm{d}(\omega) = \frac{\omega_\mathrm{T}}{\imath\,\omega+\omega_\mathrm{T}}\,V, \tag{2.89a}$$

$$E(r_1,\omega) = \frac{V}{r_1^d\,h_d(r_2)}\,\frac{\imath\,\omega+\omega_\mathrm{T2}}{\imath\,\omega+\omega_\mathrm{T}}, \tag{2.89b}$$

$$E(r,\omega) = \frac{V}{r^d\,h_d(r_2)}\frac{\imath\,\omega}{\imath\,\omega+\omega_\mathrm{T}}, \quad r_\mathrm{b1} < r < r_\mathrm{b2}. \tag{2.89c}$$

The low-frequency limit of the parameter ω_T is the desired lower transition frequency. Hence, from the quasi-static limit of the screening length

$$\lim_{\omega \to 0} \lambda(\omega) = \lambda_\mathrm{D}^* \frac{e\,V}{2\,k_\mathrm{B}\,T} \left[\frac{z\,e\,(V - \varphi_\mathrm{c})}{k_\mathrm{B}\,T} + 1 \right]^{-1/2} \approx \sqrt{\frac{\varepsilon\,V}{2\,z\,F\,c_\mathrm{max}}}, \tag{2.90}$$

the lower transition frequency is obtained as

$$\omega_\mathrm{T1} = \frac{\omega_\mathrm{T2}}{r_1^d\,h_d(r_2)} \sqrt{\frac{\varepsilon\,V}{2\,z\,F\,c_\mathrm{max}}}. \tag{2.91}$$

The lower transition frequency ω_T1 shows a complex dependence on the simulation variables. Most notably, it increases with the square root of the applied voltage amplitude and is highly sensitive to the electrode geometry. The geometric factor involved, $r_1^d\,h_d(r_2)$, reduces for a spherical electrode to r_1, for a cylindrical electrode to $r_1\,\log(r_2/r_1)$, and for a plate capacitor to $r_2 - r_1$. This means that around nanoelectrodes like e.g. nanowires the lower transition frequency is several orders of magnitude larger than for planar electrodes with a gap size in the micrometer range. Additionally, ω_T1 and ω_T2 increase linearly with the bulk concentration.

Comparison of analytical and numerical frequency responses

The analytical findings for the frequency responses, Equation 2.89, contain the frequency-dependent parameter ω_T. With the simplification $\omega_\mathrm{T} \approx \omega_\mathrm{T1}$, a linear, effective system description is obtained. Generally, it agrees well with the numerical results shown in Figures 2.19 - 2.21. In the following, the parameter influence on the frequency response of the first harmonic's amplitude of the electric field at the nanowire tip and of the voltage drop across the dynamic double layer is discussed and interpreted with the help of the analytical expressions in Equation 2.89.

Voltage dependence, Figure 2.19 In the high-frequency range $\omega \gtrsim \omega_\mathrm{T2}$, the induced charge density has only a small amplitude. Consequently, the external electric field is the only relevant contribution to the electric field at the nanowire tip, and thus both are proportional to the applied AC voltage amplitude. For lower frequencies, the field screening becomes important. Consequently the total electric field in the bulk region (not shown) is diminished, whereas the electric field at the nanowire tip is increased due to the field enhancement. Far below the lower transition frequency $\omega \ll \omega_\mathrm{T1}$, the electric field at the nanowire tip approaches its quasi-static limit. The voltage range used in Figure 2.19 is significantly larger than the critical electric potential (cf. Figure 2.17) and thus, the low-frequency limit of the electric field at the tip is proportional to the square root of the voltage, $E(r_1) \propto \sqrt{V}$. The lower transition frequency itself is affected by the voltage, too, $\omega_\mathrm{T1} \propto \sqrt{V}$. In the proximity of the lower transition frequency $\omega \approx \omega_\mathrm{T1}$, due to the large screening fields, the frequency response is highly nonlinear. This explains, why in this frequency range the asymptotic low-frequency limit is approached uncommonly slowly.

The voltage drop across the double layer is negligible compared to the applied voltage for large frequencies $\omega \gtrsim \omega_{\mathrm{T2}}$, which is equivalent to the absence of a field screening. Under these circumstances, the voltage drop is proportional to the amount of accumulated charges in the double layer, both of which are proportional to the applied AC voltage. In the quasi-stationary, low-frequency regime $\omega \ll \omega_{\mathrm{T1}}$ the entire voltage drops over the double layer.

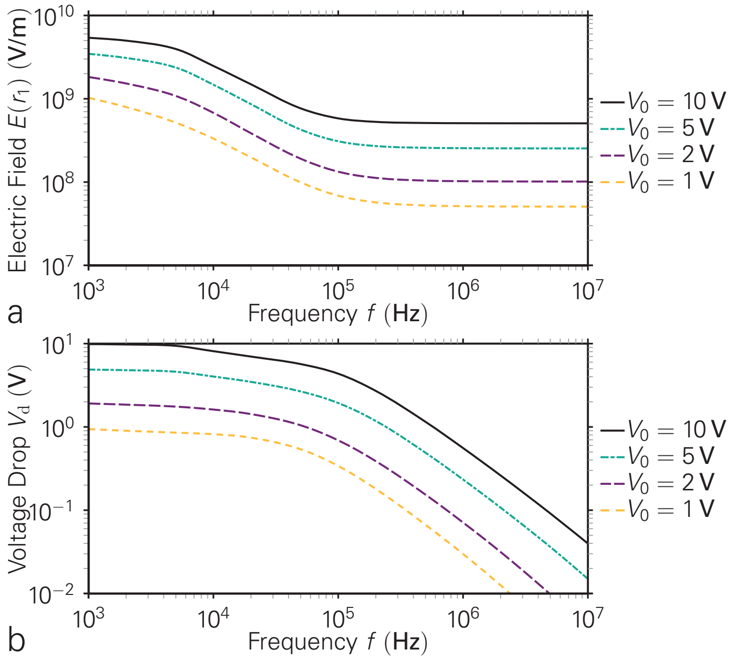

Figure 2.19: The figure shows the frequency dependence of the first Fourier component of the electric field at the electrode surface (a) and of the voltage drop across the double layer (b) with the amplitude of the external voltage as parameter. Parameters: $c_\mathrm{b} = 0.1$ mM, $r_1 = 20$ nm, $r_2 = 2$ µm. Resulting characteristic values at $V_0 = 5$ V: $\omega_{\mathrm{T1}}/(2\,\pi) = 5.3$ kHz, $\omega_{\mathrm{T2}}/(2\,\pi) = 74$ kHz, $\varphi_\mathrm{c} = 0.29$ V.

Concentration dependence, Figure 2.20 The lower and the upper transition frequency, ω_{T1} and ω_{T2}, are both proportional to the bulk ion concentration c_b. Additionally, the critical potential, which affects the low-frequency behavior, is in all considered cases much smaller than the applied AC voltage. Thus, by lowering the bulk concentration the entire frequency response of the electric field is shifted to the left on the log-scale frequency axis.

Analogous to the electric field observations, the voltage drop across the double layer follows roughly the trend of frequency shifts. However, for the ion concentration of 10 mM in Figure 2.20b, an additional nonlinear effect is visible near the frequency $f = 1$ MHz. This effect is presumably linked to the creation of higher-harmonics, which are not included in this plot.

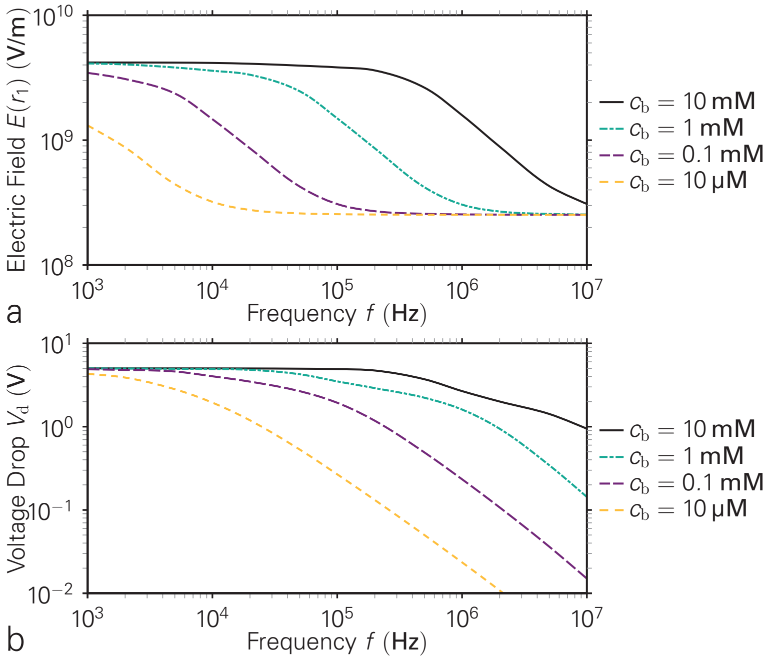

Figure 2.20: The figure shows the frequency dependence of the first Fourier component of the electric field at the electrode surface (a) and of the voltage drop across the double layer (b) with the bulk concentration as parameter. Parameters: $V_0 = 5\,\mathrm{V}$, $r_1 = 20\,\mathrm{nm}$, $r_2 = 2\,\mu\mathrm{m}$. The lower and upper transition frequency, ω_{T1} and ω_{T2}, are proportional to the bulk concentration. The critical potential φ_{c} changes between 0.18 V and 0.35 V.

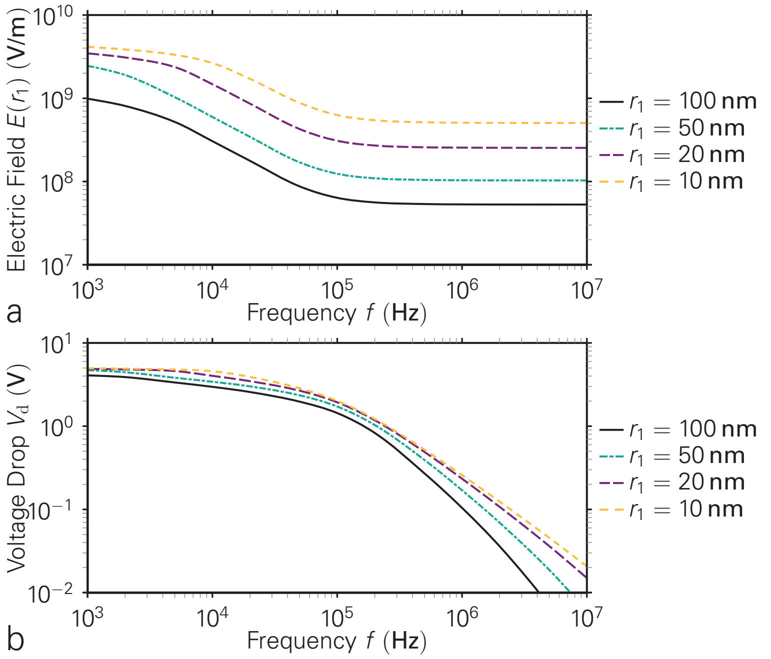

Figure 2.21: The figure shows the frequency dependence of the first Fourier component of the electric field at the electrode surface (a) and of the voltage drop across the double layer (b) with the tip radius as parameter. Parameters: $V_0 = 5\,\mathrm{V}$, $c_{\mathrm{b}} = 0.1\,\mathrm{mM}$, $r_2 = 2\,\mu\mathrm{m}$. Resulting characteristic values for $r_1 = 20\,\mathrm{nm}$: $\omega_{\mathrm{T1}}/(2\,\pi) = 5.3\,\mathrm{kHz}$, $\omega_{\mathrm{T2}}/(2\,\pi) = 74\,\mathrm{kHz}$, $\varphi_{\mathrm{c}} = 0.29\,\mathrm{V}$.

Tip size dependence, Figure 2.21 Since in the high-frequency range the total electric field at the nanowire tip equals the external electric field, it is inversely proportional to the electrode radius, $E(r_1) \propto r_1^{-1}$. However, in the quasi-static limit $\omega \ll \omega_{\mathrm{T1}}$, the double layer thickness is small compared to the electrode radius. Thus, for all electrode radii approximately the same charge profile forms at the electrode. Therefore, the low-frequency limit of the total electric field at the nanowire tip is the same in all cases. However, since the lower transition frequency is inversely proportional to the electrode radius as well $\omega_{\mathrm{T1}} \propto r_1^{-1}$, the low-frequency limit for the larger electrode radius $r_1 \geq 50\,\mathrm{nm}$ is outside the considered frequency interval.

The voltage drop across the double layer does not show a significant dependence on the electrode radius, which is confirmed by Equation 2.89a.

Frequency-influence on the spatiotemporal evolution of the charge density

The frequency dependence of the spatiotemporal behavior of the charge density is shown in Figure 2.22. Due to the time symmetry property of the ion concentration (Equation 2.46) for the charge density holds

$$\rho(r,t) = -\rho(r,t+\mathcal{T}/2). \tag{2.92}$$

The low-frequency case $\omega < \omega_{\mathrm{T1}}$ in panel (a) exhibits a compressed charge density profile with a large amplitude. The major fraction of the accumulated charge is in the crowding layer close to the electrode ($r < 22\,\mathrm{nm}$). Although the applied AC frequency is about a factor of 5 below the lower transition frequency, the corresponding charge density profile is not (yet) quasi-static. If it was, the additional symmetry relation $\rho(r,t) = -\rho(r,\mathcal{T}/2 - t)$ would hold. The reason is that in the limit of large ion concentrations the PNP equations are highly nonlinear, which creates higher harmonics of the charge density with a multiple of the applied AC frequency. These higher harmonics exceed the lower transition frequency.

For the intermediate frequency $\omega_{\mathrm{T1}} < \omega < \omega_{\mathrm{T2}}$ in panel (b), the charge density exhibits a particularly long-ranged pattern. Close to the peak voltage, i.e. at $t = 0.25\mathcal{T}$ and $t = 0.75\mathcal{T}$ respectively, a thin crowding layer forms, which contains the majority of the charge. At the times of polarity reversal ($t = 0\mathcal{T}$ and $t = 0.5\mathcal{T}$) the electric field is relatively small. Then, the large amount of accumulated ions is released and spread mostly by diffusion to far distances.

In panel (c) a frequency slightly above ω_{T2} is shown. The charge accumulation zone is even thinner than before and thus below the image resolution. At this frequency, the onset of the electric field after the polarity reversal is faster than in (b). Therefore, the broadening of the ion accumulation peak is accompanied by an active repulsion of the ions by the electric field. Characteristically for this frequency range, the charge density has a local extremum in the radial direction right after the polarity reversal, see also Figure 2.14. By the collective migration of the ions that form the concentration peak, the

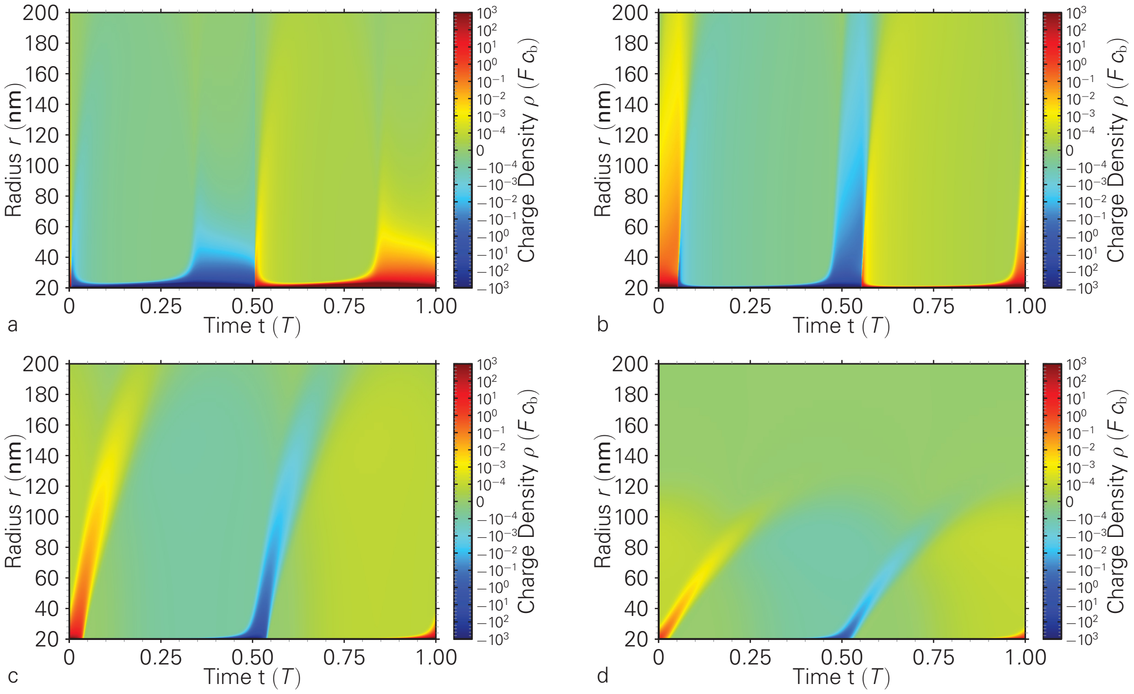

Figure 2.22: Spatiotemporal behavior of the charge density $\rho(r, t)$ at frequencies 1, 10, 100, and 1000 kHz (a - d). The time scale refers to the applied voltage $V(t) = V_0 \sin(2\,\pi\, t/T)$. Parameters: $V_0 = 5\,\mathrm{V}$, $c_\mathrm{b} = 0.1\,\mathrm{mM}$, $r_1 = 20\,\mathrm{nm}$, $r_2 = 2\,\mu\mathrm{m}$. Resulting characteristic values: $\omega_{\mathrm{T1}}/2\pi = 5.3\,\mathrm{kHz}$, $\omega_{\mathrm{T2}}/2\pi = 74\,\mathrm{kHz}$, $\varphi_\mathrm{c} = 0.29\,\mathrm{V}$. Color bars are cut to $\pm 10^3\, F\, c_\mathrm{b}$.

peak maximum travels radially over time, which results in charge repulsion patterns that are slightly tilted in the r–t plane.

The high-frequency case $\omega_{\mathrm{T2}} \ll \omega$ in panel (d) is qualitatively similar to panel (c). Due to the high frequency, the overall ion accumulation is much lower and therefore the charge density fluctuations have an even shorter range. In comparison to (c) the migrative tilt is even more emphasized. However, this is only an apparent effect owing to a shorter period time; the ion velocity associated to the slope is approximately the same for both cases.

2.6 AC ELECTRO-OSMOTIC FLUID FLOW

As discussed in section 2.4, the contradiction between theory and experiments regarding the velocity of nanowire growth from neutral particles can presumably be resolved by including AC electro-osmotic (ACEO) fluid flows into the model. For calculating the AC electro-osmotic flow, the slip approximation has often been applied, i.e. the Stokes equation without the body-force term is solved with the slip velocity at the electrodes as boundary condition for the fluid velocity [48, 56]. Hereby, the slip velocity is derived within the thin double layer approximation by solving the PNP equations while neglecting any feedback of electro-osmotic fluid flow on the double layer. In view of the complex spatiotemporal behavior of the charge density presented in this work (Figure 2.22), the electro-osmotic fluid flow should be derived by fully taking into account the spatiotemporal dependence of the body force. The necessary equations to model the ACEO fluid flow have already been presented in the previous sections and are repeated here for clarity. In detail these are: the modified PNP equations to model the electrical and chemical potential

$$\frac{\partial}{\partial t} c_i = -\nabla \cdot \mathbf{j}_i, \tag{2.93a}$$

$$\mathbf{j}_i = -\frac{D_i}{k_\mathrm{B} T} c_i \nabla(\mu_i + z_i e \varphi) + c_i \mathbf{v}, \tag{2.93b}$$

$$\nabla^2 \varphi = -\frac{z F}{\varepsilon}(c_1 - c_2), \tag{2.93c}$$

the incompressible Navier–Stokes equation

$$\rho_\mathrm{m} \left(\frac{\partial \mathbf{v}}{\partial t} + (\mathbf{v} \cdot \nabla) \mathbf{v} \right) = -\nabla p + \eta \Delta \mathbf{v} + \mathbf{f} \tag{2.94a}$$

with the additional constraint $\nabla \cdot \mathbf{v} = 0$ and the body force given by

$$\mathbf{f} = z F (c_1 - c_2) \mathbf{E}, \tag{2.94b}$$

and finally the continuity and transport equation for the neutral particles that involves diffusion, migration, and convection

$$\frac{\partial}{\partial t} c = -\nabla \cdot \mathbf{j}, \tag{2.95a}$$

$$\mathbf{j} = -D \nabla c + \frac{D \alpha}{2 k_\mathrm{B} T} c \nabla (\nabla \varphi)^2 + c \mathbf{v}. \tag{2.95b}$$

The boundary conditions were chosen for the nanowire electrode as

$$\mathbf{n} \cdot \mathbf{j}_i = 0, \quad \varphi(t) = V_0 \sin(\omega t), \quad \mathbf{v} = \mathbf{0}, \quad c = 0, \tag{2.96a}$$

for the opposing counter electrode as

$$\mathbf{n} \cdot \mathbf{j}_i = 0, \quad \varphi(t) = 0, \quad \mathbf{v} = \mathbf{0}, \quad c = c_0, \tag{2.96b}$$

and on all other system boundaries (simulation cell cut-off) as

$$\mathbf{n} \cdot \mathbf{j}_i = 0, \quad \mathbf{n} \cdot \mathbf{E} = 0, \quad \mathbf{v} = \mathbf{0}, \quad \mathbf{n} \cdot \mathbf{j} = 0. \tag{2.96c}$$

The simultaneous solution of all equations is a numerically demanding and computationally very expensive task. To this end, it is essential to simplify the model. As vantage ground, the three contributions to the particle flux (Equation 2.95) are considered. In the limit of large frequencies ($\omega \gtrsim \omega_\mathrm{T2}$) the electric field approaches the external electric field as shown in section 2.5.3. Under these conditions the migrative particle velocity can be estimated by $z_i D_i e \mathbf{E}_\mathrm{ext}/(k_\mathrm{B} T)$. For the parameters as used in section 2.5.3 the typical migrative particle velocity is in the order of 1 m/s. Thus, for fluid velocities much slower than the migrative particle velocities, the convection plays only a minor role for the ion dynamics. Therefore, to simplify the ACEO simulation, the convective contribution to

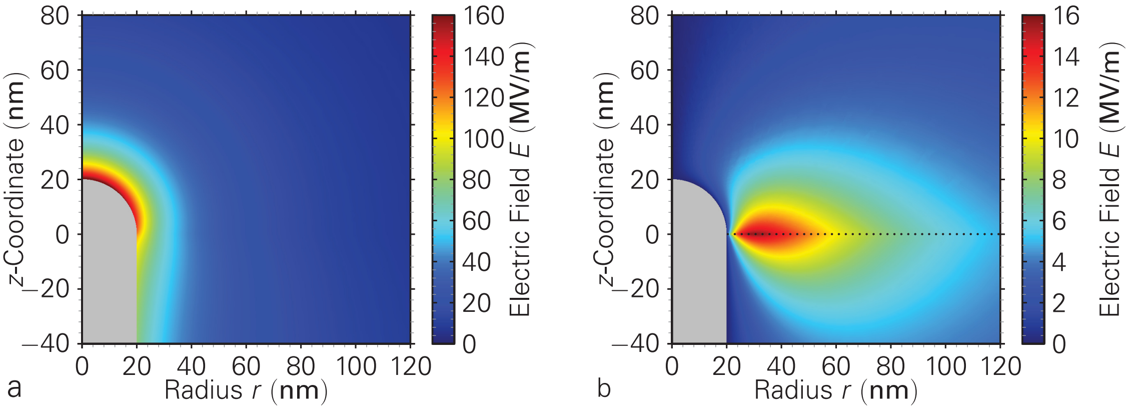

Figure 2.23: Normal (a) and tangential (b) electric field components near the nanowire tip for an applied voltage of $V_0 = 5\,\mathrm{V}$. The dotted line in (b) marks the contact plane $z = 0$ between spherical and cylindrical coordinate systems.

the *ion flux* (Equation 2.93b) is neglected. Moreover, it has been shown in section 2.3.2 that dielectrophoretic fluid flows are negligible as well. From these two prerequisites immediately follows that the PDE system decouples and can be solved sequentially. The solution of the PNP equations is the first step and was described in the previous section. In the second step, the body force of the Navier–Stokes equation is computed from the charge density and the electric field. In the final step, the fluid velocity obtained from the solution of the Navier–Stokes equation enters the transport equation for neutral particles (Equation 2.95), which determines the nanowire growth velocity.

Despite the well-justified model simplifications introduced so far, the computational complexity of the ion transport model is still very high so that each simulation run takes almost two weeks of computation time. A much faster, albeit rather crude estimate can be obtained from the one-dimensional ion dynamics simulations presented in section 2.5.2. The accuracy of the simulation results is determined by a comparison among the two simplification levels for the nanowire geometry.

2.6.1 ACEO fluid flow estimation based on one-dimensional solutions of the PNP equations

Within any one-dimensional geometry (cf. Figure 2.6a on page 15) the body force is balanced by the pressure gradient and, consequently, no fluid flow evolves. Therefore, the axially symmetric nanowire geometry as shown in Figure 2.6b on page 15 is used for the fluid flow calculations. The union of the hemispherical nanowire tip with the cylindrical wire breaks the one-dimensional symmetry of its components in the contact zone. This symmetry change in the contact plane gives rise to comparatively large electric field components tangential to the nanowire surface, cf. Figure 2.23. The normal field component is defined as the radial component in the respective cylindrical and spherical coordinate systems. The tangential component, which is crucial for the AC electro-osmotic fluid flow, is the corresponding orthogonal component, i.e. E_z and E_θ, respectively.

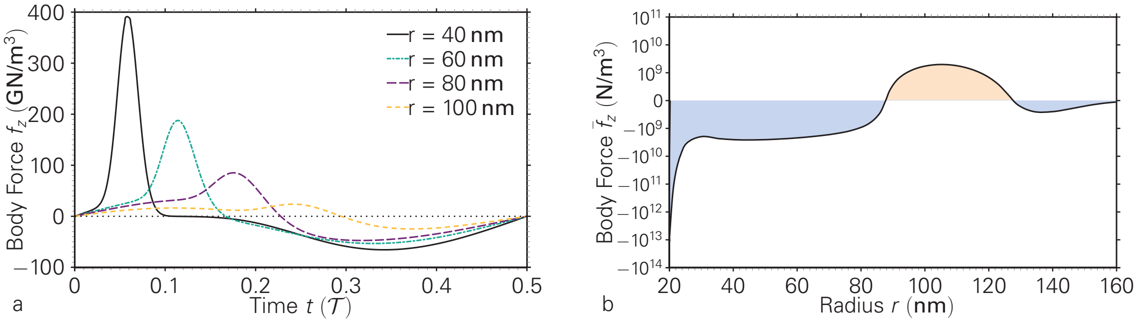

Figure 2.24: (a) The time-evolution of the z-component of the body force at various radii in the plane $z = 0$ reveals two changes of sign within one half oscillation period. (b) The time-averaged z-component of the body force $\bar{f}_z(r)$ as a function of the radius exhibits two sign changes, e.g. at $r \approx 90$ nm and $r \approx 125$ nm. The amplitude of the body force is substantially smaller than its time average. Parameters: $V = 5$ V, $f = 1$ MHz, $c_\mathrm{b} = 0.1$ mM.

Because of the dominant normal field component and its moderate change along the surface of the hemispherical cap (Figure 2.23a), it can be expected that the radial dependence of the charge density does not change dramatically near the transition region. Thus, to estimate the body force, the charge density calculated above for the mere spherical-symmetric case is also used within the transition region close to the contact plane $z = 0$ as highlighted in Figure 2.23b. From the charge density in the spherical geometry $\tilde{\rho}(r, t)$ the charge density in the cylinder coordinate system is constructed as

$$\rho(r, z, t) = \begin{cases} \tilde{\rho}(\sqrt{r^2 + z^2}, t) & , z \geq 0 \\ \tilde{\rho}(r, t) & , z < 0 \end{cases} . \tag{2.97}$$

This may seem like a crude approximation, which greatly overestimates the charge density in the region $z \ll 0$. However, in view of the small extension of the tangential electric field in z-direction (cf. Figure 2.23), this approximation should yield a tentative picture of the fluid flow and an estimate of the order of magnitude of the flow velocity. For an illustration of the spatiotemporal behavior of the body force, at first the body force within the contact plane $z = 0$ is considered. There, the tangential component of the body force is parallel to the axial z-direction

$$f_\mathrm{z}(r, t) = \rho(r, t)\, E_\mathrm{z}(r, t). \tag{2.98}$$

The tangential electric field component in Equation 2.98 is actually affected by the induced charge density. However, when considering large frequencies $\omega \gtrsim \omega_{\mathrm{T2}}$, this effect is small, as shown in section 2.5.3. Then, the electric field is almost equal to the external field, and thus in phase with the applied voltage (Equation 2.89), but not so with the space charge density (Figure 2.22). Consequently, the space charge density and electric field in Equation 2.98 exhibit different signs during certain time intervals. In other words, the sign of the body force changes periodically over time. Figure 2.24a shows the z-component of the body force within the plane $z = 0$ as a function of time at different radial distances for a frequency of 1 MHz. All curves exhibit two zero crossings within one half oscillation period. In Figure 2.24b, the radial dependence of the z-component of the time-averaged body force is shown. Remarkably, this curve reveals several changes in sign of the body force over the radius. The radial body force dependence (Figure 2.24b) suggests that the fluid flow near the nanowire is directed opposite to the wire growth direction, and a back-flow occurs at distances beyond 90 nm.

The ACEO fluid flow, which results from the body force as discussed, is characterized by the Reynolds number. To estimate the Reynolds number, a characteristic system length, ℓ, in the order of 100 nm is extracted from the charge density calculations. From preparatory fluid flow simulations, fluid velocities of $v \lesssim 10^{-3}\,\mathrm{m/s}$ are expected. Therefore, for the present flow problem the estimated Reynolds number $Re = \rho_\mathrm{m}\, v\, \hat{\ell}/\eta \lesssim 10^{-4}$ is small. Hence, the nonlinear terms in the Navier–Stokes equation (Equation 2.95) can be neglected, as before in section 2.4. The remaining equation system is linear in $\mathbf{v}$ and p, and a Fourier transformation of it yields

$$\imath\, \omega\, \rho_\mathrm{m}\, \mathbf{v}(\omega) = -\nabla p(\omega) + \eta\, \Delta \mathbf{v}(\omega) + \mathbf{f}(\omega), \tag{2.99a}$$

$$\nabla \cdot \mathbf{v}(\omega) = 0. \tag{2.99b}$$

This form reveals that each Fourier mode of $\mathbf{v}$ and p only depends on the corresponding Fourier mode of $\mathbf{f}$. Due to the time symmetry property of the ion concentrations, Equation 2.46 on page 29, the Fourier spectra of the charge density ρ and the electric field $\mathbf{E}$ contain only odd components. Thus their product, the body force $\mathbf{f}$, and therefore also the fluid velocity $\mathbf{v}$ and the pressure p exhibit only even Fourier components. The Fourier transformed Navier–Stokes equation, Equation 2.99 is solved numerically for each Fourier component of $\mathbf{v}$ and p separately. Since the pressure in the liquid only occurs in the Navier–Stokes equation, it is merely a byproduct of the fluid flow computation and therefore not studied in more detail. Along the electrode surfaces and on the edges of the simulation cell ($0 \le r \le 3\,\mu\mathrm{m}$, $-0.85\,\mu\mathrm{m} \le z \le 2.15\,\mu\mathrm{m}$), a velocity of zero was used as boundary condition (no-slip boundary condition). The rotational axis $r = 0$ marks an exception, as this is not a system boundary.

All resulting Fourier components of $\mathbf{v}$, with the exception of $\omega = 0$, are complex valued vectors, i.e. the fluid flow at each point of space is described by four real scalars for each Fourier mode. Since the higher Fourier modes always occur in complex conjugate pairs, the real sum of both is considered. For one point of space the time-dependence of the sum of one Fourier mode pair of $\mathbf{v}$ is given by

$$\mathbf{v}(t) = 2 \begin{bmatrix} \mathfrak{Re}(v_r) & \mathfrak{Im}(v_r) \\ \mathfrak{Re}(v_z) & \mathfrak{Im}(v_z) \end{bmatrix} \cdot \begin{bmatrix} \cos(\omega t) \\ -\sin(\omega t) \end{bmatrix}, \tag{2.100}$$

which is shown in Figure 2.25. Over one oscillation period, the end points of the fluid flow vectors describe an ellipse. To simplify the visualization of the higher Fourier components of the fluid velocity, only the semi-major axis of this ellipse is pictured. This construction ensures that the maximum occurring velocity of this Fourier component and its direction are rendered.

The calculated velocity field of the fluid flow near the nanowire tip is shown in Figure 2.26. Accordingly, the time-averaged body force drives the fluid from the nanowire tip along

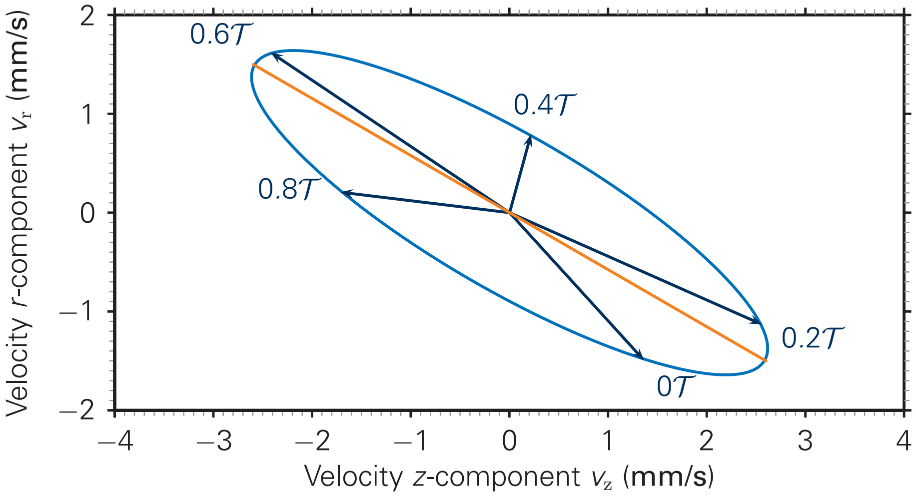

Figure 2.25: Illustration of a higher Fourier mode of the fluid flow velocity in the time-domain at one point of space. Generally, the end points of these velocity vectors describe an ellipse. For visualization purpose the highlighted semi-major axis is used, which is simultaneously the largest principal value of the velocity.

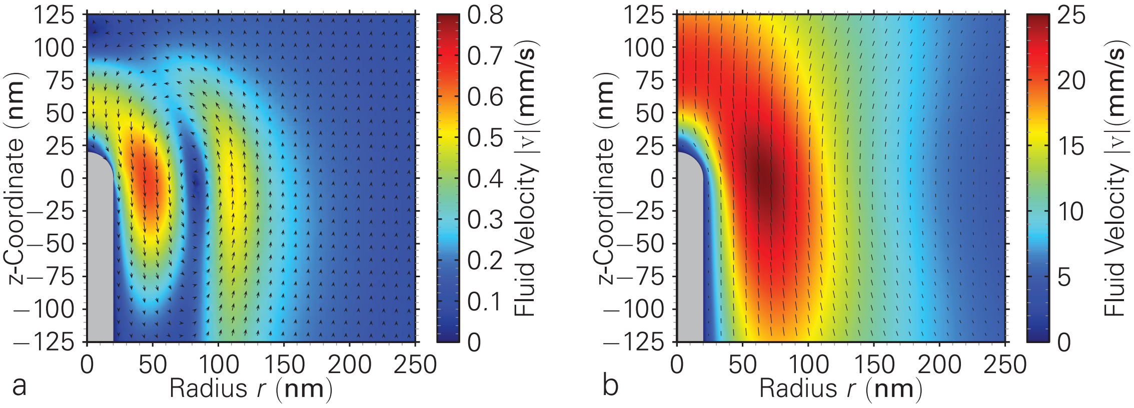

Figure 2.26: Magnitude and direction of the calculated velocity field of the fluid flow near the nanowire tip. Panel (a) shows the time-averaged fluid flow ($\omega = 0$), panel (b) shows the largest principal value of the $\omega = 4\pi f$ component of the fluid velocity (cf. Figure 2.25). Parameters: $f = 1$ MHz, $c_b = 0.1$ mM, $V_0 = 5$ V, $r_1 = 20$ nm.

the nanowire surface in negative z-direction within a cylindrical shell of about 50 nm thickness. The main back-flow occurs in a cylindrical shell with inner radius of about 100 nm and outer radius of 150 nm. The magnitude of the estimated velocity reaches values of up to 0.6 mm/s. A qualitatively similar flow pattern was reported by Yeo et al. [60] for a wire geometry on the microscale using a slip boundary condition. The overall fluid flow is the superposition of the time-average flow pattern and higher-order fluid flow oscillations at even multiples of the base frequency. Figure 2.26b shows the oscillation pattern of the Fourier mode with the lowest frequency ($\omega = 4\pi f$). Although the fluid flow velocity amplitude is larger than the time-average flow velocity, the oscillation amplitude associated to this mode is less than 2 nm.

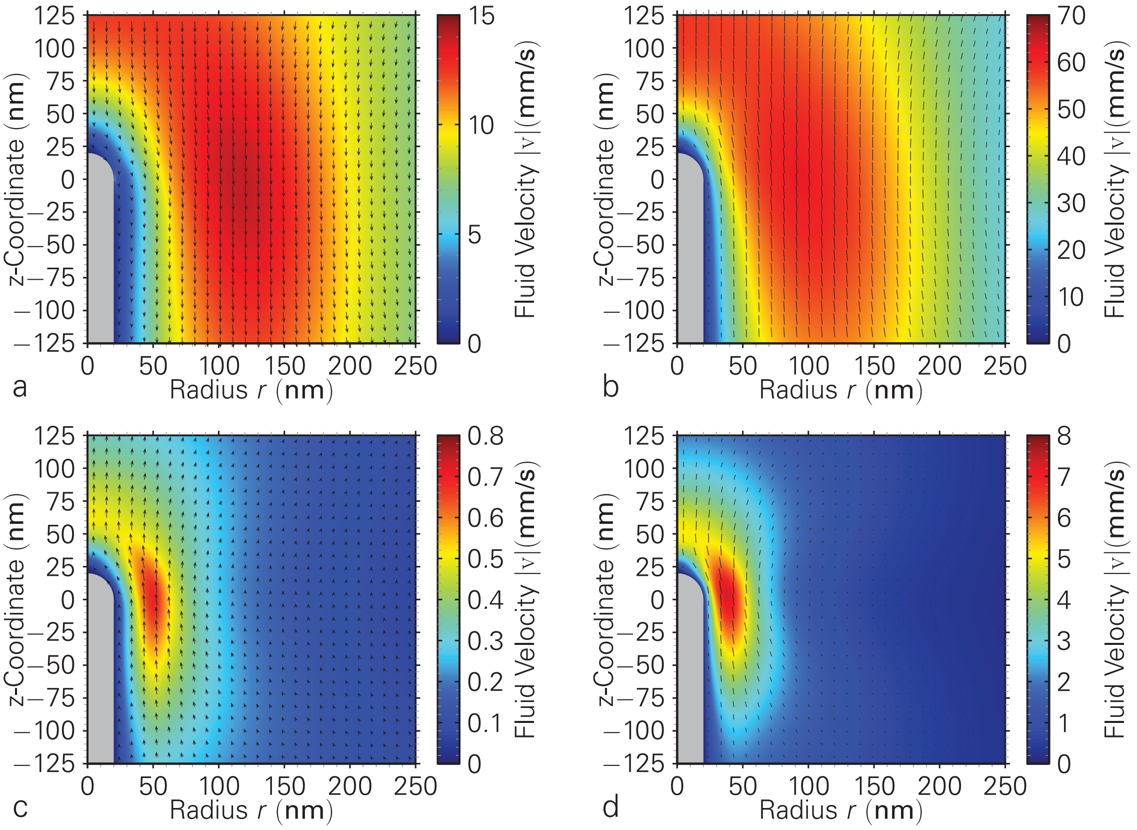

Figure 2.27: Magnitude and direction of the calculated velocity field of the fluid flow near the nanowire tip. Panel (a) and (c) show the time-average fluid flow ($\omega = 0$) for $f =$ 100 kHz and $f = 10$ MHz, respectively. Panel (b) and (d) show the largest principal value of the $\omega = 4\pi f$ mode of the fluid velocity for $f = 100$ kHz and $f = 10$ MHz, respectively. Parameters: $c_\mathrm{b} = 0.1$ mM, $V_0 = 5$ V, $r_1 = 20$ nm.

In Figure 2.27 the flow patterns for a higher frequency (10 MHz) and a lower frequency (100 kHz) are compared. Here, the results for 100 kHz bear a more qualitative character, since the prerequisite of negligible induced electric field is impaired. The simulations show that above the upper transition frequency ω_{T2}, the spatial extension of the fluid flow pattern decreases with increasing frequency. This is caused by the reduction of the amplitude and pattern range of the charge density as discussed in section 2.5.3. Additionally, there is a transition in the direction of fluid flow at the nanowire tip from antiparallel to the direction of growth for low frequencies to parallel to the direction of growth for higher frequencies. The previously shown case of an intermediate frequency (Figure 2.26) exhibits a localized toroidal roll cell with a radius of about 80 nm. Apparently, this pattern marks an intermediate transition state between the high- and low-frequency pattern. The amplitude of the fluid velocity generally decreases with the applied frequency, but due to the flow pattern transition, there is a local minimum around 1 MHz. As before, the amplitude of the Fourier component with $\omega = 4\,\pi\, f$ is much larger than the time-average. Furthermore, the extension and the amplitude of the flow pattern decrease with increasing frequency.

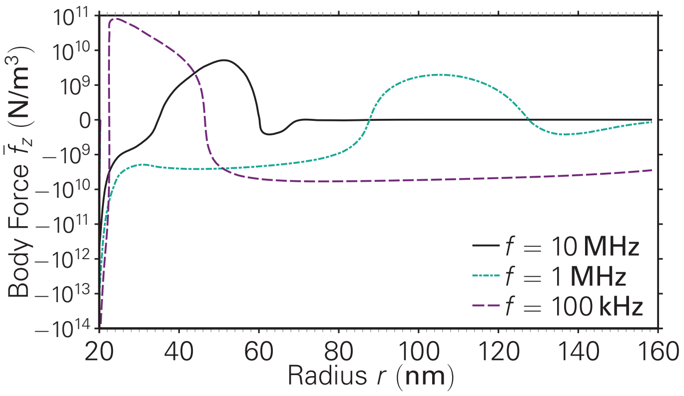

Figure 2.28: Radial dependence of the time-averaged tangential body force at the contact plane $z = 0$ for three different AC frequencies.

The key to understanding the transition of the flow pattern lies in the spatial and temporal dependence of the tangential body force. To illustrate this, Figure 2.28 compares the time-averaged tangential body forces at the three investigated frequencies. In general, the time-averaged body force curves lack a coherent trend for the AC frequency. This emphasizes the highly nonlinear character of the body force, which causes the unexpected flow pattern. Notably, the time-average of the body force is much smaller than its oscillation amplitude for all frequencies, see e.g. Figure 2.24. The consequence of an almost vanishing body force time-average is that the higher-harmonic fluid velocity amplitudes are much larger by comparison.

The quantitative influence of the frequency on the fluid flow is given by an analytical relation: since the Navier–Stokes equation is in its linear limit, the velocity amplitude is proportional to the body force amplitude, which in turn depends on ρ and $\mathbf{E}$. According to Equation 2.60 and Equation 2.89, at a given frequency $\omega > \omega_{\mathrm{T1}}$ both the charge density and the electric field depend linearly on the applied voltage. On the other hand, since the induced electric field is negligible at the considered frequencies, the electric field is independent from the bulk concentration, whereas the charge density depends linearly on it. In summary, this means that the fluid flow oscillation amplitude is proportional to $V_0^2 c_{\mathrm{b}}$.

2.6.2 ACEO fluid flow simulation based on solutions of the PNP for an axially symmetric nanowire geometry

In this section, a more precise solution of the ACEO model (see page 46) is presented. As before, the PNP equations, the Navier–Stokes equation, and the transport of neutral particles are solved sequentially. However, in contrast to section 2.6.1, the PNP equations (Equation 2.93) are calculated on the entire wire geometry and not estimated from the one-dimensional simulations. The time spent on these extended simulations is typically a factor of ten larger than the simplified versions of section 2.6.1.

The Figures 2.29, 2.30 and 2.31 show the obtained charge densities for the previously considered frequencies of 100 kHz, 1 MHz and 10 MHz, respectively. In their panels (a)–(d), the asymptotic periodic charge densities in the vicinity of the nanowire are displayed for various times. Additionally, in panels (e) and (f) the charge densities along the axial ($r = 0$) and radial ($z = 0$) direction of nanowire tip are depicted as a function of time. As it turns out, for all three discussed frequencies, the charge density differences between these two directions are only minor and occur mainly for larger radii ($r \geq 100\,\mathrm{nm}$). Furthermore, these cuts agree well with their one-dimensional pendants in Figure 2.22 on page 45. Consequently, for $f \geq 100\,\mathrm{kHz}$ the assumptions of section 2.6.1, to employ the one-dimensional simulation results in the tip region, are confirmed.

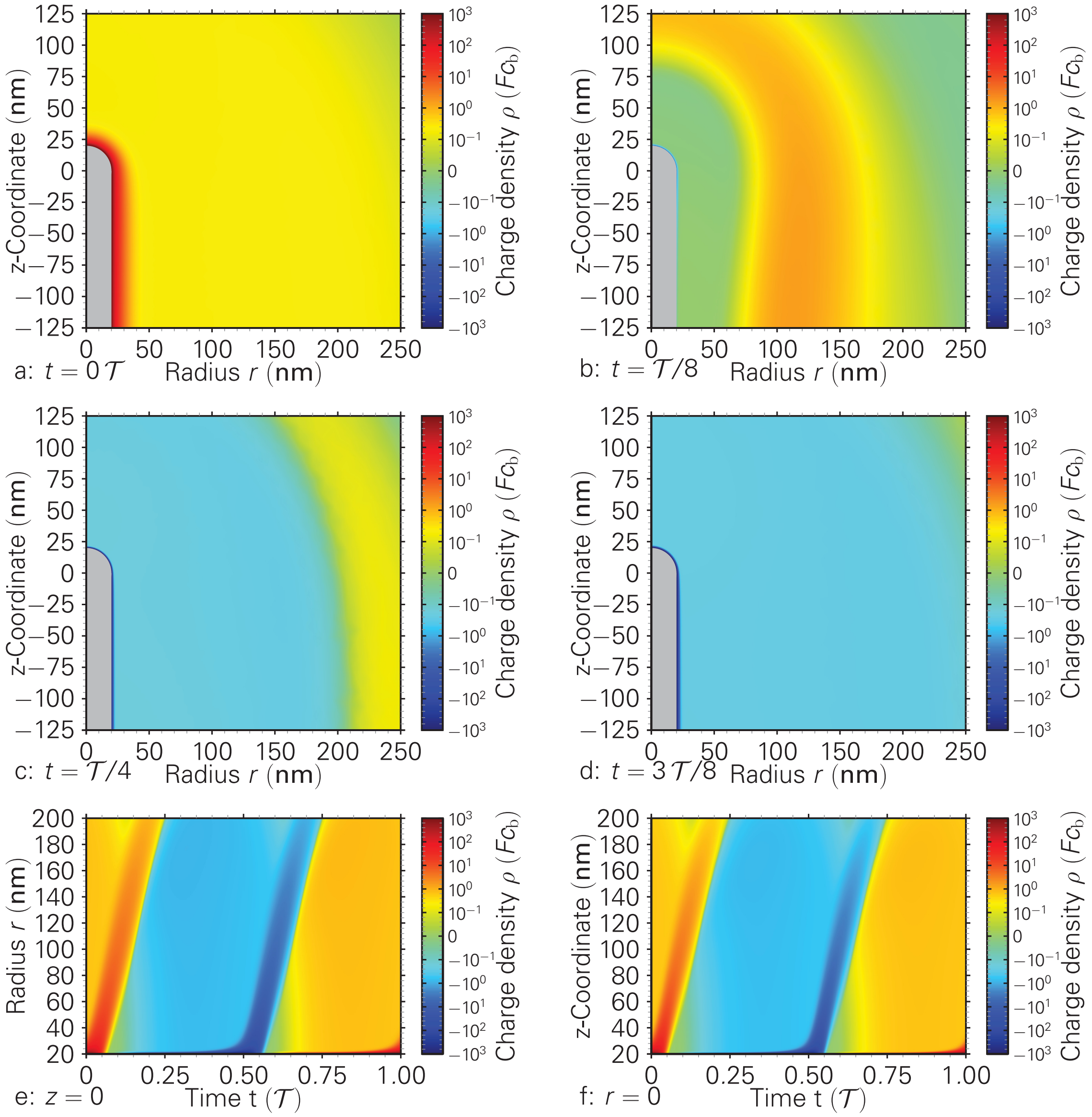
a: $t = 0\,\mathcal{T}$

b: $t = \mathcal{T}/8$

c: $t = \mathcal{T}/4$

d: $t = 3\,\mathcal{T}/8$

e: $z = 0$

f: $r = 0$

Figure 2.29: Spatio-temporal evolution of the charge density resulting from the two-dimensional solution of the PNP equations. Panels (a)-(d) show the charge density for the times $0\,\mathcal{T}$, $0.125\,\mathcal{T}$, $0.25\,\mathcal{T}$ and $0.375\,\mathcal{T}$. A radial (e) and axial (f) cut through the simulation domain illustrates the time dependence. Parameters: $f = 100\,\mathrm{kHz}$, $c_\mathrm{b} = 0.1\,\mathrm{mM}$, $V_0 = 5\,\mathrm{V}$, $r_1 = 20\,\mathrm{nm}$.

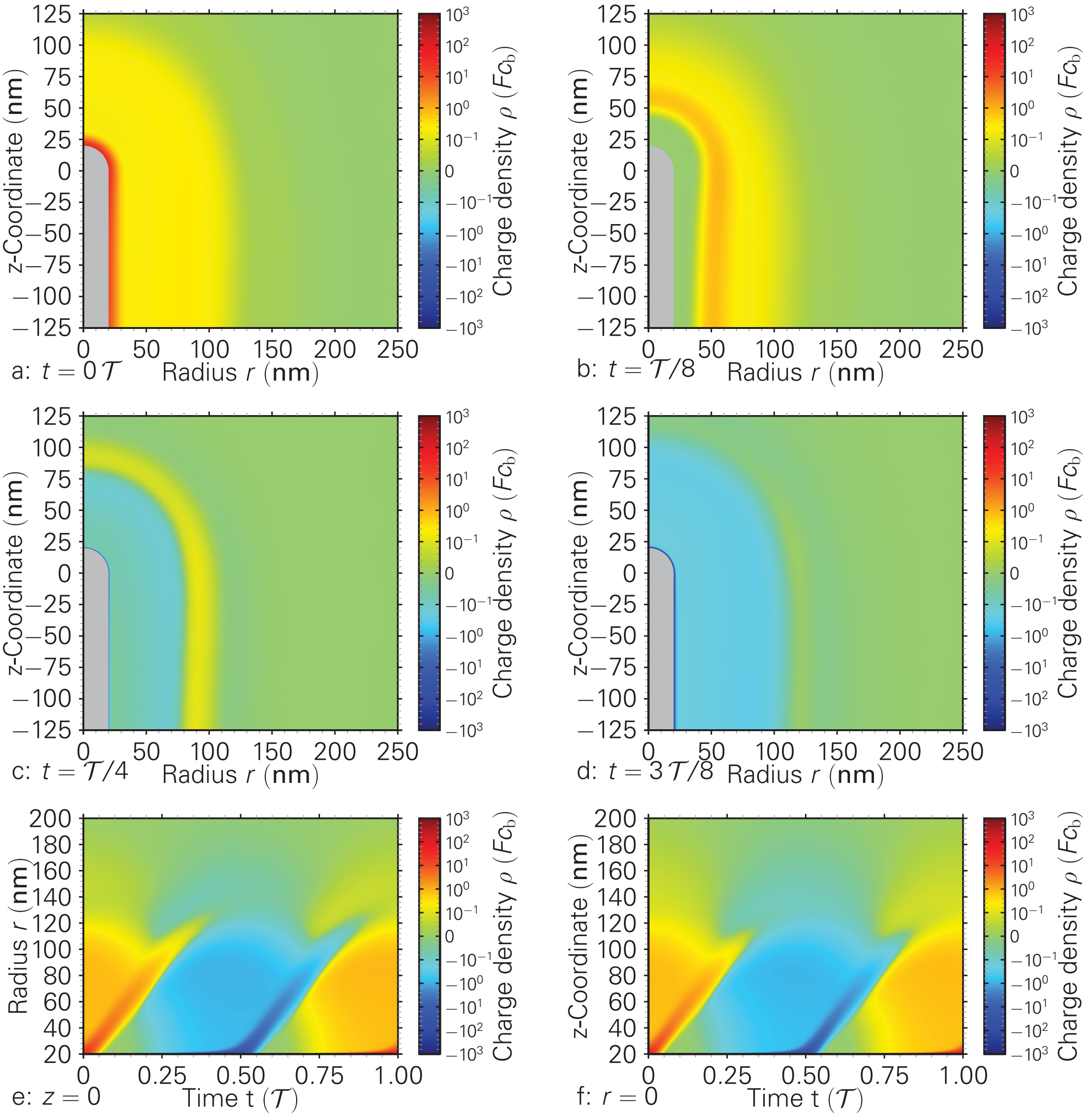
a: $t = 0\,\mathcal{T}$

b: $t = \mathcal{T}/8$

c: $t = \mathcal{T}/4$

d: $t = 3\mathcal{T}/8$

e: $z = 0$

f: $r = 0$

Figure 2.30: Spatio-temporal evolution of the charge density resulting from the two-dimensional solution of the PNP equations. Panels (a)-(d) show the charge density for the times $0\,\mathcal{T}$, $0.125\,\mathcal{T}$, $0.25\,\mathcal{T}$ and $0.375\,\mathcal{T}$. A radial (e) and axial (f) cut through the simulation domain illustrates the time dependence. Parameters: $f = 1\,\text{MHz}$, $c_\text{b} = 0.1\,\text{mM}$, $V_0 = 5\,\text{V}$, $r_1 = 20\,\text{nm}$.

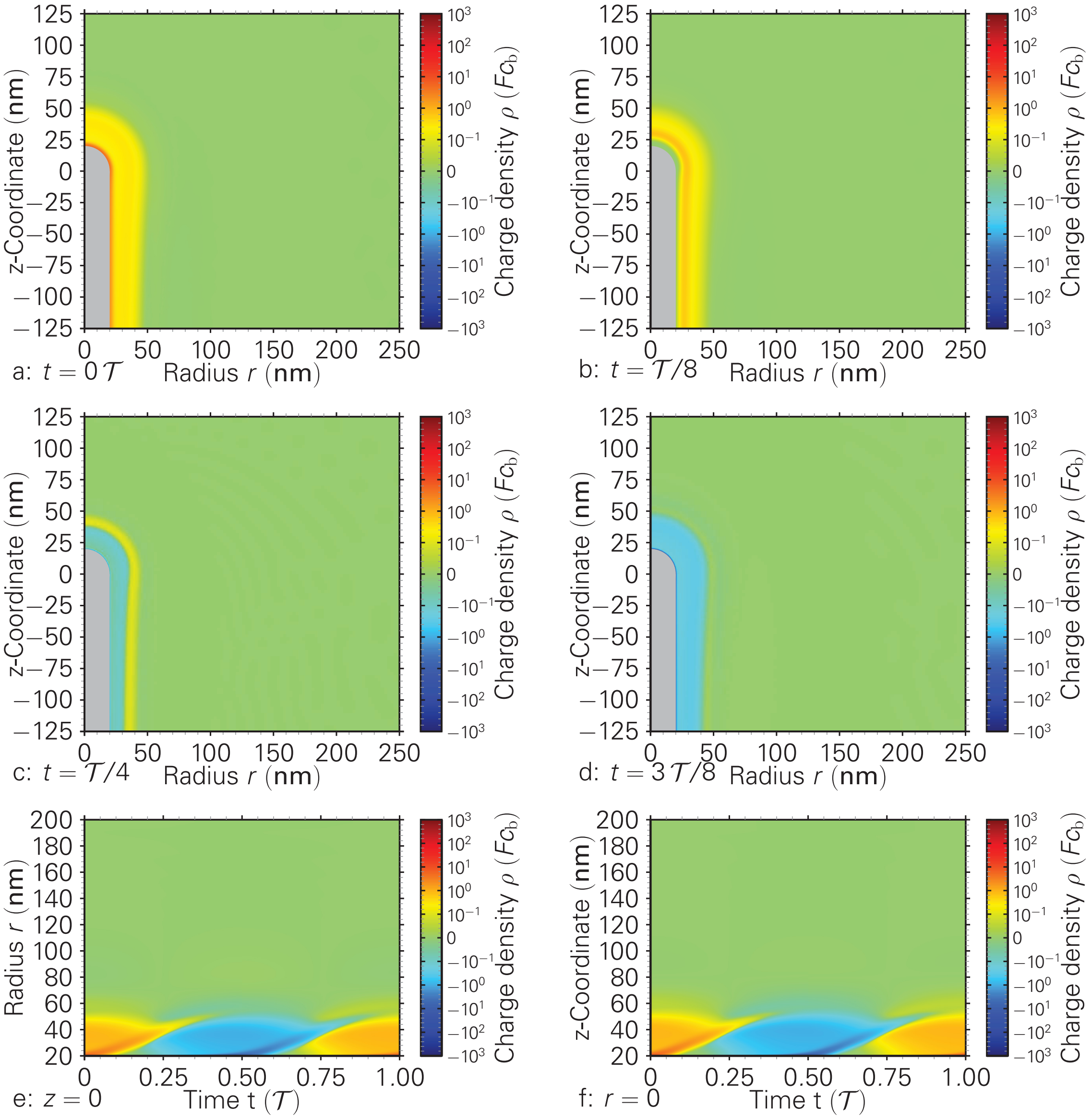

a: $t = 0\,\mathcal{T}$

b: $t = \mathcal{T}/8$

c: $t = \mathcal{T}/4$

d: $t = 3\,\mathcal{T}/8$

e: $z = 0$

f: $r = 0$

Figure 2.31: Spatio-temporal evolution of the charge density resulting from the two-dimensional solution of the PNP equations. Panels (a)-(d) show the charge density for the times $0\,\mathcal{T}$, $0.125\,\mathcal{T}$, $0.25\,\mathcal{T}$ and $0.375\,\mathcal{T}$. A radial (e) and axial (f) cut through the simulation domain illustrates the time dependence. Parameters: $f = 10\,\mathrm{MHz}$, $c_\mathrm{b} = 0.1\,\mathrm{mM}$, $V_0 = 5\,\mathrm{V}$, $r_1 = 20\,\mathrm{nm}$.

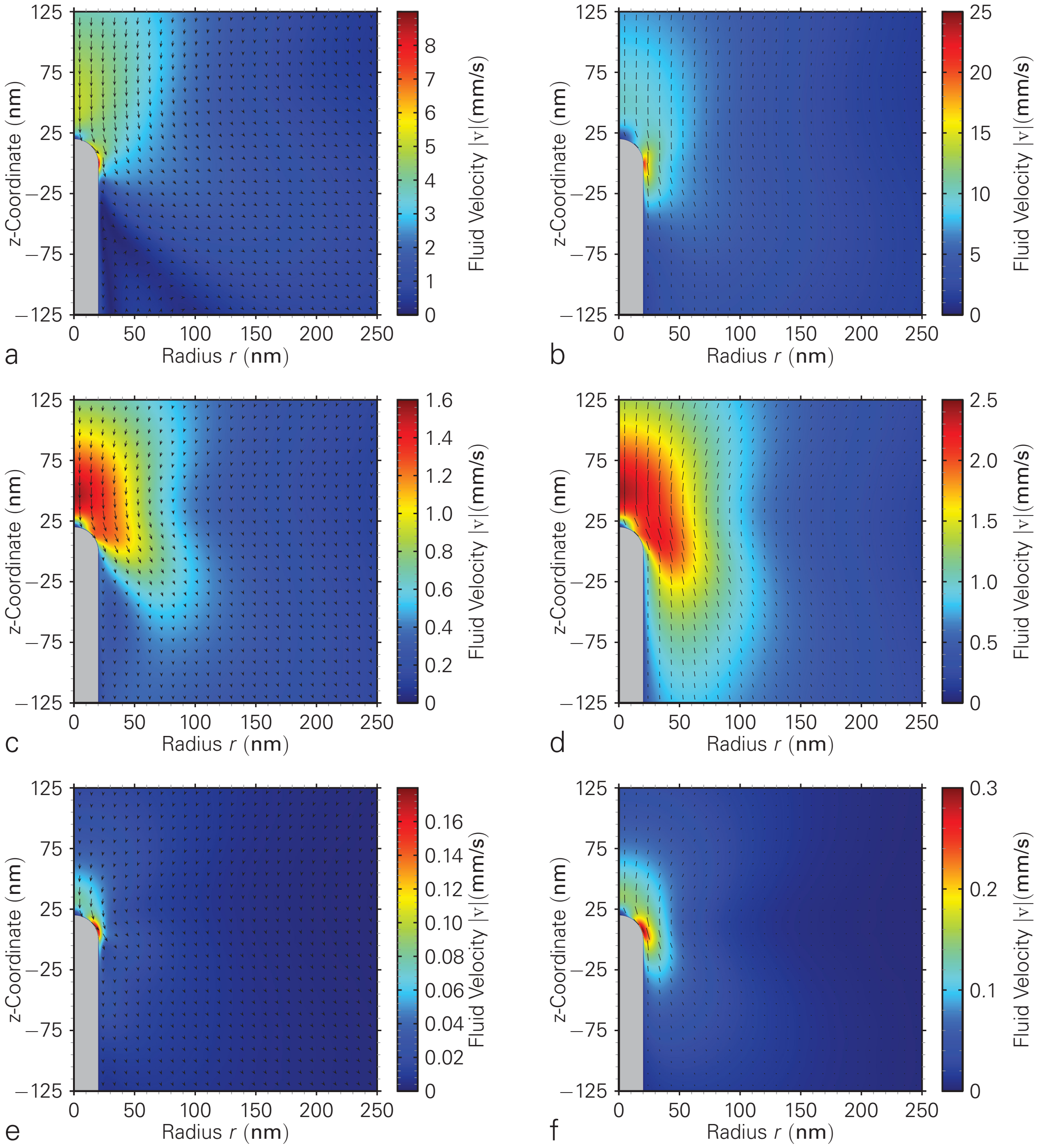

Figure 2.32: Magnitude and direction of the calculated velocity field of the fluid flow near the nanowire tip. The largest time-averaged fluid flow ($\omega = 0$) for 100 kHz (a), 1 MHz (c), and 10 MHz (e) is observed close to the cylinder axis and the nanowire. The direction of flow is antiparallel to the direction of wire growth. The largest principal value of the $\omega = 4\pi f$ mode of the fluid velocity for 100 kHz (b), 1 MHz (d), and 10 MHz (f) shows a similar distribution and orientation as the $\omega = 0$ component. Parameters: $c_b = 0.1$ mM, $V_0 = 5$ V, $r_1 = 20$ nm.

Based on the charge density and the electric potential results, the body force driving the fluid motion is calculated. The solution of the Fourier-transformed Navier–Stokes equation is shown in Figure 2.32. The simulation parameters used are the same as in Figure 2.26 and Figure 2.27 on page 50. The degree of agreement between this solution and the one from previous section depends on the considered frequency: for 100 kHz the flow pattern for the time-average as well as the doubled frequency is similar. Quantitatively, the fluid velocities are about a factor of 2 lower than what the simulations based on the one-dimensional geometry suggest. This overestimation is caused by applying the larger charge density of the spherical geometry at the cylindrical part of the wire as well. Moreover, the normal electric field at $z = 0$ is lower than that on a purely spherical electrode, which also reduces the charge density at the spherical tip.

For higher AC frequencies the one-dimensional estimation predicts a transition to an orientation reversal of the time-average flow pattern. This is not confirmed by Figure 2.32; instead, the fluid flow is directed towards the wire tip for all investigated frequencies. The flow amplitude for the time-average as well as for the higher harmonics decrease strongly with increasing excitation frequency. Additionally, the range of flow patterns are strongly reduced as well. The reason for this strong discrepancy again lies in the body force. The highly complex interaction between the charge density and the electric field apparently is very sensitive to its time average.

The qualitative character of the ACEO simulations based on a one-dimensional ion dynamics becomes obvious in the light of the improved two-dimensional simulations. But since the ACEO simulation based on one-dimensional ion densities are much faster and have a by far smaller memory consumption, they are well-fit to narrow down the interesting parameter space for detailed simulations. For the subsequent nanowire growth simulations, the improved accuracy of the two-dimensional ion dynamics is utilized.

2.6.3 Nanowire growth under the influence of ACEO fluid flow

The final step to complete the nanowire growth simulation for the DEP mechanism is to solve the transport equation for the neutral particles, Equation 2.95 on page 46, with the obtained fluid flow as an input. For this purpose, the more accurate estimation from section 2.6.2 is used. Of particular interest in this investigation is whether the influence of the ACEO fluid flow is capable of enhancing the simulated nanowire growth velocity to the experimentally observed level. By employing the Fourier transformed Navier–Stokes equation (Equation 2.99), each Fourier mode of the fluid flow velocity can be computed individually. However, since all higher Fourier modes describe a local periodic fluid motion in the vicinity of their respective equilibrium position, their contribution to the overall particle flux is expected to be negligible. Therefore, for the particle flux simulations only the time-averaged fluid flow is considered. The fluid flow amplitude varies with the AC frequency; for 100 kHz the maximum fluid velocity is 9 mm/s, for 1 MHz it is 1.6 mm/s and for 10 MHz it is 0.18 mm/s, see Figure 2.32.

Figure 2.33 compares the particle concentrations in the asymptotic growth regime for complexes (left panels) and clusters (right panels). The flux lines of the particle transport,

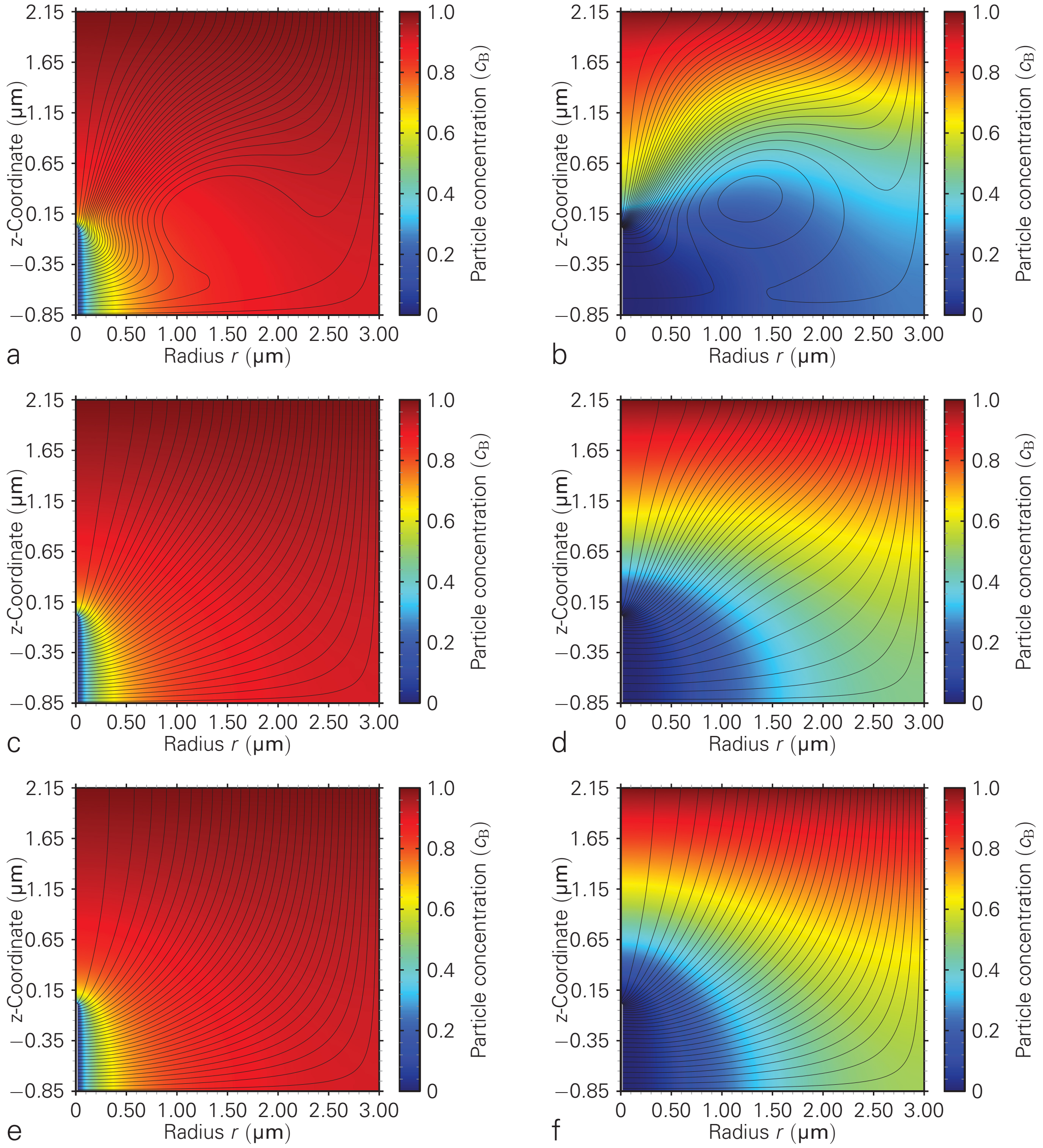

Figure 2.33: The asymptotic particle concentration and particle flux lines under the influence of diffusion, migration, and convection are shown for frequencies of 100 kHz (a, b), 1 MHz (c, d), and 10 MHz (e, f). The simulation results for complexes (a, c, e) exhibit a particle depletion only in the immediate vicinity of the nanowires and the flux lines are hardly affected by the fluid motion. For metal clusters with $r_\mathrm{p} = 13.5\,\mathrm{nm}$ (b, d, f) a long-range particle depletion is observed and for the largest fluid velocity (b) a significantly different flux line pattern arises. Parameters: $c_\mathrm{b} = 0.1\,\mathrm{mM}$, $V_0 = 5\,\mathrm{V}$, $r_1 = 20\,\mathrm{nm}$.

Equation 2.95, are shown as well. These correspond to the trajectories, which the complexes or clusters take in statistical average on their way from the reservoir (top edge of the simulation cell) to the wire surface (bottom left). Additionally, there are closed flux lines in panel (b). In statistical average, particles in this region follow the stream lines in counterclockwise orientation. The spacing between the flux lines describes the particle flux magnitude in the cylinder coordinate system, i.e. the denser the particle flux lines are, the more particles follow this trajectory. Therefore, the density of flux lines, which end at the nanowire surface, directly represents the nanowire growth velocity at this part of the surface.

The asymptotic concentration profile and the flux lines of the complexes are much less affected by the ACEO fluid flow than those of the clusters. From the modeling perspective, platinum complexes behave like single-atom clusters. Therefore, the comparison of complexes and clusters reflects the particle size dependence of the particle transport and the resulting nanowire growth. To work out the influence of the ACEO fluid flow, at first the case without convection, i.e. only diffusion and migration is revisited.

Since, at an applied AC frequency of 10 MHz, the amplitude of the fluid velocity is negligible (see also Figure 2.32e), Figure 2.33e and f approximate the convection-free case well. The diffusion flux is proportional to the diffusion coefficient D, which has a particle size dependence of r_p^{-1} (cf. Equation 2.15). Likewise, in section 2.3.2 the nanowire growth velocity, which is proportional to the sum of diffusion and migration fluxes, was found to be proportional to $r_\mathrm{p}^{-1/4}$. Therefore, it is concluded that the decrease of the diffusion flux resulting from an increased particle size is largely compensated by an increase in the migration flux owing to a larger dielectrophoretic force. The associated reweighting of the contributions to the total particle flux causes the depletion area near the nanowire (blue coloring of Figure 2.33e and f) to grow with increasing particle size. This depletion area is governed by the migration current, and particles within this region are quasi-immediately captured by the strong dielectrophoretic force in the vicinity of the nanowire tip.

The introduction of the ACEO fluid flow superimposes a convection to the particle flux. For sufficiently large fluid flow velocities, convection becomes dominant and the particle trajectories resemble the closed flux lines of the fluid flow (cf. Figure 2.32). As the comparison of clusters and complexes shows, the ACEO fluid velocity generated at $f = 100\,\mathrm{kHz}$ is sufficient to dominate the cluster transport, but for complexes only a local deformation of flux lines is observed. This highly particle-size-dependent response to the fluid flow has two reasons: first, the total particle flux is larger for a smaller particle size and thus for a given fluid velocity the convection flux accounts for a smaller fraction of it. Second, as with increasing particle sizes the migration-controlled depletion area near the nanowire tip expands, its boundary region with a particular steep concentration gradient is shifted outwards, compare Figures 2.33e and 2.33f. When the location of the fluid flow vortex coincides with this boundary region, the effect of the ACEO fluid flow on the particle transport is especially enhanced. Through the effect of convection, particle-rich solution is transported above the vortex from right to left and particle-depleted solution in the opposite direction below the vortex. Consequently, the cluster transport is channeled between the vortex and the nanowire axis, cf. Figure 2.33b. In contrast, if, due to a different particle size, the vortex is located inside either zone, the migration-controlled

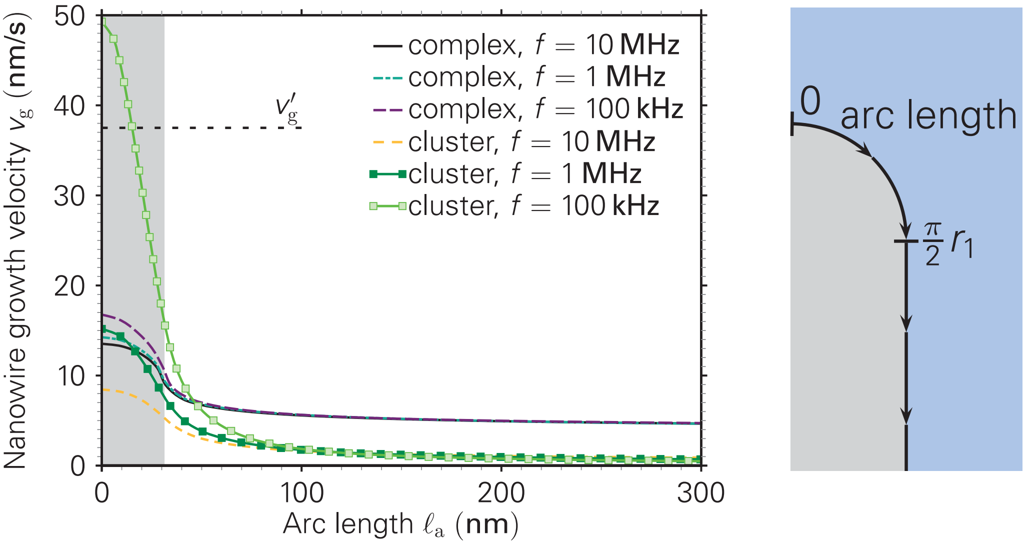

Figure 2.34: Distribution of the growth velocity over the nanowire circumference. The arc length is measured starting from $(0, r_1)$. The arc-segment associated to the wire tip is highlighted. Parameters: $c_b = 0.1$ mM, $V_0 = 5$ V, $r_1 = 20$ nm. The scaled experimental nanowire growth velocity $v_g' = 37.5$ nm/s is added for comparison.

depletion area or the diffusion-controlled region, the concentration gradient would be small. Then, convection would exchange solution volumes with a similar particle concentration and the overall influence of the ACEO fluid flow on the particle transport would be dramatically reduced.

The local distribution of the nanowire growth velocity resulting from the different cases of Figure 2.33 are compared in Figure 2.34. The velocity of nanowire growth from complexes exhibits only a small sensitivity towards the frequency change and the connected ACEO fluid flow. The growth velocity is maximal at the nanowire tip, but the wire shaft grows significantly as well, similar to the previous simulations without fluid flow, cf. Figure 2.7 on page 21. In contrast, the cluster-grown nanowires reveal a strong fluid-flow–and thus frequency–dependence. Moreover, due to the flow-induced redirection of flux lines, the nanowire growth from metal clusters is highly focused to the wire tip. A max/min-ratio of growth velocity of up to 100:1 makes it likely that nanowires grown in this manner are much thinner and straighter than their complex-grown counterparts.

To assess the potential for optimization of the nanowire morphology, in particular regarding the reduction of their thickness, a geometric scaling is considered. This approach allows to retrieve the parametric changes necessary for a further miniaturization of the nanowires. Under the prerequisite of negligible ion crowding, i.e. for sufficiently high AC frequencies, a scaling law with the scaling factor k exists:

$$\mathbf{x}' = k\,\mathbf{x} \tag{2.101a}$$

$$t' = k^2\, t \tag{2.101b}$$

$$f' = f/k^2 \tag{2.101c}$$

$$c_\mathrm{b}' = c_\mathrm{b}/k^2 \tag{2.101d}$$

$$V_0'(t') = V_0(t) \tag{2.101e}$$

$$\varphi'(\mathbf{x}', t') = \varphi(\mathbf{x}, t) \tag{2.101f}$$

$$c_i'(\mathbf{x}', t') = c_i(\mathbf{x}, t)/k^2 \tag{2.101g}$$

$$\mathbf{f}'(\mathbf{x}', t') = \mathbf{f}(\mathbf{x}, t)/k^3 \tag{2.101h}$$

$$\mathbf{v}'(\mathbf{x}', t') = \mathbf{v}(\mathbf{x}, t)/k \tag{2.101i}$$

$$p'(\mathbf{x}', t') = p(\mathbf{x}, t)/k^2 \tag{2.101j}$$

In the primed coordinate system $(\mathbf{x}', t')$ the PDE solution for the ion dynamics and ACEO fluid flow are expressed by the numerical results of the unprimed system. This scaling law can be verified by applying it to the original PDE system Equation 2.93 and Equation 2.94 on page 46. The convection-diffusion equation, Equation 2.95, has an approximate scaling law, which employs the fact that the migration flux is strongly localized directly at the nanowire. Then, at greater distances, for the growth-limiting convection and diffusion particle flux there holds in time average:

$$c_\mathrm{p}' = c_\mathrm{p} \tag{2.102a}$$

$$v_\mathrm{g}' \approx v_\mathrm{g}/k \tag{2.102b}$$

$$c'(\mathbf{x}') \approx c(\mathbf{x}) \tag{2.102c}$$

$$\mathbf{j}'(\mathbf{x}') \approx \mathbf{j}(\mathbf{x})/k \tag{2.102d}$$

The intended application of the presented scaling laws is to reduce the nanowire diameter, while preserving the electrode gap distance. This is an inconsistency in the geometric scaling. However, since the electric field near the nanowire is the major drive for the ion flux and the ACEO fluid flow, the incorrect scaling of the electrode gap distance has a negligible effect on the overall results.

The established scaling laws allow for a comparison of simulations and experiments with different wire radii, which is particularly useful as the experimental nanowires have a rather broad tip radius distribution. In the experiments at 300 K, nanowires with a radius of about $r_1 \approx 50\,\mathrm{nm}$ grow with an average velocity of $v_\mathrm{g} = 15\,\mathrm{nm/s}$, cf. Figure 2.10 on page 23. To enable the comparison with the modeling results, the radius is scaled to $r_1 = 20\,\mathrm{nm}$, which corresponds to $k = 0.4$. The obtained, scaled growth velocity is $v_\mathrm{g}' = 37.5\,\mathrm{nm/s}$. In Figure 2.34 this scaled nanowire growth velocity is compared to the simulation results. Considering that the growth model assumes an idealized, instant particle deposition, a higher theoretical than experimental growth velocity is expected. Therefore, only the nanowire growth from metal clusters in the presence of a strong ACEO fluid flow (up to 8.5 mm/s at a frequency of $f = 100\,\mathrm{kHz}$) predicts a sufficiently large growth velocity. Additionally, only this case shows a particle deposition sufficiently anisotropic to produce long and thin nanowires, cf. Figure 2.34. These two facts prove that first, platinum clusters are the main precursor for the nanowire assembly, and second that for the investigated parameter range the ACEO fluid flow plays an integral role in it.

These insights in the nanowire growth mechanism explain also the dependence of the nanowire growth velocity on the platinum salt concentration, as shown in Figure 2.11 on page 24. During the preparation of the aqueous solution, further ions are added together with the platinum complexes, which are converted to platinum cluster during the aging process. As described in section 2.6.1, the ACEO fluid velocity is approximately proportional to the electrolyte concentration. Thus, a linearly increasing growth velocity with

Table 2.3: Influence of the experimental process parameters on the three particle flux contributions according to Equation 2.95.

	diffusion	**convection**	**migration**
c_p	A lower particle concentration leads to a larger characteristic transport length r_s, which emphasizes the influence of the convection.		
r_p	inverse to particle size	no influence	increases with particle size
c_b	no influence	increases with ion concentration	below the lower transition frequency ($\propto c_\mathrm{b}$) a strong field screening narrows down the migration-controlled depletion region and decreases the migration flux outside
f	no influence	largest between lower and upper transition frequency	
V	no influence	increases with voltage amplitude	increases with voltage amplitude

platinum salt concentration is expected. However, with increasing ion concentrations the lower and the upper transition frequency, ω_{T1} and ω_{T2}, rise as well. Ultimately, effects like electric field screening and crowding limit the ACEO fluid velocity, which presumably is responsible for the saturation of the nanowire growth velocity at larger concentrations.

2.6.4 Model-based optimization of the dielectrophoretic nanowire growth

The model provides important leads on how to reduce the size and to improve the straightness of nanowires grown according to an existing protocol. According to the scaling laws, Equation 2.101 and Equation 2.102, this goal can be achieved by choosing the scaling factor as $k < 1$. This requires an increase in the AC frequency and the ion concentration simultaneously, while keeping the voltage amplitude constant.

Beyond the scaling law, an in-depth analysis of the particle fluxes reveals additional potential for optimization. As a general rationale, the flux lines of the particle flux need to focus at the nanowire tip, similar to the example of Figure 2.33b. To achieve this goal, it is essential to tailor the three contributions to the total particle flux (cf. Equation 2.95), diffusion, convection, and migration. First, as the comparison of clusters and complexes shows, a dominant diffusion causes an almost isotropic particle deposition. Thus, to avoid this, the relative influence of diffusion on the total particle flux has to be minimized. Second, a strong convection flux due to the ACEO fluid flow bends the flux lines, so more flux lines pass between the vortex center and the nanowire. Consequently, to promote the growth of straight and thin nanowires, the influence of convection flux should be maximized. Lastly, the migration is responsible for extracting the particles from the fluid flow in the vicinity of the nanowire tip. As discussed previously, the migration flux should be adjusted such that the edge of the migration-controlled depletion area is close to the fluid flow vortex.

Table 2.3 summarizes the influence, which the experimental parameters (particle concentration and radius, ion concentration, AC frequency and AC voltage) have on the three discussed particle flux contributions. Accordingly, suggestions on how to grow thin and straight nanowires are developed:

1. A low particle concentration should be employed.
2. Although Table 2.3 suggests the use of large particles, the particle size also determines the minimal wire diameter. Therefore, if one additionally requires a homogeneous wire morphology, the maximum particle size should be considerably smaller than the desired wire diameter.
3. A high ion concentration and an AC frequency slightly below the corresponding upper transition frequency should be chosen.
4. Depending on the previous choices, the AC voltage is determined to locate the edge of the depletion zone close to the ACEO fluid flow vortex in order to maximize the channeling effect of the convection transport.
5. The electrode geometry and the number of nucleation sites on it have a complex influence on the ACEO flow pattern, so no general recommendation can be given. However, to enable the formation of long-range ACEO fluid flow patterns, the typical distance between the electrodes and different nanowires should be at least in the order of 1 µm.

2.7 ION-BASED NANOWIRE GROWTH (DENA)

The nanowire growth mechanism investigated in the previous sections is based on the growth from neutral particles, i.e. from electrically neutral chemical complexes or from neutral metal clusters. In this section, the mechanism of directed electrochemical nanowire assembly (DENA) is considered. In this process the nanowire is grown from metal containing ions that undergo an electrochemical reaction at the nanowire surface, in which the metal is reduced. Finally, these metallic atoms are deposited and the nanowire grows. As precursor for the DENA nanowire growth cations like Cu^{2+} [16] or Pd^{2+} [25], as well as anions like $[\mathrm{PtCl}_6]^{2-}$ [26] may be used. Under suitable conditions, anion-based DENA is known to yield straight and particularly thin nanowires [70], which are superior to nanowires grown from cations. Therefore, this work concentrates on the anion mechanism, which is investigated by the example of a $\mathrm{H}_2\mathrm{PtCl}_6$ solution. Further explanation on how to prepare such solutions and a brief description of the hydrolysis of the produced $[\mathrm{PtCl}_6]^{2-}$ anion are given in section 2.1. For the electrochemical deposition of platinum, a cathodic and an anodic partial reaction need to be considered

$$\begin{array}{rcl}
[\mathrm{PtCl}_6]^{2-}(\mathrm{aq}) + 4\,e^- & \longrightarrow & \mathrm{Pt}\,(\mathrm{s}) + 6\,\mathrm{Cl}^-(\mathrm{aq}) \\
4\,\mathrm{Cl}^-(\mathrm{aq}) & \longrightarrow & 2\,\mathrm{Cl}_2(\mathrm{g}) + 4\,e^- \\
\hline
[\mathrm{PtCl}_6]^{2-}(\mathrm{aq}) & \longrightarrow & \mathrm{Pt}\,(\mathrm{s}) + 2\,\mathrm{Cl}^-(\mathrm{aq}) + 2\,\mathrm{Cl}_2(\mathrm{g})
\end{array} \tag{2.103}$$

Notably, the two major hydrolysis products of $[\mathrm{PtCl_6}]^{2-}$, $[\mathrm{PtCl_5(H_2O)}]^{-}$ and $[\mathrm{PtCl_5(OH)}]^{2-}$, undergo a very similar reduction.

The underlying principle of DENA to grow nanowires relies on a locally selective metal deposition. The necessary electrochemical reduction of the anionic precursor is inhibited in the bulk solution, but triggered by the high electric field at the nanowire tip. Thereby, a homogeneous metal coating of the electrodes is avoided and a nanowire morphology is obtained. Since the transfer of electrons is involved in the metal deposition reaction, it is presumed that only in the vicinity of the electrodes this conversion can take place. As platinum is a very noble metal, the reaction is considered to be irreversible. Since the reduction step is crucial for the nanowire growth, a kinetic model of this reaction is needed. In the following, three schemes are proposed to model this field-activated reaction. For each model, the field sensitivity of the respective reaction constant k_r is evaluated.

2.7.1 Reaction models of platinum reduction

Field-assisted thermal activation For this model, it is assumed that the rate-limiting process of the platinum reduction is the decomposition of the platinum complex ion after an electron has been transferred from the electrode, e.g.

$$[\mathrm{PtCl_6}]^{2-} + 1\,e^- \rightleftharpoons [\mathrm{PtCl_5}]^{2-} + \mathrm{Cl}^- \cdot \tag{2.104}$$

This reaction creates a highly unstable intermediate species, which in turn undergoes fast follow-up reactions. The electron hopping from the electrode to the complex in the presence of the electric field accounts for an additional activation of the reaction. The amount of additional activation energy is determined by the hopping distance ℓ and the electric field E as $\Delta E_\mathrm{a} = e\,\ell\,E$. Assuming a first-order kinetic of the reaction, an Arrhenius equation is used to model the reaction rate for the initial decomposition

$$k_\mathrm{r} \propto \exp\left(\frac{-E_\mathrm{a}^0 - \Delta E_\mathrm{a}}{k_\mathrm{B} T}\right) \propto \exp\left(\frac{e\,\ell\,E}{k_\mathrm{B} T}\right), \tag{2.105}$$

where E_a^0 is the activation energy in the absence of an electric field. The hopping length is in the order of the ion diameter including the hydration shell, $\ell \approx 0.5\,\mathrm{nm}$. Based on the previous results, cf. Figure 2.19, the electric field is assumed to be in the order of $2 \times 10^8\,\mathrm{V/m}$. These estimations yield an additional activation energy of 0.1 eV, which corresponds to an increase of the reaction constant by a factor in the order of 100 due to the electric field.

Electron tunneling as rate determining step The second mechanism reconsiders the reaction of Equation 2.104, but here the electron transfer via tunneling from the electrode to the complex ion is assumed to be the rate-determining step. Simmons [94] derived a generalized formula for tunneling currents through thin barriers, depending on the applied voltage and the barrier height. The tunneling can happen even if the complex anion is not adsorbed directly at the metal surface. Therefore, a tunneling length in the order of $\ell \approx 1$ nm is assumed. With the typical electric field of 2×10^8 V/m, a tunneling voltage of 0.2 V is obtained. However, the mean barrier height is of a similar order as the work function, which for platinum – depending on the crystal facet – is around 5.6 eV [72]. Consequently, the activation by the tunneling voltage is much smaller than the average barrier height, which means the tunneling junction has an ohmic characteristic [94]. Therefore, the tunneling current and thus also the reaction rate is proportional to the electric field

$$k_\mathrm{r} \propto |\mathbf{E}| \, . \tag{2.106}$$

Field-induced bond weakening The third, discussed mechanism considers the field-induced decomposition of the platinum complex anion according to

$$[\mathrm{PtCl_6}]^{2-} \rightleftharpoons [\mathrm{PtCl_5}]^{-} + \mathrm{Cl}^{-} \tag{2.107}$$

as the rate-limiting step. In this scenario, the large electric field causes a strong polarization of the complex anion. The polarization affects the originally symmetric electron density so that one particular Pt–Cl bond is weakened and the thermal activation suffices to split the complex anion at this bond.

To study the electron density under the influence of external electric fields, the program CP2K was used. "CP2K is a program to perform atomistic and molecular simulations of solid state, liquid, molecular, and biological systems. It provides a general framework for different methods such as e.g., density functional theory using a mixed Gaussian and plane waves approach and classical pair and many-body potentials."[95].

The calculations of $[\mathrm{PtCl_6}]^{2-}$ in vacuum under the influence of an external electric field have been carried out by Dr. Arezoo Dianat. Figure 2.35 shows the resulting electron density distribution for the cases with and without an applied external electric field. The positions of chlorine atoms are shifted relative to the platinum atom in the direction opposing the electric field. Therefore, the bond lengths along the x-axis become highly asymmetric. Additionally, the electron density of the bonds are extremely different.

To estimate the reaction rate constant k_r of the complex splitting, the reaction barrier for this reaction is needed, which has been determined by a variant of the nudged elastic band method [96]. To this end, the evolution of the total energy has been monitored as the length of one Pt–Cl bond was gradually increased. The difference between the obtained maximum total energy and the relaxed state is 1.82 eV in the absence of an external electric field. However, due to technical limitations of the CP2K software, an analog nudged elastic band study in the presence of an external electric field failed. In detail, the CP2K software employs Lagrange multipliers to determine the energy optimum with the constraint of a fixed Pt–Cl bond length. That means the calculated electric potentials of the molecules are superimposed by additional Lagrange terms, that could not be separated in a post processing scheme from the intended results.

Therefore, the bond energy was estimated alternatively for the cases with an external electric field of $E = 200$ MV/m and $E = 400$ MV/m. In a first step, the molecular structure of the $[\mathrm{PtCl_6}]^{2-}$ molecule is optimized in the external electric field and its total energy

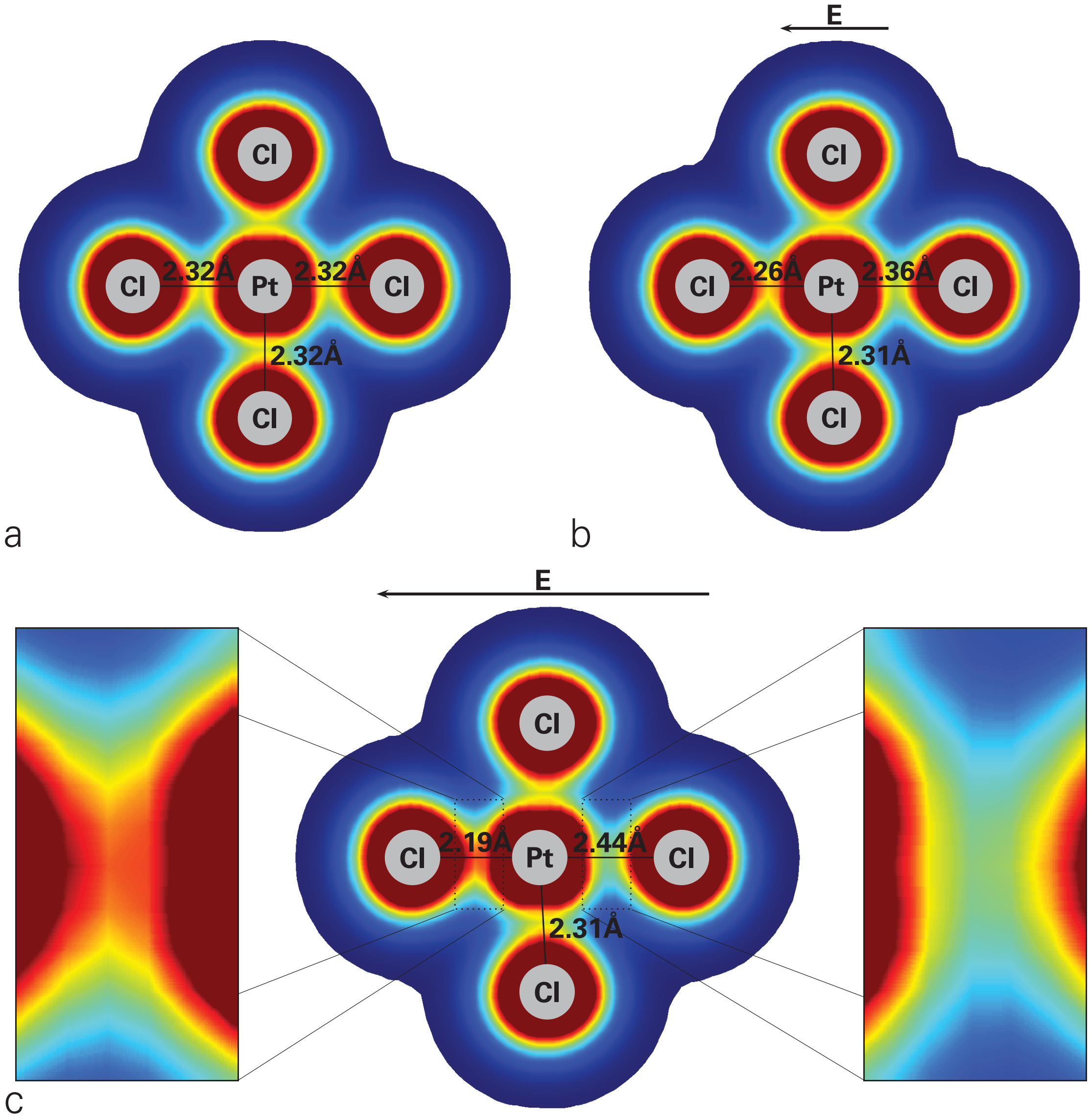

Figure 2.35: The figure shows cuts through the electron density of $[PtCl_6]^{2-}$ for three electric field strengths: a) $E = 0\,\mathrm{V/m}$, b) $E = 2 \times 10^8\,\mathrm{V/m}$ and c) $E = 4 \times 10^8\,\mathrm{V/m}$. In panel c) the stretched and compressed Pt−Cl bonds are displayed in an enlarged inset. The color scale (electron density) has been cut to the range from 1.25×10^{-3} to $0.15 e/a_0^3$, where a_0 is the Bohr radius. CP2K calculations by Dr. Arezoo Dianat.

determined. Afterwards, the procedure is repeated for the reaction products, $[PtCl_5]^-$ and Cl^-. The difference of the combined energies of both products and the energy of the educt is used as the approximation for the bond energy. This estimation does not include energy contributions from moving the charged molecules in the external and intramolecular electric fields. As shown for the first reaction model, the energy contributions of a net charge of one electron are in the order of 0.1 eV, which is a comparatively small value. To emphasize the quality of this estimation, the bond energy for the field-free case was calculated in that manner, too. From the calculation results (cf. Table 2.4) it can be seen that the estimations in fact differs only by 0.15 eV. Moreover, please note that the neglected energy contributions of the charged ions in the external electric field facil-

Table 2.4: Summary of CP2K simulation results for $[PtCl_6]^{2-}$ in vacuum under the influence of strong electric fields. The bond energies are defined as the energy difference between the relaxed configuration of $[PtCl_6]^{2-}$ and the unbound state of the two separate fragments $[PtCl_5]^-$ and Cl^-. The reaction barrier has been determined by a nudged elastic band method.

electric field (MV/m)	0	200	400
min. bond length	2.32	2.26	2.19
max. bond length	2.32	2.36	2.44
med. bond length	2.32	2.31	2.31
bond energy	1.67 eV	0.15 eV	−0.38 eV
reaction barrier	1.82 eV	n/a	n/a

itates the bond splitting. Thus, the presented approximation *underestimates* the effect of field-induced bond weakening.

As Table 2.4 shows, at an external electric field of 200 MV/m, the energy of the electron enriched bond is 0.15 eV, i.e. dramatically lower than for $E = 0$ MV/m. This huge change in the bond energy is much more than what could be explained by electric polarization or electric potential differences alone. To analyze the phenomenon, the basic principles of molecular orbital (MO) theory are considered. The Pt−Cl bonds are coordinative σ-bonds, which means that any partial charges on the chlorine populate an anti-bonding MO. Since the binding MO is fully populated whereas the anti-bonding MO is only partially, an overall bonding effect is observed. In the ground state the $[PtCl_6]^{2-}$ is highly symmetric (cf. Figure 2.35a): all negative partial charges of the chlorine atoms and thus all Pt−Cl bond energies are equal. On the other hand, in the presence of a large external electric field, the $[PtCl_6]^{2-}$ molecule is highly polarized and the partial charges on the chlorine ions are redistributed, see Figure 2.35c. The right chlorine in panel c exhibits a drastically increased partial charge; the left chlorine's partial charge is reduced by about the same amount. Hence, the energies of the left bond is increased strongly and of the right bond is decreased by a similar amount. Consequently, the resulting change of the total energy due to the external electric field is much smaller than the bond weakening effect. The sensitivity of the reaction barrier with respect to the applied electric field is determined from the bond energy. For an electric field around 2×10^8 V/m it is approximately given by a central difference as

$$\frac{\partial E_\mathrm{a}}{\partial E} \approx \frac{E_\mathrm{a}(400\,\mathrm{MV/m}) - E_\mathrm{a}(0\,\mathrm{MV/m})}{400\,\mathrm{MV/m}} = -5 \times 10^{-9}\, e\,\mathrm{m}. \tag{2.108}$$

This leads to a field dependence of the reaction rate according to

$$k_\mathrm{r} = k_0 \exp\left(\frac{\partial E_\mathrm{a}}{\partial E}\frac{E}{k_\mathrm{B}T}\right), \tag{2.109}$$

with k_0 as a constant of proportionality. In the absence of an electric field, the reaction is inhibited due to the high reaction barrier (see Table 2.4). At $E = 4 \times 10^8$ V/m the reaction enthalpy is negative and only a very small, if any, reaction barrier is expected. Therefore, at this large applied field the considered reaction and thus the deposition of platinum is anticipated to happen quasi-instantaneously.

2.7.2 Simplifications of the transport equations in the context of DENA

The ion transport simulation under high AC electric fields, section 2.5.2, has so far considered only chemically inert ions. In the deposition reaction, Equation 2.103, however, metal-rich multivalent anions decompose to solid metal, multiple monovalent metal-free anions, and other uncharged reaction products. Using the results from section 2.5.3, in the following it is shown that for large frequencies ($\omega \gg \omega_{\mathrm{T1}}$) multivalent ions behave similarly to an equivalent amount of monovalent ions. Subsequently, this property of the numerical solution is exploited to simplify the calculation scheme further.

To analyze the effect of ion valences, Equations 2.67 and 2.89 are reconsidered

$$\omega_{\mathrm{T2}} = 2\, z\, D\, e\, F\, c_{\mathrm{b}}/(\varepsilon\, k_{\mathrm{B}} T), \tag{2.110a}$$

$$V_{\mathrm{d}}(\omega) = \frac{\omega_{\mathrm{T}}}{\imath\,\omega + \omega_{\mathrm{T}}}\, V, \tag{2.110b}$$

$$E(r_1,\omega) = \frac{V}{r_1^d\, h_d(r_2)}\,\frac{\imath\,\omega + \omega_{\mathrm{T2}}}{\imath\,\omega + \omega_{\mathrm{T}}}, \tag{2.110c}$$

$$E(r,\omega) = \frac{V}{r^d\, h_d(r_2)}\,\frac{\imath\,\omega}{\imath\,\omega + \omega_{\mathrm{T}}}, \qquad r_{\mathrm{b1}} < r < r_{\mathrm{b2}}, \tag{2.110d}$$

$$Q(\omega) = \frac{-A_{\mathrm{d}}(r_1)\,\varepsilon\, V}{r_1^d\, h_d(r_2)}\;\frac{\omega_{\mathrm{T2}}}{\imath\,\omega + \omega_{\mathrm{T}}}. \tag{2.110e}$$

Notably, in all balanced reaction equations considered in this work, the total amount of ionic charges is preserved, i.e. $\sum_i |z_i|\, c_i$ is constant. That means, if through reaction all bivalent anions in the solution are converted to two monovalent anions, the upper transition frequency ω_{T2} in Equation 2.110a is unaffected, since $z_i\, c_i$ is constant in the reaction. Generalizing the consideration of section 2.5.3, this invariant of the upper transition frequency is also found in mixtures of mono- and multivalent ions that are present in the ongoing nanowire growth reaction.

Furthermore, in the high-frequency range there holds $\omega_{\mathrm{T}} \approx \omega_{\mathrm{T1}} \ll \omega$. Therefore, ω_{T} can be neglected in Equations 2.110b–e. Consequently, the voltage drop over the double layer, the electric fields at the electrode and in the bulk region, and the overall amount of charges in the double layer are the same throughout the whole quasi-stationary nanowire growth.

As given in section 2.5.3, the particle flux in the bulk zone at high frequencies is

$$\mathbf{j}_i(r) = D\, z_i\, c_i\, \mathbf{E}(r). \tag{2.111}$$

Since $\sum_i z_i\, c_i$ for all anion types and $E(r)$ are reaction-independent, the sum of all anion particle fluxes $\sum_i z_i\, \mathbf{j}_i(r)$ in the bulk zone is too. Through the reaction equation the consumption of multivalent anions is directly linked to the creation of monovalent anions. Therefore, at the electrode, the sum of all anion fluxes is zero $\sum_i z_i\, \mathbf{j}_i(r_1) = \mathbf{0}$ as before in the blocking electrode boundary condition. The charge balance, Equation 2.110e, states that the overall amount of anions (and cations) in the double layer between the electrode and the bulk zone is reaction-independent. Only, the local distribution of anions differs slightly. A more comprehensive analysis of the anion concentration in the double layer is presented in section 2.7.3 on page 74 and following. Since also in the double layer $\sum_i z_i\, c_i$ is approximately equal for the cases of mono- and multivalent anions at all times, $\sum_i z_i\, \frac{\partial}{\partial t} c_i$ and therefore also $\sum_i z_i\, \mathbf{j}_i$ are roughly reaction-independent. In summary, the sum of particle fluxes at the electrode, in the double layer and in the bulk zone are not affected by the reaction that converts multivalent to monovalent anions. Therefore, without loss of generality, it is sufficient to discuss only monovalent ions in the following.

Introducing the concentrations of metal-rich anions c_{a1} and of metal-free anions c_{a2}, the total anion concentration can be expressed as $c_2 = c_{\mathrm{a1}} + c_{\mathrm{a2}}$. Then, applying the definition of the chemical potential (Equation 2.42) to the transport equation (Equation 2.41b) yields

$$\begin{aligned} \mathbf{j}_{\mathrm{a1}} + \mathbf{j}_{\mathrm{a2}} &= -\frac{D}{k_{\mathrm{B}} T} \left[c_{\mathrm{a1}} \nabla(\mu_{\mathrm{a1}} + z_2\, e\, \varphi) + c_{\mathrm{a2}} \nabla(\mu_{\mathrm{a2}} + z_2\, e\, \varphi) \right] \\ &= -\frac{D}{k_{\mathrm{B}} T} (c_{\mathrm{a1}} + c_{\mathrm{a2}}) \nabla\!\left(k_{\mathrm{B}} T \log \frac{c_{\mathrm{a1}} + c_{\mathrm{a2}}}{c_{\max} - (c_1 + c_{\mathrm{a1}} + c_{\mathrm{a2}})} + z_2\, e\, \varphi\right) \qquad (2.112) \\ &= -\frac{D}{k_{\mathrm{B}} T}\, c_2 \nabla(\mu_2 + z_2\, e\, \varphi) = \mathbf{j}_2 . \end{aligned}$$

Equation 2.112 shows that the superposition of several, chemically different anion species with the same valence and diffusion coefficient behaves like one indistinguishable anion species. Therefore, it is possible to decouple the ion transport according to the PNP equations entirely from the chemical conversion of anion species during the nanowire growth reaction. The striking advantage of this procedure is that the PNP equations can be solved with fewer degrees of freedom (as there are fewer concentration variables) and, even more important, the convergence acceleration (presented in the numerical methods on page 89) becomes applicable. Most appealing, however, is that the comparison of different reaction conditions and models does not require to recompute the asymptotic periodic state of the ion dynamics, but only the computationally much cheaper calculation of the anion reaction needs to be repeated. The described optimizations provides an essential contribution to the speed-up of the calculation process that enables the simulation of wire-like two dimensional geometries.

For the concentration of the metal-rich anions the ansatz $c_{\mathrm{a1}} = g\, c_2$ is chosen. Then their particle flux becomes

$$\mathbf{j}_{\mathrm{a1}} = -\frac{D}{k_{\mathrm{B}} T}\, g\, c_2 \nabla \left(k_{\mathrm{B}} T \log \left(\frac{g\, c_2}{c_{\max} - (c_1 + c_2)} \right) + z_2\, e\, \varphi \right) = g\, \mathbf{j}_2 - D\, c_2 \nabla g. \qquad (2.113)$$

From the continuity equation of the metal-rich anion species, the governing partial differential equation for g is derived as

$$0 = \frac{\partial}{\partial t} c_{\mathrm{a1}} + \nabla \cdot \mathbf{j}_{\mathrm{a1}} \qquad (2.114)$$

$$0 = c_2 \frac{\partial}{\partial t} g + g \frac{\partial}{\partial t} c_2 + g \nabla \cdot \mathbf{j}_2 + \mathbf{j}_2 \cdot \nabla g - D \nabla c_2 \cdot \nabla g - D\, c_2 \nabla^2 g \qquad (2.115)$$

$$0 = c_2 \frac{\partial}{\partial t} g + (\mathbf{j}_2 - D \nabla c_2) \cdot \nabla g - D\, c_2 \nabla^2 g + g \left(\frac{\partial}{\partial t} c_2 + \nabla \cdot \mathbf{j}_2 \right) \qquad (2.116)$$

$$0 = \frac{\partial}{\partial t} g - \frac{D}{k_{\mathrm{B}} T} \nabla \left(\mu_2 + z_2\, e\, \varphi + k_{\mathrm{B}} T \log(c_2 / c_{\mathrm{b}}) \right) \cdot \nabla g - D \nabla^2 g, \qquad (2.117)$$

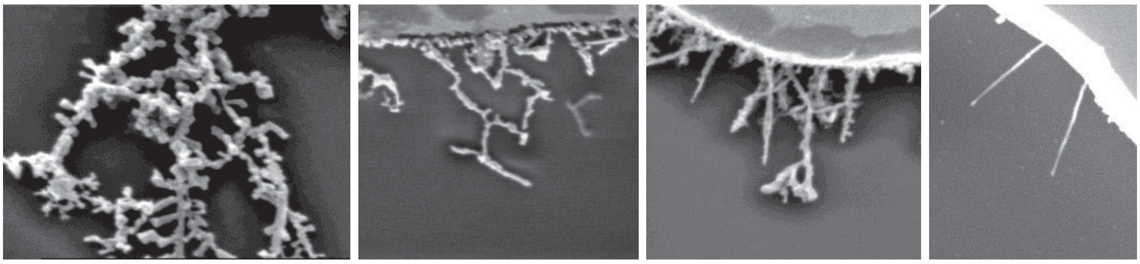

Figure 2.36: The SEM images of platinum nanowires reveal a strong influence of the signal form of the applied AC voltage on the nanowire morphology. From left to right a square wave signal is approximated with an increasing number of Fourier components n ($n = 3$, $n = 4$, $n = 6$, and a true square wave signal), cf. Equation 2.120. Reprinted with permission from [97]. Copyright 2014 American Chemical Society.

where in Equation 2.116 the continuity equation for c_2 has been used. At the nanowire surface, the particle flux of metal-rich anions is given by the reaction rate

$$\mathbf{j}_{\mathrm{a1}} \cdot \mathbf{n} = k_{\mathrm{r}}\, c_{\mathrm{a1}}. \tag{2.118}$$

Thus, in combination with Equation 2.113 the boundary conditions of g at the nanowire is given by

$$-D\, \nabla g \cdot \mathbf{n} = k_{\mathrm{r}}\, g. \tag{2.119}$$

The second boundary is placed inside the bulk region of the electrolyte. Because of a huge reservoir of platinum-rich ions in the solution drop and the mixing of the solution through AC electro-osmosis, the concentration of metal-rich anions at the second boundary is assumed to be the same as in a freshly prepared solution. Remarkably, due to the stoichiometry of $\mathrm{H_2PtCl_6}$, the platinum anion concentration is only one half of the concentration of monovalent anions, i.e. $c_{\mathrm{a1}} = 0.5\, c_2$. Accordingly, the boundary conditions at the nanoelectrode ($r = r_1$) becomes $g = 0.5$.

2.7.3 Influence of AC signal form and frequency on the nanowire growth

The anionic DENA mechanism reveals a strong sensitivity towards the signal form of the applied AC voltage. For illustration, SEM images of nanowires grown by A. Nerowski [97] are shown in Figure 2.36. In this image series the signal form was gradually changed from a sine wave to a square signal. To this end, the Fourier series of a square signal was truncated after the nth term, where n was increased from 1 (pure sine) to ∞ (square signal)

$$V(t) = V_0(n) \sum_{k=1}^{n} \frac{\sin\left((2k-1)\,\omega\, t\right)}{2k-1}. \tag{2.120}$$

To achieve comparable results, the amplitude $V_0(n)$ was chosen to keep the signals RMS value constant at $V_{\mathrm{RMS}} = 7\,\mathrm{V}$. The remaining parameters were $c_{\mathrm{b}} = 0.2\,\mathrm{mM}$ and $f = 1\,\mathrm{MHz}$.

In fact, for $n = 1$ no growth of nanowires occurred during the experiments, while for the square signal extraordinary thin, straight and unbranched wires were grown. This striking difference is due to the behavior of the metal-rich anions. Generally, to grow nanowires, a large ion concentration and a field activation of the metal reduction reaction are needed. However, in the negative half-wave, when electrons are in excess and a reduction is facilitated, the anion concentration is low due to the field repulsion. On the other hand, in the positive half-wave, the anions are accumulated at the nanowire surface, but the reduction of platinum is inhibited. To grow nanowires nevertheless, the polarity change from positive to negative needs to have a high slew-rate. Thereby, the reduction is enabled before the majority of anions is repelled too far from the electrode to allow for a charge transfer from the electrode to the platinum complex. For a quantitative analysis of this mechanism, the ion concentrations and electric potential have been simulated using the PNP equations (cf. section 2.5) for a sine and a square wave. The time-dependent simulation results are shown in Figure 2.37 as a parametric plot of the total anion concentration versus the electric field at the nanowire surface. The total anion concentration serves as an upper bound to characterize the concentration of the metal-rich anions. As discussed before, for the case of platinum, a stoichiometric factor of 2 has to be applied, i.e. the platinum concentration is only about half of the total anion concentration.

In the simulation, the nanowire is composed of a hemispherical tip and a cylindric shaft. Thus, the solution of the growth equation at the nanowire can be approximated as the superposition of solutions of a spherical geometry (Figure 2.6a on page 15) in the tip region and of a cylindrical setup at the shaft. In the junction of tip and shaft, the solution shows a smooth and monotonous transition between the two one-dimensional extremes. Thus, considering the nanowire growth in a spherical setup is a measure for the length extension of the nanowires. Similarly, the growth velocity in the cylinder setup models the diameter increase of the nanowire shaft.

The nanowire growth velocity for all three considered reaction models (cf. section 2.7.1) depends on the electric field and the concentration of metal-rich anions in the vicinity of the nanowire. However, at a sufficiently high field-activation of the reaction, the nanowire growth velocity is limited by the availability of metal-rich anions at the nanowire surface. Therefore, for any considered reaction model there is an electric field threshold, at which a further increase of the electric field does not significantly enhance the nanowire growth velocity. To estimate the corresponding maximal nanowire growth velocity $v_{\mathrm{w,max}}$, it is assumed that in every AC period all platinum anions with a distance less than the charge transfer length $\ell \approx 1\,\mathrm{nm}$ are reduced

$$v_{\mathrm{w,max}} = c_{\mathrm{a1}}\,\Omega\,\ell\,f. \tag{2.121}$$

Consequently, to yield a nanowire growth velocity in the typical experimental range of 10 nm/s, a total anion concentration of at least $c_2 = 0.22\,\mathrm{mM}$ is required at the nanoelectrode ($r = r_1$). This limit is marked in Figure 2.37 and allows to estimate the electric field threshold E_{t}. Since in the experiments no nanowire growth in either, length or thickness for a sine signal and no thickness growth for the square signal are observed, the electric field threshold is larger than the intersections at $E = -53\,\mathrm{MV/m}$. On the other hand, since for a square signal a nanowire growth in length is found, the electric field

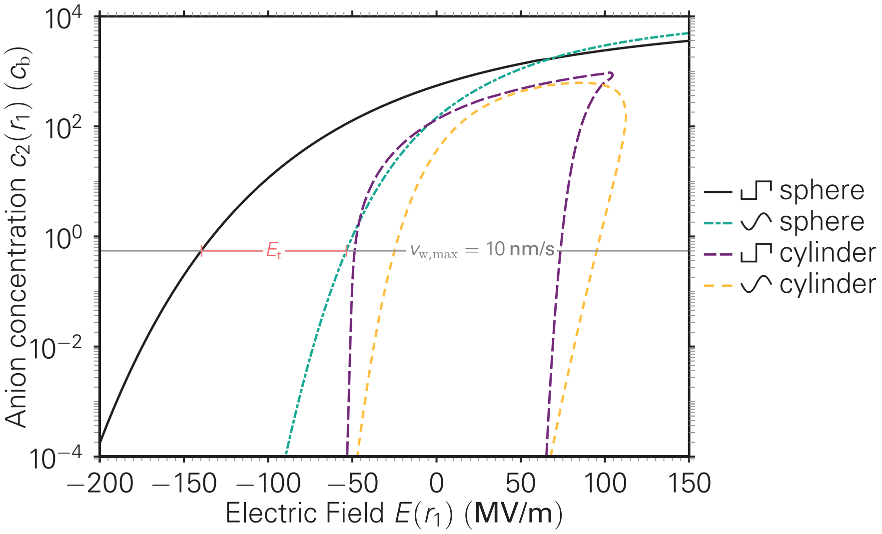

Figure 2.37: Parametric plot of the time-dependent anion concentration versus the corresponding electric field, both at the nanowires surface. As signal shape a sine and a square signal with a finite slope of 8.3×10^7 V/s is used. The minimal anion concentration to enable the experimentally found nanowire growth velocity of 10 nm/s is marked. Based on the fact that the nanowire grows at the tip (approximated by a sphere) for the square signal and not for the three other cases, the possible range for the electric field threshold is deduced (red color). The simulation parameters are $V_\mathrm{RMS} = 7$ V, $c_\mathrm{b} = 0.4$ mM, $f = 1$ MHz, and $r_1 = 20$ nm.

threshold should be smaller than the intersections at $E = -140$ MV/m. For a distinct switching of the nanowire growth velocity, the reaction rate constant should change by several orders of magnitude when increaseing the electric field from $E = -53$ MV/m to $E = -140$ MV/m. The reaction models of field-assisted thermal activation (Equation 2.105) and tunneling current limited platinum reduction (Equation 2.106) yield an increase by a factor of 5.6 and 2.6, respectively, which makes them unsuited. In contrast, the field-induced bond weakening predicts a change of over seven orders of magnitude. A further argument in favor of the bond weakening hypothesis is that the electric field threshold, at which the reaction is enabled, agrees well with the CP2K calculations, cf. Table 2.4. Therefore, in the following, a reaction rate according to Equation 2.109 is employed.

In the next step, the constant of proportionality, k_0, in Equation 2.109 needs to be determined. To this end, the concentration ratio of metal-rich anions by the total amount anions, g, is determined from Equation 2.117 using the boundary condition Equation 2.119 and $g = 0.5$ as mentioned above. The resulting nanowire growth velocity is shown in Figure 2.38 as a function of k_0. In addition to the sine and square signal, the case of $n = 3$ (up to fifth harmonic) is depicted. The corresponding nanowire growth velocity in length is substantially smaller than the one for the square signal, but still more than one order of magnitude larger than for the sine case. Experimental nanowire growth velocities for square signals have a broad scattering and are typically in the order of 10 nm/s. To obtain a comparable growth velocity in the simulation, k_0 is chosen in the range from about 10 nm/s to 1000 nm/s as highlighted in Figure 2.38.

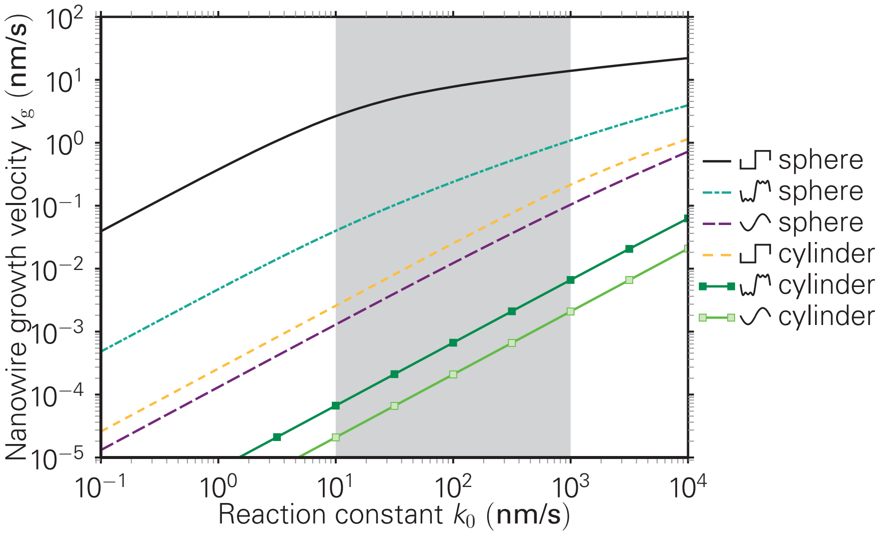

Figure 2.38: Simulated DENA nanowire growth velocity depending on the constant of proportionality k_0. The highlighted region marks the range of k_0, where the rectangular signal yields typical experimental growth velocities.

Using the axially symmetric wire geometry (Figure 2.6b on page 15), the nanowire growth velocity for a square-shaped voltage is simulated. The obtained distribution of the nanowire growth along the wire surface is shown in Figure 2.39. For $k_0 = 10\,\mathrm{nm/s}$ the nanowire growth velocity at the nanowire tip of 13 nm/s is within the expected range. However, the wire growth velocity at the cylindrical wire shaft is only one order of magnitude smaller. Under these circumstances, a growth of thin, straight, and unbranched nanowires as shown in Figure 2.36 is unlikely. At a lower reaction rate of $k_0 = 1\,\mathrm{nm/s}$ the growth velocity at the shaft is strongly reduced, while the growth velocity at the tip is hardly affected. The aspect ratio of growth velocity is larger than 200 : 1, which excellently matches the experimental findings. In the region of transition from tip to shaft the growth velocity drops smoothly. This is due to the smooth progress of the normal electric field along the wire surface.

As mentioned before, the key distinctive feature between the sine wave and rectangular signal shape is the voltage slope at the time of polarity reversal. If it is too low as in the case of a sine signal, by the time a sufficient electric field has build up, the anions have left the proximity of the nanowire. Under these conditions the nanowire cannot grow. The minimal voltage slope to enable the nanowire growth is estimated from a simplified version (no crowding, since $\omega \gg \omega_{\mathrm{T1}}$) of the PNP equations,

$$\frac{\partial c_i}{\partial t} = -\nabla \cdot \mathbf{j}_i \approx D\,\nabla \cdot \left(\nabla c_i + \frac{z_i\, e\, c_i}{k_{\mathrm{B}} T} \nabla \varphi \right) . \tag{2.122}$$

As shown in section 2.5.3, the typical thickness of the double layer is much smaller than the tip radius r_1. Thus, the planar approximation ($\nabla \approx \mathbf{e}_{\mathrm{r}} \frac{\partial}{\partial r}$) holds in the double layer. Moreover, in the absence of field enhancement, the electric field is approximately constant throughout the double layer, i.e. $E(r,t) \approx V(t)/r_1$. To analyze the system behavior

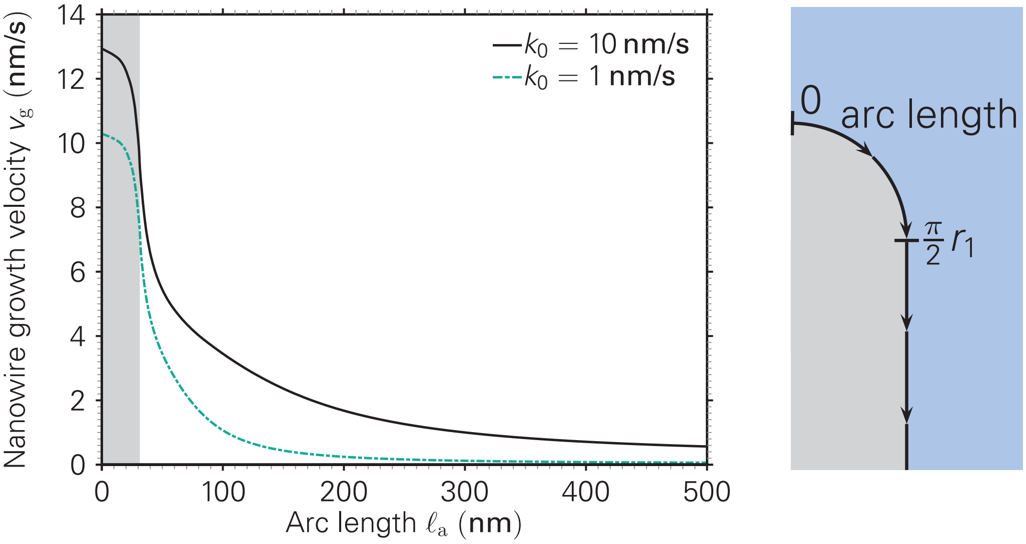

Figure 2.39: Local distribution of the normal nanowire growth velocity of the anion-based DENA mechanism with a rectangular signal shape applied. The tip region of the axially symmetric wire geometry is highlighted. Parameters: $V_{\mathrm{RMS}} = 7\,\mathrm{V}$, $f = 10\,\mathrm{MHz}$, $c_{\mathrm{b}} = 0.1\,\mathrm{mM}$, $r_1 = 20\,\mathrm{nm}$

after the polarity reversal, the electric field step response is considered, i.e. the electric field is immediately switched from zero to the electric field threshold E_{t}. Then, the Fourier transformation of Equation 2.122 after the switching event yields

$$\imath\omega c_i(r,\omega) = D\frac{\partial^2}{\partial r^2} c_i(r,\omega) - \frac{D\,z_i\,e\,E_{\mathrm{t}}}{k_{\mathrm{B}}T}\frac{\partial}{\partial r} c_i(r,\omega). \tag{2.123}$$

Considering the boundary condition $\mathbf{j}_i \cdot \mathbf{n} = 0$ at $r = r_1$, the analytical solution of Equation 2.123 for anions ($z_2 < 0$) is

$$\begin{aligned} c_2(r,\omega) &= \hat{k}_i(\omega)\exp\left((r-r_1)\sqrt{\frac{\omega_{\mathrm{p}}}{D}}\right)\cosh\left((r-r_1)\sqrt{\frac{\imath\omega+\omega_{\mathrm{p}}}{D}}\right), \\ \omega_{\mathrm{p}} &= \frac{D}{4}\left(\frac{z_i e E_{\mathrm{t}}}{k_{\mathrm{B}}T}\right)^2, \end{aligned} \tag{2.124}$$

where $\hat{k}_i(\omega)$ is an integration constant determined by the initial conditions. Based on Equation 2.124, two frequency regimes can be distinguished. At very low frequencies, i.e. $\omega \ll \omega_{\mathrm{p}}$, the long-range anion dislocation sets in, which prohibits the charge transfer from the electrode to the anion and thereby the reduction. Only for a sufficiently high frequency, $\omega \gg \omega_{\mathrm{p}}$, the ions are rearranged merely in the immediate vicinity of the electrode, which still allows the charge transfer. Therefore, to enable the nanowire growth, the electric field threshold should be reached within

$$\Delta t < \mathcal{O}\left(2\pi/\omega_{\mathrm{p}}\right) \tag{2.125}$$

A numerical simulation with the parameters $V_0 = 7\,\mathrm{V}$, $r_1 = 20\,\mathrm{nm}$, and $f = 10\,\mathrm{MHz}$ reveals that an adequate nanowire growth occurs if the electric field threshold is reached within $0.02\,\mathcal{T}$. Assuming an electric field threshold of $E_{\mathrm{t}} = -100\,\mathrm{MV/m}$, which is an

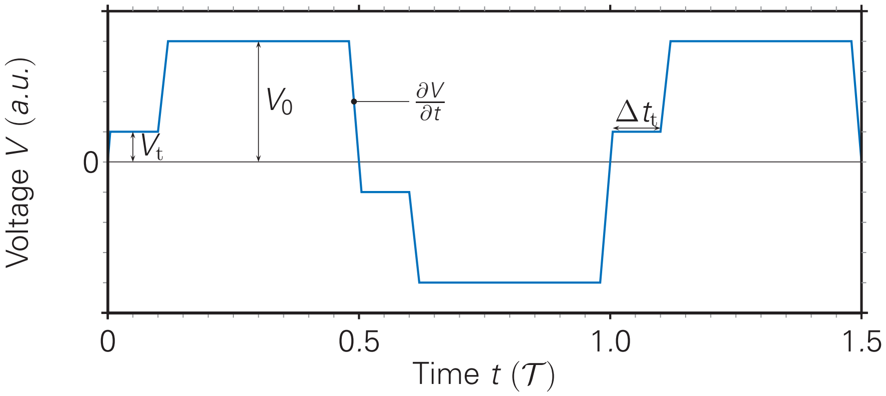

Figure 2.40: Schematic voltage signal for optimized anion-based DENA nanowire growth. The major design parameters are the threshold voltage (V_t), the voltage slope ($\frac{\partial V}{\partial t}$), the period time ($\mathcal{T} = 1/f$) and the voltage amplitude (V_0).

intermediate value within the previously determined interval, Equation 2.125 yields a rise time of less than $0.037\,\mathcal{T}$.

The upper bound for the rise time (Equation 2.125) to enable the nanowire growth in length corresponds to a minimal voltage slope of

$$\frac{\partial |V|}{\partial t} = r_1 \frac{\partial |E|}{\partial t} > r_1 \, |E_\mathrm{t}| \, \frac{\omega_\mathrm{p}}{2\,\pi}. \tag{2.126}$$

However, if a rectangular signal with a large voltage amplitude $V_0 \gg r_1 \, |E_\mathrm{t}|$ and a voltage slope much larger than required by inequality 2.126 is applied, the electric field at the cylinder shaft, which is smaller than the one at the tip, reaches the electric field threshold within the maximum rising time, too, which leads to an undesired thickness growth. Exactly this phenomenon is responsible for the comparatively large growth velocities at the cylinder for $k_0 = 10\,\mathrm{nm/s}$ in Figure 2.39. To prevent this scenario, based on the simulation results, an improved signal shape design is sketched in Figure 2.40. As before, the signal should be anti-periodic in time, $V(t) = -V(t + \mathcal{T}/2)$, to allow for a nanowire growth from both electrodes. At the polarity reversal, the voltage drops from the positive amplitude, V_0, with a sufficiently large slope (cf. Equation 2.126) to the negative of the threshold level

$$V_\mathrm{t} = r_\mathrm{d}\,|E_\mathrm{t}|, \tag{2.127}$$

where r_d is the desired radius of the growing nanowire. The voltage is held at the threshold level until the anions have left the cylindrical nanowire shaft, i.e. for a time period given by

$$\Delta t_\mathrm{t} \gg 2\pi/\omega_\mathrm{p}. \tag{2.128}$$

Afterwards, the voltage reaches its negative amplitude. This construction ensures that the reduction of the platinum anions happens only at nanowire tips with a radius $r_1 \lesssim r_\mathrm{d}$. At larger tips and at the cylinder shaft the electric field threshold is reached only after the hold, which effectively inhibits the nanowire growth at these places. The voltage signal designed in this fashion enables the platinum anion reduction predominantly at the nanowire tip. In order to grow thin nanowires from it, additionally a large supply of platinum ions from the solution to the tip has to be maintained. By adjusting the AC voltage amplitude V_0 and the AC frequency, it is possible to control the total anion concentration, cf. section 2.5. It is recommended to choose a frequency close to the upper transition frequency, since this yields the largest anion displacement in one AC period, which provides the best exchange of metal-free and metal-rich anions. To support the growth of thin and straight nanowires, the ratio of total anion concentration at the nanowire tip to the one at the nanowire shaft should be maximized. Due to the ion crowding, this is achieved when the total anion concentration c_2 barely reaches the maximum concentration c_{max} at the nanowire tip. As shown in section 2.5, the anion concentration amplitude at a given AC frequency is controlled by the AC voltage amplitude of the sine signal. By comparing the RMS voltages of the sine signal and the optimized growth signal, these results can be approximately transferred to chose the voltage amplitude V_0 of the optimized signal.

In summary, for a carefully adjusted voltage signal as sketched in Figure 2.40, the growth of straight nanowires with a predefined thickness is predicted. Growing nanowires with the designed voltage signal is likely to yield even thinner nanowires than the already highly promising result of Ref. [70] with a nanowire diameter of about 15 nm. Moreover, the presented approach can be easily transferred to other stable metallic anions. In this case, only the electric field threshold and possibly the stoichiometric factor need to be adapted.

3 NUMERICAL IMPLEMENTATION

3.1 FOUNDATIONS

3.1.1 Strong and weak forms of partial differential equations

The form, in which PDEs have been presented so far, is known as the strong form. It is characterized by an equation, which involves an unknown function and its derivatives, usually in space and/or time, such as

$$\Xi\left(u(\mathbf{x},t),\frac{\partial}{\partial t}u(\mathbf{x},t),\nabla u(\mathbf{x},t),\nabla^2 u(\mathbf{x},t),\dots\right)=0,\quad \mathbf{x}\in\Omega \tag{3.1}$$

The solution of the PDE needs to fulfill this equation at any point of space, at which this equations is defined, here the domain Ω. In order to arrive at a unique solution, it is required to pose additional boundary conditions, i.e. constraints to the sought function on the entire boundary of Ω, and initial conditions, i.e. the functional values over the entire domain at an initial point of time.

On the other hand, there exists also a weak form of any PDE, whose solution is the same as the one of the strong form it corresponds to. One way to transform a strong from into a weak form is to multiply an implicit strong form like Equation 3.1 with an arbitrary test function $w(\mathbf{x})$ from a Sobolev space and integrate the product over the entire domain

$$\int_\Omega \mathrm{d}V\,\Xi\left(u(\mathbf{x},t),\frac{\partial}{\partial t}u(\mathbf{x},t),\nabla u(\mathbf{x},t),\nabla^2 u(\mathbf{x},t),\dots\right)w(x)=0. \tag{3.2}$$

The resulting equation is fulfilled for any choice of the test function if and only if the strong form is satisfied at any point of space and thus the integrand vanishes over the entire domain.

All PDEs solved in this work are of second-order, i.e. up to second derivatives in space occur. With the help of integration by parts and the application of the divergence theorem, the weak form of these second-order PDEs can be rewritten, such that only up to first-order derivatives of the sought function as well as the test function occur. For example there holds

$$\begin{aligned}\int_\Omega \mathrm{d}V\,(\nabla^2 u(\mathbf{x},t))\,w(\mathbf{x}) &= \int_\Omega \mathrm{d}V\,\nabla\cdot(w(\mathbf{x})\,\nabla u(\mathbf{x},t)) - \int_\Omega \mathrm{d}V\,\nabla u(\mathbf{x},t)\cdot\nabla w(\mathbf{x}),\\ &= \int_{\partial\Omega} \mathrm{d}A\,\mathbf{n}\cdot(w(\mathbf{x})\,\nabla u(\mathbf{x},t)) - \int_\Omega \mathrm{d}V\,\nabla u(\mathbf{x},t)\cdot\nabla w(\mathbf{x}),\end{aligned} \tag{3.3}$$

where **n** is the outward oriented surface normal. The resulting surface integrals can be simplified by substituting with the boundary conditions.

3.1.2 FEM discretization

The finite element method is a numerical tool to solve partial differential equations approximately. To this end, a mesh is defined, which tiles the domain Ω completely into elements. On each of the created subdomains, a set of local ansatz functions is defined. The ansatz functions are described by the nodes of the element. These nodes are special points in the element, at which exactly one local ansatz function is unity and all other local ansatz functions vanish. The numerical solution of the PDE is then expressed as a piecewise superposition of the local ansatz functions. To ensure the continuity of the overall numerical solution, the local ansatz functions of neighboring finite elements are connected over shared nodes on their common edge or vertex.

For the numerical solution of PDEs, their weak form is considered. Then, the ansatz is introduced for the system variable, for example the scalar function u. The approximation of u is fully described by all of its nodal values. Hence, the degrees of freedom equal the number of nodes in the mesh. In general, the approximation of u does not fulfill the weak form for all choices of the test function w. Consequently, with the available degrees of freedom for u, the weak form can be satisfied only for a selection of test functions. Applying Galerkin's method, a basis of test functions is chosen from the same function space as the ansatz for u. Evaluating the integrals in the weak form for each considered test function yields a set of algebraic equations with as many equations as unknowns. Céa's lemma [98] proves that Galerkin's method yields optimal results for the class of elliptic PDEs, to which all PDEs considered in this work belong.

3.2 MESHES AND ANSATZ FUNCTIONS

3.2.1 One-dimensional systems

To get a first impression, the transport of ions, complexes, and metal clusters and the resulting nanowire growth have been studied in an one-dimensional spherically symmetric geometry. Due to the spherical symmetry, all tangential derivatives and vector components vanish exactly. Thus, these calculations allow the investigation of the transport processes and their parameter influence at extremely low computational costs. Other than in a planar, one-dimensional calculation, the curved electrode surface of the spherical geometry preserves major features of the numerical solution in the vicinity of the nanowire tip.

In one-dimensional systems, the domain is a line segment and the boundary conditions are applied to its end points. The element tiling of the domain should reflect the local length scales of the solution. Since the gradients of the electric and chemical potential are particularly steep at the electrodes, a very fine element resolution is required there. On the other hand, for the bulk region far from the electrodes, where little spatial and temporal changes in the system variables occur (cf. section 2.5.2), a much larger element size is sufficient. To this end, the line segment of length ℓ is subdivided into N_x smaller line segments according to two geometric sequences

$$x_k = r_1 + \begin{cases} \frac{\ell(q^k-1)}{2(q^{N_\mathrm{x}/2}-1)}, & 0 \leq k \leq N_\mathrm{x}/2 \\ \ell - \frac{\ell(q^{N_\mathrm{x}-k}-1)}{2(q^{N_\mathrm{x}/2}-1)}, & N_\mathrm{x}/2 < k \leq N_\mathrm{x} \end{cases}, \tag{3.4a}$$

$$q = \left(\frac{\ell_\mathrm{max}}{\ell_\mathrm{min}}\right)^{2/N_\mathrm{x}}. \tag{3.4b}$$

Each finite element is then the line segment between two neighboring x_k. For the mesh generation a ratio of largest to smallest element of $\frac{\ell_\mathrm{max}}{\ell_\mathrm{min}} = 5000$ and $N_\mathrm{x} = 512$ is used. This construction and parametrization ensures a smooth transition between the sub-angstrom resolution near the electrode and coarser elements of up to a few ten nanometers in length in the bulk zone.

As element type a linear 3-node element with a quadratic ansatz function is chosen. In local coordinates $\xi \in [0, 1]$ the ansatz with the nodal values u_i is given by

$$u\,(\xi) := u_0\ (2\,\xi - 1)\ (\xi - 1) + 4\,u_1\ (1 - \xi)\ \xi + u_2\,\xi\ (2\,\xi - 1) \tag{3.5}$$

The integration of the weak form is performed numerically using Gauss-Legendre quadrature with three integration points. The integration of a function $\Xi(x)$ over the ith element then becomes

$$\begin{aligned} \int_{x_i}^{x_{i+1}} \mathrm{d}x\,\Xi(x) &= (x_{i+1} - x_i) \int_0^1 \mathrm{d}\xi\,\Xi\,(x_{i+1}\,\xi + x_i\,(1 - \xi)) \\ &=: (x_{i+1} - x_i) \int_0^1 \mathrm{d}\xi\,\hat{\Xi}(\xi) \\ &\approx \frac{x_{i+1} - x_i}{2} \left[\frac{5}{9}\,\hat{\Xi}\left(\frac{1}{2} - \sqrt{\frac{3}{20}}\right) + \frac{8}{9}\,\hat{\Xi}\left(\frac{1}{2}\right) + \frac{5}{9}\,\hat{\Xi}\left(\frac{1}{2} - \sqrt{\frac{3}{20}}\right)\right] \end{aligned} \tag{3.6}$$

This scheme allows to integrate a polynomial of up to 5th-order exactly. Employing a quadratic ansatz function, the discretization of a linear PDE yields a fourth-oder polynomial as integrand of the weak form. In addition, due to the spherically symmetric geometry, the integral over the domain volume $\mathrm{d}V = \mathrm{d}x\,4\,\pi\,x^2$ further increases the polynomial order. However, due to the fine element tiling ($x_{k+1} - x_k \ll x_k$), the change of x^2 over one element is extremely small, such that a linear approximation has a negligible error. Therefore, all occurring integrals of the weak form of a linear PDEs are calculated with quasi-analytic precision.

3.2.2 Axisymmetric, two-dimensional systems

As introduced in section 2.2 on page 12, the axisymmetric nanowire geometry is modeled by a hemisphere connected to a cylinder. This simplified nanowire is embedded concentrically in a cylinder of solution, whose radius and axis length is several orders of magnitude larger than the wire diameter. This geometry represents a good compromise between geometric accuracy and numerical effort.

To study the geometry dependence of the nanowire growth, three different domain shapes, one with a nanowire radius of 20 nm and two with 50 nm, were meshed using the software COMSOL® , version 4.3. Operating the incorporated geometry design tool, the radial cross section of the geometry was sketched. Afterwards the method *Free Triangular* was applied to generate the mesh. With the help of the *Size* feature, the geometric properties of the overall mesh, including adaptations at the nanowire surface and as required also at the counter electrode, were adjusted, cf. Table 3.1. The tailoring of these meshes ensures a fine resolution in the sub-nanometer range close to the electrodes and a much coarser resolution in the bulk region of up to 130 nm and 100 nm length, respectively. Since smaller curvature radii result in larger electric fields, which in turn lead to steeper concentration gradients, the minimum elements size of mesh I needs to be significantly smaller than for meshes II and III.

For the FEM calculations 6-node triangle elements were utilized. In local coordinates, $\xi \geq 0, \eta \geq 0, \xi + \eta \leq 1$, the ansatz functions are defined as

$$\begin{aligned} u(\xi,\eta) =& u_{0,0}\,(\xi+\eta-1)(2\xi+2\eta-1) - 4\,u_{1,0}\,\xi(\xi+\eta-1) + u_{2,0}\,\xi(2\xi-1) \\ & - 4\,u_{0,1}\,\eta(\xi+\eta-1) + 4\,u_{1,1}\,\xi\eta + u_{0,2}\,\eta(2\eta-1). \end{aligned} \tag{3.7}$$

Similarly to the one-dimensional case, the integrals of the weak form are approximated with a quadrature formula. In the literature [99], a nonlinear coordinate transformation exists, which allows the application of the Gauss-Legendre quadrature of rectangles to triangles as well. Additionally, Pan [100] proposed an improvement, which also includes local derivatives in the calculation. Despite the good numerical approximation of the occurring integrals, these formulas have the crucial drawback that the value of the quadrature depends on the orientation of the triangle. Due to the automated mesh generation by COMSOL® , the orientation of the triangles in the mesh is–to some extent–arbitrary, which bears the threat of introducing additional numerical artifacts.

To avoid such artifacts, a quadrature for triangles was implemented based on Romberg's method. The key idea is to start with a simple integration scheme, in this case

$$\int_{\Omega_i} \mathrm{d}A_i\, u(\xi,\eta) = \frac{A_i}{3}\left[u(0,0) + u(1,0) + u(0,1)\right] + A_i\,\mathcal{O}(h^2), \tag{3.8}$$

where A_i is the area of the ith element and h is a typical length scale of it. Then, the triangles are recursively subdivided into four congruent triangles as shown in Figure 3.1. Applying the quadrature formula to all subtriangles gives a slightly different estimation of the total integral. As the subtriangles area is only one fourth of the original triangle, the leading term of quadrature error, $A_i\,\mathcal{O}(h^2)$ in the initial formula, is also one fourth. A linear

Table 3.1: Parameters of the *Size* objects used to create the *Free Triangular* mesh. Additionally statistics on the resulting mesh are provided. Mesh I has two types of superseded edges with different maximum element sizes.

Mesh No:	I	II	III
r_1	20 nm	50 nm	50 nm
h	0.85 µm	0.85 µm	1.7 µm
a	3 µm	3 µm	6 µm
Maximum element size	0.135 µm	0.1 µm	0.1 µm
Minimum element size	0.06 µm	0.06 µm	0.06 µm
Maximum element growth rate	1.15	1.135	1.135
Resolution of curvature	0.3	0.3	0.3
Resolution of narrow regions	1	1	1
superseded edges	NW surface / counter electrode	NW surface	NW surface
Maximum element size	0.5 nm / 2 nm	1 nm	1 nm
Minimum element size	0.05 nm	0.2 nm	0.2 nm
Maximum element growth rate	1.3	1.3	1.3
Resolution of curvature	0.001	0.001	0.001
triangles	101785	38394	70495
nodes	207722	78255	143464
maximum element area	9100 nm^2	5400 nm^2	5300 nm^2
average element area	88.2 nm^2	233 nm^2	509 nm^2
median element area	0.68 nm^2	0.53 nm^2	0.80 nm^2
minimum element area	0.000 75 nm^2	0.012 nm^2	0.012 nm^2

combination of both results can be used to cancel the leading error term. The emerging quadrature is then given by

$$\int_{\Omega_i} \mathrm{d}A_i \, u(\xi,\eta) = A_i \left[u\left(0, \frac{1}{2}\right) + u\left(\frac{1}{2}, 0\right) + u\left(\frac{1}{2}, \frac{1}{2}\right) \right] / 3 + A_i \mathcal{O}(h^3). \tag{3.9}$$

Usually, the number of quadrature points increases due to application of Romberg's method. For the first iteration, however, the weights for the points $\{(0,0),(1,0),(0,1)\}$ cancel, so that the total number remains 3. A recursive application produces better ap-

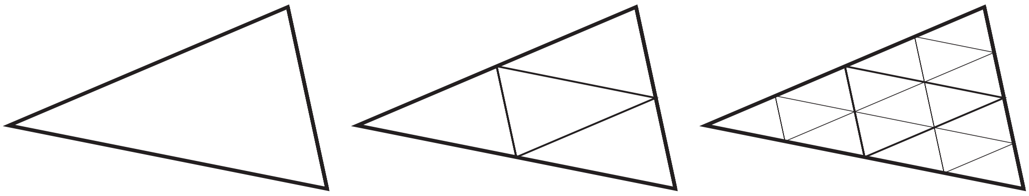

Figure 3.1: Recursive subdivision of triangle elements used to improve the quadrature according to Romberg's method

proximation of the integral at the expense of increasing the number of quadrature points. In this work, the output of the second iteration,

$$\begin{aligned}\int_{\Omega_i} \mathrm{d}A_i\, u(\xi,\eta) = \frac{A_i}{45}\Bigg[&4\,u\left(\frac{3}{4},\frac{1}{4}\right) + 4\,u\left(\frac{3}{4},0\right) - u\left(\frac{1}{2},\frac{1}{2}\right) + 8\,u\left(\frac{1}{2},\frac{1}{4}\right)\\ &-u\left(\frac{1}{2},0\right) + 4\,u\left(\frac{1}{4},\frac{3}{4}\right) + 8\,u\left(\frac{1}{4},\frac{1}{2}\right) + 8\,u\left(\frac{1}{4},\frac{1}{4}\right)\\ &+4\,u\left(\frac{1}{4},0\right) + 4\,u\left(0,\frac{3}{4}\right) - u\left(0,\frac{1}{2}\right) + 4\,u\left(0,\frac{1}{4}\right)\Bigg]\\ &+A_i\,\mathcal{O}(h^5),\end{aligned} \tag{3.10}$$

is used. This choice is a compromise between accuracy and computation time, the latter of which increases fast with the recursion number. By construction, all recursion steps of this quadrature formula are invariant over a permutation of the triangle vertices.

As quadrature algorithm for quadrilateral elements the Gauss-Legendre formula with 3 × 3 quadrature points is used, which results from a sequential application of Equation 3.6 for ξ and η.

3.2.3 NURBS enhanced FEM

Compared to the solution of the Poisson–Nernst–Planck equation, the dielectrophoretic transport of metal clusters or complexes shows a much larger length scale on the order of 100 nm. Consequently, a significantly coarser FEM mesh can be used for these simulations. Thereby, the numerical solution of the PDE system speeds up drastically without causing noticeable negative consequence for the accuracy. However, employing a coarse, polygonal mesh leads to a highly inaccurate representation of the geometry. To exploit the advantages of a coarse mesh nevertheless, an element type with curved edges is introduced. The geometry of these elements is described by non-uniform rational B-splines (NURBS), a generalization of B-splines and Bézier curves. An FEM scheme relying on this type of finite elements is called a NURBS enhanced FEM or shortly NEFEM.

In this work, the NEFEM mesh is assembled from curved, quadrilateral NURBS-elements and regular triangular elements. Both element types are mapped on their respective orthonormal standard element, cf. Figure 3.2. In the local coordinates of the standard element (ξ,η), the ansatz function u as well as the mapping to the real space $\mathbf{x}$ is defined. For the regular triangles this becomes

$$\mathbf{x}(\xi,\eta) = \mathbf{x}_0(1-\xi-\eta) + \mathbf{x}_1\,\xi + \mathbf{x}_2\,\eta, \tag{3.11a}$$

$$u(\xi,\eta) = \sum_{i=0}^{3}\sum_{k=0}^{3-i} u_{ik}\binom{3}{i}\binom{3-i}{k}\,\xi^i\,\eta^k\,(1-\xi-\eta)^{3-i-k}, \tag{3.11b}$$

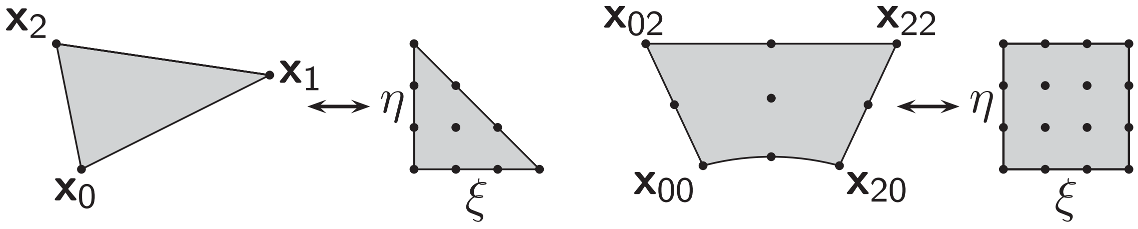

Figure 3.2: Mapping of triangles and curved quadrilateral elements to standard elements. On the standard elements a bicubic ansatz function is defined (cf. Equations 3.11 and 3.12) and the corresponding nodes are shown.

and for the NURBS based quadrilaterals they are

$$\mathbf{x}(\xi,\eta) = \frac{\sum\limits_{i,k} \mathbf{x}_{ik}\, w_{ik} \binom{2}{i} \xi^i \, (1-\xi)^{2-i} \, \binom{2}{k} \eta^k \, (1-\eta)^{2-k}}{\sum\limits_{i,k} w_{ik} \binom{2}{i} \xi^i \, (1-\xi)^{2-i} \, \binom{2}{k} \eta^k \, (1-\eta)^{2-k}}, \tag{3.12a}$$

$$u(\xi,\eta) = \sum_{i=0}^{3}\sum_{k=0}^{3} u_{ik} \binom{3}{i} \xi^i \, (1-\xi)^{3-i} \binom{3}{k} \eta^k \, (1-\eta)^{3-k}\,. \tag{3.12b}$$

A combination of curved and regular, i.e. non-curved, finite elements is used to reduce the computation time. The mapping of curved elements, in particular the evaluation of derivatives in global coordinates is computationally rather expensive and should therefore be reduced to a minimum.

The numerical integration in regular triangle elements is described in the previous section. However, due to using cubic polynomials as ansatz functions, the presented numerical quadrature has proven insufficient. As it turns out, the quadrature formula using the next recursion step of Romberg's method is computationally more expensive than an analytical integration. Therefore, for the NEFEM method the integration is implemented as

$$\int_0^1 \mathrm{d}\xi \int_0^{1-\xi} \mathrm{d}\eta\, \xi^k\, \eta^l = \frac{k!\; l!}{(k+l+2)!}. \tag{3.13}$$

The integral over the quadrilateral elements is transformed to the standard elements using the mapping relation

$$\int_{\Omega_i} \mathrm{d}\mathbf{x}\, \hat{f}(\mathbf{x}) = \int_0^1 \mathrm{d}\xi \int_0^1 \mathrm{d}\eta\, f(\xi,\eta) \left| \begin{pmatrix} \frac{\partial \mathbf{x}}{\partial \xi} & \frac{\partial \mathbf{x}}{\partial \eta} \end{pmatrix} \right| . \tag{3.14}$$

The subsequent quadrature of Equation 3.14 employs the Gauss-Legendre-scheme with 4 × 4 integration points.

Due to the high element ansatz order and the geometrically smooth boundary representation a very coarse mesh, depicted in Figure 3.3, is sufficient to calculate the fluid flow and hydrodynamic pressure, which result from the dielectrophoretic force on metal clusters or complexes in the solution, cf. section 2.3. This is verified by applying the obtained results, visualized in Figure 2.12, to the strong form, which gives only a very small relative residue. It should be emphasized once more that for the ion transport simulations

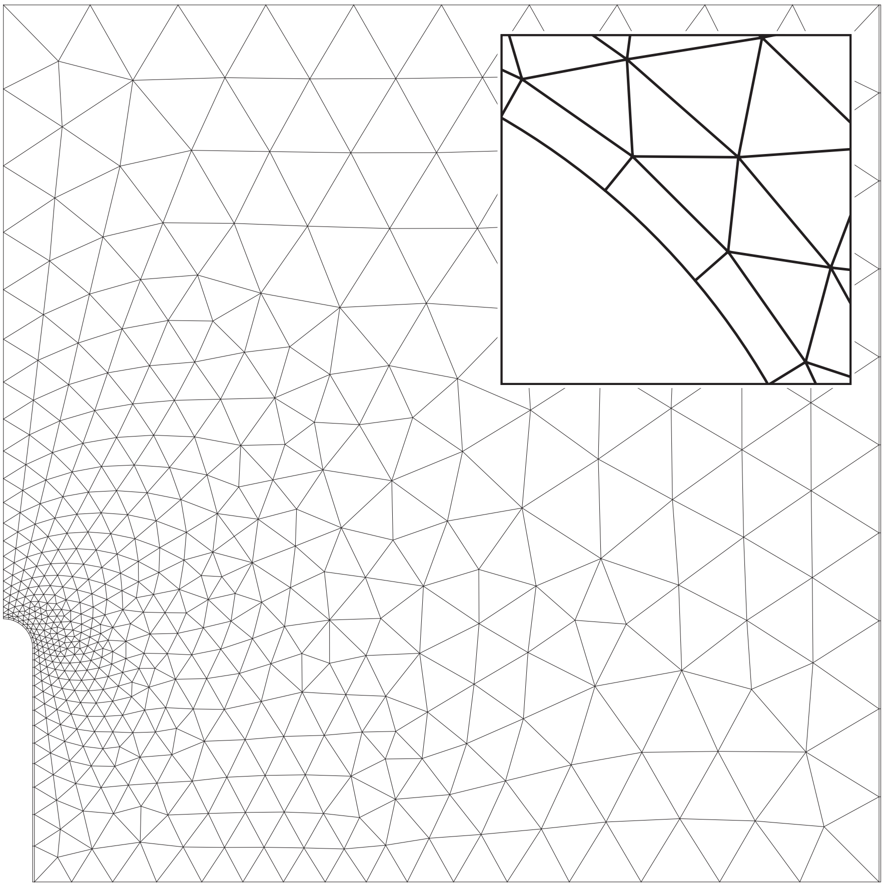

Figure 3.3: The NEFEM mesh used to calculate a fluid flow induced by the dielectrophoretic force of clusters and complexes. The mesh consists of regular triangle elements and NURBS enhanced quadrilateral elements, which allow for an geometric exact representation of the semi-spherical nanowire tip, cf. inset.

and the fluid flow computation based thereon, cf. section 2.5, the NEFEM approach is not suitable. Due to the large convective terms in the transport equation (Equation 2.95), large concentration peaks are accumulated at the electrode tip and consecutively moved up to a few hundred nanometers through the aqueous solution before they are leveled by diffusion. To capture the steep gradients of these peaks a high resolution mesh, in a broad strip around the nanowire is required. For the small element sizes, however, the curvature effects of the nanowire boundary become negligible. Under these circumstances a mesh with just regular, triangular elements is more performant.

3.3 NUMERICAL IMPLEMENTATION OF THE EMPLOYED MODEL PDES

A summary of the model PDEs and the corresponding boundary conditions is given in section 2.6 on page 45 seqq. As described in section 3.1.1, the model PDEs in strong form are transformed into weak form with consideration of the respective boundary conditions.

$$\int_\Omega \mathrm{d}V \left(w_{c_i} \frac{\partial c_i}{\partial t} + c_i \nabla w_{c_i} \cdot \left[\frac{D}{k_\mathrm{B} T} \nabla \left(\mu_i + z_i \, e \, \varphi \right) - \mathbf{v} \right] \right) = 0 \tag{3.15a}$$

$$\int_\Omega \mathrm{d}V \left(-\frac{F}{\varepsilon} \, w_\varphi \sum_i z_i \, c_i + \nabla w_\varphi \cdot \nabla \varphi \right) = 0 \tag{3.15b}$$

$$\int_\Omega \mathrm{d}V \left(w_{v_i} \left[\rho_\mathrm{m} \frac{\partial v_i}{\partial t} + \rho_\mathrm{m} \left(\mathbf{v} \cdot \nabla \right) v_i + \frac{\partial p}{\partial x_i} + \rho \, \frac{\partial \varphi}{\partial x_i} \right] + \eta \, \nabla w_{v_i} \cdot \nabla v_i \right) = 0 \tag{3.15c}$$

$$\int_\Omega \mathrm{d}V \, \nabla w_p \cdot \mathbf{v} = 0 \tag{3.15d}$$

In order to ensure a well-conditioned equation system and as preparation for a later numerical implementation, all system variables and weak form integrands are normalized. The choices for the normalization are the wire radius r_1 as length unit, the simulation time step τ as time unit, and $c_\mathrm{b} \, F \, k_\mathrm{B} T / e$ as energy density unit.

$$\mu_i' = \mu_i / (k_\mathrm{B} T) \tag{3.16a}$$

$$\varphi' = e \, \varphi / (k_\mathrm{B} T) \tag{3.16b}$$

$$c_i' = c_i / c_\mathrm{b} \tag{3.16c}$$

$$\mathbf{x}' = \mathbf{x} / r_1 \tag{3.16d}$$

$$v_i' = v_i \sqrt{\frac{e \, \rho_\mathrm{m}}{c_\mathrm{b} \, F \, k_\mathrm{B} T}} \tag{3.16e}$$

$$p' = p \, e / (c_\mathrm{b} \, F \, k_\mathrm{B} T) \tag{3.16f}$$

$$t' = t / \tau \tag{3.16g}$$

Additionally, for notational convenience, various combinations of physical constants and model parameters are introduced as follows:

$$\beta = \frac{\varepsilon \, k_\mathrm{B} T}{r_1^2 \, c_\mathrm{b} \, F \, e} \tag{3.17a}$$

$$\gamma = \frac{D \, \tau}{r_1^2} \tag{3.17b}$$

$$\chi = \frac{\tau}{r_1} \sqrt{\frac{c_\mathrm{b} \, F \, k_\mathrm{B} T}{e \, \rho_\mathrm{m}}} \tag{3.17c}$$

$$\kappa = \frac{\tau \, \eta}{r_1^2 \, \rho_\mathrm{m}} \tag{3.17d}$$

$$c_i = \frac{\exp(\mu_i)}{1 + a \sum_k \exp(\mu_k)} \tag{3.17e}$$

$$c_{ik} = \frac{\partial c_i}{\partial \mu_k} \tag{3.17f}$$

$$c_{ikl} = \frac{\partial^2 c_i}{\partial \mu_k \partial \mu_l} \tag{3.17g}$$

$$\blacksquare_{,i} = \frac{\partial \blacksquare}{\partial x_i} = \mathrm{e}_i \cdot \nabla \blacksquare \tag{3.17h}$$

It can be shown, that the indices of c_{ik} and c_{ikl} are interchangeable, which is used in the following simplifications. Unless specified otherwise, in the further usage only normalized variables are discussed and the prime notation in Equation 3.16 is dropped in the following. Rewriting and scaling the weak form equations yields

$$\int_\Omega \mathrm{d}V \left(w_{c_i} \frac{\partial c_i}{\partial t} + c_i \nabla w_{c_i} \cdot \left[\gamma \, \nabla \left(\mu_i + z_i \, \varphi \right) - \chi \, \mathbf{v} \right] \right) = 0, \tag{3.18a}$$

$$\int_\Omega \mathrm{d}V \left(-w_\varphi \sum_i z_i \, c_i + \beta \, \nabla w_\varphi \cdot \nabla \varphi \right) = 0, \tag{3.18b}$$

$$\int_\Omega \mathrm{d}V \left(w_{v_i} \left[\frac{\partial v_i}{\partial t} + \chi \, \left(\mathbf{v} \cdot \nabla \right) v_i + \chi \, p_{,i} + \chi \sum_k z_k \, c_k \, \varphi_{,i} \right] + \kappa \, \nabla w_{v_i} \cdot \nabla v_i \right) = 0, \tag{3.18c}$$

$$\int_\Omega \mathrm{d}V \, \chi \, \nabla w_p \cdot \mathbf{v} = 0. \tag{3.18d}$$

After the spatial discretization of the weak form (cf. section 3.1.2) the PDE system, Equation 3.18, has become a large set of ODE, where each nodal value is an unknown function in time. For a broad overview over numerical solution techniques of such initial-value problems, the reader is referred to a large variety of textbooks [101, 102]. Due to the highly stiff nature of the ODE system, a single-step approach to time-integration was used in this work. Explicit methods like forward Euler or higher-order explicit Runge-Kutta schemes cause large oscillations over space and time [103] and are therefore inappropriate for this purpose. Hence, a time integration according to the trapezoidal rule has been implemented. To this end, an explicit first-order ODE is numerically approximated according to

$$\frac{\mathrm{d}u}{\mathrm{d}t} = h(u,t) \quad \rightarrow \quad \frac{u^{n+1} - u^{n}}{\tau} = \frac{h(u^{n+1}, t^{n+1}) + h(u^{n}, t^{n})}{2}, \tag{3.19}$$

where the superindex n denotes the respective variable at the nth discrete time step. This implicit time-integrator has an integration error in the order of $\mathcal{O}(\tau^2)$ and showed satisfactory results in most cases. However, it was found that under extreme conditions (e.g. if the migration contributions to the total ion flux exceeds the one of the diffusion flux by far), the numerical solution starts oscillating. In contrast to the aforementioned explicit integrators, the amplitude of the occurring oscillations is bound. Nevertheless, this is a severe artifact of the numerical solution, which undermines all numerical benefits from the higher convergence order. Therefore, a backward Euler scheme was chosen

$$\frac{\mathrm{d}u}{\mathrm{d}t} = h(u,t) \quad \rightarrow \quad \frac{u^{n+1} - u^{n}}{\tau} = h(u^{n+1}, t^{n+1}), \tag{3.20}$$

which is known for its high robustness [104].

Equations 3.18a–3.18c depend nonlinearly on the system variables. Thus, the equation system resulting from time-integration (Equation 3.20) is nonlinear as well and thereby inappropriate for a direct solution by means of linear algebra. Instead, Newton's method is employed to solve for the system variables at the end of the current time step.

To solve the implicit, nonlinear equation for a model variable, e.g. u, an estimation of the future function value $\widehat{u}^{n+1}$ is required. In this work, the initial estimation is obtained from a cubic extrapolation of the 4 most recent function values of each variable at each node. The estimated function value differs by the prediction error δu from the true future function value u^{n+1}, i.e.

$$u^{n+1} = \widehat{u}^{n+1} + \delta u. \tag{3.21}$$

To retrieve this future value, the residue of inserting $\widehat{u}^{n+1}$ to Equation 3.20 is linearly expanded in terms of the prediction error δu. The solution of the resulting *linear* equation (system) is used to improve the estimated future function value, cf. Equation 3.21. This procedure is repeated until the residue is below the error threshold. Applying to Equation 3.18 the procedure as described, yields the iteration equations for the weak forms of the model PDEs

$$\begin{aligned}
&\int_\Omega \mathrm{d}V \left(w_{c_i} \sum_{kl} \hat{c}_{ikl}^{n+1} \left\{ \hat{\mu}_k^{n+1} - \mu_k^n \right\} \delta\mu_l \; + \hat{c}_i^{n+1} \nabla w_{c_i} \cdot \left[\gamma \nabla \left(\delta\mu_i + z_i \, \delta\varphi \right) - \chi \, \delta\mathbf{v} \right] \right. \\
&\left. + \sum_k \hat{c}_{ik}^{n+1} \left[w_{c_i} + \nabla w_{c_i} \cdot \left\{ \gamma \nabla \left(\hat{\mu}_i^{n+1} + z_i \, \hat{\varphi}^{n+1} \right) - \chi \, \widehat{\mathbf{v}}^{n+1} \right\} \right] \delta\mu_k \right) = \\
&- \int_\Omega \mathrm{d}V \left(w_{c_i} \sum_k \hat{c}_{ik}^{n+1} \left[\hat{\mu}_k^{n+1} - \mu_k^n \right] \right. \\
&\left. + \hat{c}_i^{n+1} \nabla w_{c_i} \cdot \left[\gamma \nabla \left(\hat{\mu}_i^{n+1} + z_i \, \hat{\varphi}^{n+1} \right) - \chi \, \widehat{\mathbf{v}}^{n+1} \right] \right),
\end{aligned} \tag{3.22a}$$

$$\begin{aligned}
&\int_\Omega \mathrm{d}V \left(-w_\varphi \sum_{ik} z_i \, \hat{c}_{ik}^{n+1} \delta\mu_k + \beta \nabla w_\varphi \cdot \nabla \delta\varphi \right) = \\
&\int_\Omega \mathrm{d}V \left(w_\varphi \sum_i z_i \, \hat{c}_i^{n+1} - \beta \nabla w_\varphi \cdot \nabla \hat{\varphi}^{n+1} \right),
\end{aligned} \tag{3.22b}$$

$$\begin{aligned}
&\int_\Omega \mathrm{d}V \left(\kappa \nabla w_{v_i} \cdot \nabla \delta v_i + w_{v_i} \left[\delta v_i + \chi \left(\widehat{\mathbf{v}}^{n+1} \cdot \nabla \right) \delta v_i + \right. \right. \\
&\left. \left. \chi \left(\delta\mathbf{v} \cdot \nabla \right) \hat{v}_i^{n+1} + \chi \, \delta p_{,i} + \chi \sum_k z_k \, \hat{c}_k^{n+1} \, \delta\varphi_{,i} + \chi \sum_{kl} z_k \, \hat{c}_{kl}^{n+1} \, \hat{\varphi}_{,i}^{n+1} \, \delta\mu_l \right] \right) = \\
&- \int_\Omega \mathrm{d}V \left(w_{v_i} \left[\hat{v}_i^{n+1} - v_i^n + \chi \left(\widehat{\mathbf{v}}^{n+1} \cdot \nabla \right) \hat{v}_i^{n+1} + \chi \hat{p}_{,i}^{n+1} \right. \right. \\
&\left. \left. + \chi \sum_k z_k \, \hat{c}_k^{n+1} \, \hat{\varphi}_{,i}^{n+1} \right] + \kappa \nabla w_{v_i} \cdot \nabla \hat{v}_i^{n+1} \right),
\end{aligned} \tag{3.22c}$$

$$\int_\Omega \mathrm{d}V \, \chi \nabla w_p \cdot \delta\mathbf{v} = - \int_\Omega \mathrm{d}V \, \chi \nabla w_p \cdot \widehat{\mathbf{v}}^{n+1}. \tag{3.22d}$$

In the linearized weak form, Equations 3.22, all known terms are collected on the right-hand-side of the equations. The left-hand-side depends linearly on the prediction error, for which the equation system is solved. After the Newton iteration converged, the future value is accepted as current value and the next time step is treated.

3.4 CONVERGENCE ACCELERATION

The PNP equations are an exceptionally stiff PDE system, particularly for large applied electric fields. This implies that in order to solve an initial value problem with the scheme described in section 3.3, many oscillation periods have to be calculated to obtain the asymptotic periodic solution. Especially at intermediate frequencies $\omega_{\mathrm{T1}} \ll \omega \ll \omega_{\mathrm{T2}}$, the amount of necessary time-steps per period is particularly high.

Generally, a direct solution for the asymptotic periodic problem is possible. This requires to consider all time steps of one period in one equation system and pose periodic boundary conditions for the first and the last time step within the period time. This approach increases the size of the equation system dramatically, even when a coarse time discretization is applied. Even worse, the resulting equation system is much more stiff and the matrix associated to it is less sparse. As a consequence, the resulting iteration scheme has an extremely low convergence rate and a particularly small convergence radius. This means, a direct solution for the asymptotic periodic state of the PNP equations is computationally unfeasible.

The convergence acceleration is a new methodology to efficiently retrieve the asymptotic periodic solution of the PNP equations. The physical solution to this problem is unique and attractive, which means that all initial conditions converge towards the same asymptotic solution. Thus, the task to find the asymptotic periodic solution is equivalent to searching for an initial condition, which is reobtained after one time period has passed. The first initial condition is chosen as $c_1(r) = c_2(r) = c_{\mathrm{b}}$. Notably, no time derivatives of the electric potential occur in the Poisson–Nernst–Planck equation and hence no initial condition for φ is needed. Based on the present initial condition, the time-evolution over one half period is simulated. If the considered initial condition equals the initial condition of the asymptotic periodic solution, the time-symmetry property applies (cf. Equation 2.46 on page 29)

$$c_1(r, t) = c_2(r, t - \mathcal{T}/2), \tag{3.23a}$$

$$\varphi(r, t) = -\varphi(r, t - \mathcal{T}/2). \tag{3.23b}$$

Otherwise, the next generation of initial conditions are determined as an averaging according to

$$\hat{c}_1(r, 0) = [c_1(r, 0) + c_2(r, \mathcal{T}/2)]/2 \tag{3.24a}$$

$$\hat{c}_2(r, 0) = [c_2(r, 0) + c_1(r, \mathcal{T}/2)]/2 \tag{3.24b}$$

Usually, the deviations from the asymptotic periodic solution exhibit different signs for the initial and final concentration profiles. Thus, by averaging them, the errors cancel out partially and a fast-converging sequence of initial conditions is obtained.

An improved convergence acceleration applies a continuous averaging, i.e. after each time step performed according to section 3.3, the updated concentration is modified with a simulation result from the past. With $N = \mathcal{T}/(2\,\tau)$ as the number of time steps in a half period, the improved convergence acceleration for each time step is given by

$$\hat{c}_1^n = \left(1 - 2^{-N}\right) c_1^n + 2^{-N} c_2^{n-N}, \tag{3.25a}$$

$$\hat{c}_2^n = \left(1 - 2^{-N}\right) c_2^n + 2^{-N} c_1^{n-N}. \tag{3.25b}$$

For concentrations with a negative superindex the uniform ion concentration $c_i(r) = c_\mathrm{b}$ is used. Since the time-evolution of the PNP equations is calculated in terms of the chemical potentials μ_i, before/after each time step a conversion from/to the concentration domain is needed. The iteration is terminated when the convergence criteria

$$\frac{\left|c_1^k - c_2^{k-N}\right|}{c_1^k + c_2^{k-N} + 10^{-3} c_\mathrm{b}} \leq 1\,\%, \quad \frac{\left|c_2^k - c_1^{k-N}\right|}{c_2^k + c_1^{k-N} + 10^{-3} c_\mathrm{b}} \leq 1\,\% \tag{3.26}$$

is fulfilled for the past N time steps in the entire simulation domain.

For the simulation parameters used in this work, convergence is typically achieved within the first ten oscillation periods. In summary, the convergence acceleration as developed in this work enables the fast and efficient solution of the extremely stiff PNP equations.

4 DISCUSSION AND CONCLUSIONS

Summary

The goal of this thesis was to model and simulate the electric field-assisted nanowire growth from aqueous solutions. By comparison with related experimental studies, it was possible to unveil the underlying principles of the nanowire growth mechanisms. This knowledge is essential to improve the protocols of nanowire growth such that the application requirements of straight, thin and unbranched nanowires can be met. In this work, two different technologies of nanowire fabrication have been considered: first, the dielectrophoretic nanowire assembly (DEP) from uncharged chemical complexes or metal clusters and second, the directed electrochemical nanowire assembly (DENA).

For the dielectrophoretic nanowire growth, an aged K_2PtCl_4-solution is considered as the precursor. During the aging-process the $[PtCl_4]^{2-}$-ions undergo a hydrolysis, in which chloride ligands are replaced by water. The ligand exchange is accompanied by a change of the overall complex charge. In this manner, particularly for small precursor concentrations, a solution with $cis-PtCl_2(H_2O)_2$ as the dominant platinum agent is obtained. This platinum complex is an electrically neutral dipole and is therefore subject to the dielectrophoretic force. An experimental analysis of such solutions revealed additionally the presence of platinum clusters [21].

The nanowire growth was simulated using a model that incorporates diffusion and migration due to the dielectrophoretic force. The obtained predictions regarding the nanowire growth velocity and morphology are compared to an experimental study by A. Nerowski [21], in which nanowires were grown from aged K_2PtCl_4-solutions at various temperatures and for different precursor concentrations. From the analysis it is found that for high temperatures the nanowire growth is transport-limited, whereas for low temperatures a reaction limitation is observed. Overall, this model shows merely a qualitative agreement with the high-temperature experimental results. It is concluded that an additional transport mechanism acts on the complexes and/or clusters.

Through additional modeling and simulations, a fluid flow caused by the dielectrophoretic force could be ruled out as a candidate for this additional transport. Therefore, an alternative model that includes an AC electro-osmotic (ACEO) fluid flow in addition to the diffusion and dielectrophoretic migration was implemented. The established methods to calculate the ACEO fluid flow apply the slip velocity approximation, which considers the differences in fluid motion between both ends of thin double layers. Since the typical feature sizes of growing nanowires are much smaller then the thickness of the double layer, this simplification is not applicable in the present context. Thus, a spatially-resolved body force is calculated in the double layer region, which is employed in the Navier–Stokes equation to obtain the ACEO fluid flow. To this end, the structure of and the charge distribution within the double layer have been investigated by considering the ion transport in the solution under the influence of large electric fields by means of the Poisson–Nernst–Planck equation. To account for the finite-size of ions, a modified chemical potential was used.

A particular numerical difficulty was encountered in solving the exceptionally stiff set of partial differential equations owing to the multi-scale time and geometry modeling. To improve the convergence rate of the algorithm that determines the asymptotic, periodic ion distribution, a so-called convergence acceleration has been introduced. This methodology exploits the time-antisymmetry between the cations and anions and thereby returns the input data for the ACEO fluid flow calculation much faster.

The simulation of ion dynamics around nanoelectrodes for large applied electric fields revealed novel ion concentration patterns. Typically, during the half-period with an attractive electric field, the ion concentration up to about 1 nm from the electrode exceeds the bulk concentration value by several orders of magnitude. In the other half-period, the ions are repelled by a few hundred nanometers and the solution in proximity of the electrode is virtually free of this ion type. Through this interplay of the cations, anions, and the highly inhomogeneous electric field, a dynamic double layer with a very thin inner and an extremely wide outer layer is formed.

For these dynamic double layers the electric field and potential is evaluated. The electric field is found to consist of three contributions. The first is the external electric field, which can be observed in a charge-free dielectric or vacuum. The second contribution is the field screening, which is caused by the counter-charges in the double layer. The third contribution is the field enhancement, which ensures the Dirichlet boundary conditions of the electric potential. This means that for large charge densities close to the electrode, the electric field is significantly increased compared to the external electric field. Far from the electrode, in the bulk region, the electric field is strongly diminished.

Depending on the ion concentrations and the electrode curvature, three different frequency ranges can be distinguished. Below the lower transition frequency ω_{T1}, the ion concentration profiles are quasi-stationary. The rate at which the AC voltage changes is so slow that ions are in thermodynamic equilibrium at all times and a full field screening is observed. In this equilibrium situation, the net force on each ion is zero and consequently, no ACEO fluid flow can evolve.

Above the upper transition frequency ω_{T2}, the AC voltage changes so fast that the majority of ions cannot follow the excitation of the external electric field. Thus, at such high frequencies, the oscillation amplitude of the ion concentration and subsequently of the body force is extremely diminished. As a second consequence, the space charge density becomes sinusoidal with a phase shift of roughly 90° relative to the exciting AC electric field. Hence, the body force driving the ACEO fluid flow has a marginal time average compared to its already drastically reduced amplitude. The resulting ACEO fluid flow therefore shows oscillating directions and a relatively small time average. It should be mentioned that in this high frequency regime small deviations in the ion distribution (e.g. caused by numerical errors in the simulation) may already lead to noticeable changes in the time average of the fluid flow.

For intermediate frequencies between the lower and the upper transition frequency, feature-rich and highly nonlinear concentration profiles develop. The corresponding ACEO fluid flow exhibits a complex three dimensional flow pattern. The closed stream lines surround a semi-circular vortex line, which has a radius of several hundred nanometers. The stream lines have an extension of several micrometers and their orientations in the vicinity of the nanowire are inverse to the direction of nanowire growth.

Since the simulation of the dynamic double layer in the axisymmetric, two dimensional coordinate system is computationally highly expensive, a simplified calculation based on an one-dimensional solution of the Poisson–Nernst–Planck equation has been studied. In the intermediate frequency range, the obtained simulation results are in qualitative agreement with the solution of the full, two-dimensional problem. In the high frequency regime, the one-dimensional simplification fails due to the already mentioned high error sensitivity of the body force's time average.

The nanowire growth simulation based on diffusion, dielectrophoretic migration, and ACEO fluid flow as material transport mechanisms provided two major insights: first, for nanowires grown from complexes, the introduction of the ACEO fluid flow has a negligible effect on the nanowire growth velocity and morphology. This means the mismatch between the theoretical predictions and the experimental results remains. Second, nanowire growth by metal cluster assembly is highly affected by the additional ACEO fluid flow and the calculated growth velocity is increased to the experimental level.

In detail, it is found that due to the low diffusion coefficient of the metal clusters, the convective flux due to the ACEO fluid flow becomes the main transport mechanism for intermediate distances to the wire surface (micrometer range). In the proximity of the nanowire (up to about 200 nm), transport is dominated by the dielectrophoretic force, whereas in the long range (more than a few µm), diffusion is the major contribution to the particle flux. Since only the modeling for the case of a metal cluster assembly in the presence of an ACEO fluid flow is able to reproduce the experimental results quantitatively, this is considered as an evidence for both assumptions.

Based on the found mechanism for dielectrophoretic nanowire assembly, parameter optimizations to grow thinner and straighter nanowires are derived. To this end, a geometric scaling law of the Poisson–Nernst–Planck equation and the Navier–Stokes equation is considered, which aims at a miniaturization of existing nanowire growth protocols. Moreover, an optimization strategy on the basis of particle flux contributions is discussed. The resulting suggestions regarding the particle concentration and size, ion concentration, AC frequency and voltage, and electrode geometry design are presented in section 2.6.4.

The second major nanowire growth mechanism discussed in this work is the DENA scheme. As highlighted in section 2.7, the directed electrochemical nanowire assembly from cationic and anionic precursors obeys fundamentally different mechanisms. Since nanowires grown from anions have a thinner diameter and a much better morphology control, this methodology was investigated in more detail by the example of H_2PtCl_6-solutions. In this case, the anionic precursors are $[PtCl_6]^{2-}$-ions and their hydrolysis products.

The electrochemical conversion of these ions to metallic platinum at the electrode is induced by the electric field. For this process three alternative mechanisms have been proposed and their respective kinetics modeled. The first scenario considers the energy gain during a charge transfer process from the electrode to a platinum complex anion in a high electric field. This energy difference contributes to the free reaction enthalpy and thereby affects the reaction rate. In the second scenario, the provision of electrons through tunneling from the electrode to the complex is considered as the rate-limiting step. In the third alternative, the field-induced polarization of the complex ions is discussed. Through polarization of the platinum complex molecule, the binding energy of one particular bond is selectively weakened, which facilitates a thermally activated decomposition of the precursor. By comparing CP2K simulations with experiments, a quantitative agreement of the electric field threshold with the bond weakening mechanism is found. The other possible mechanisms could be ruled out, because they demonstrated an insufficient sensitivity towards the electric field strength.

The identification of the reaction kinetics allowed to deduce the principle behind the anionic DENA mechanism: negatively charged complexes need further electrons to be reduced in order to enable a metallic deposition. However, during the negative half wave, when electrons are available in excess, the complex anions are repelled from the electrode. Since the charge transfer can only happen in the vicinity of the electrode, this leaves only a small time frame for the reduction of the metal complex anion to take place before their concentration is depleted. To model the ion transport in the solution, the previously discussed Poisson–Nernst–Planck equation is reused.

In contrast to the previous application of ion transport simulations in the ACEO fluid flow calculations, in the case of nanowire growth by DENA the complex anions are consumed during the deposition reaction. Only the application of a numerical trick allows to lead back the DENA growth problem to the previously employed, blocking electrode boundary conditions. This procedure is a key prerequisite for the convergence acceleration and furthermore decouples the nanowire growth simulation from the numerically highly expensive retrieval of the stationary solution of the Poisson–Nernst–Planck equation. As such, this step is crucial for the computational feasibility of the DENA simulation.

The influence of the voltage signal shape is found to be of utmost importance for the growth velocity and the morphology of DENA-grown nanowires. The nanowire growth velocity distribution was monitored for a sine signal as well as a rectangular signal shape with a limited slew rate. To investigate the length and thickness growth of nanowires separately, the signal shape studies were carried out for one-dimensional spherical and cylindrical geometries. By comparing these results with experiments, the reaction rate parameters needed for the simulation could be estimated.

According to the simulation results, the straightest and thinnest nanowires grow when a rectangular signal is used in the DENA process. The mechanism driving this tendency is based on the large voltage slope of the signal: the sooner the field-assisted reaction of complex anions sets in, the more ions are available on the nanowire surface for a reduction. Since the electric field at the nanowire tip is the largest, the reaction is triggered there first. However, if the slew rate is too high, the growth is enabled on the whole nanowire surface and the nanowires grow substantially in thickness as well.

To avoid thickness growth and to improve diameter controllability of the nanowire, an innovative voltage signal shape has been constructed. The design rule specifies the valid parameter range for the RMS-voltage, the frequency and the slew rate. The designed signal supports nanowire growth from both electrodes simultaneously. As an additional feature, the proposed signal allows the tailoring to the employed precursor and the desired nanowire diameter.

Conclusion

In direct comparison, the DENA methodology yields straighter and thinner nanowires than the DEP nanowire assembly . The main reason is that DEP-grown nanowires are assembled from clusters and their size poses a strict minimum to the accessible nanowire diameter, but also promotes the branching of the nanowire. A reduction of the cluster size and ultimately the transition to a complex assembly would–in principle–lift the geometric diameter restrictions, but simultaneously it induces a more isotropic growth, which again leads to thicker nanowires. Therefore, an intermediate cluster size should be chosen to establish an optimal trade-off between the two effects. A further optimization of the nanowire growth can also happen by decreasing the cluster concentration and increasing the fluid flow velocity, which in turn requires a higher AC voltage, an increased electrolyte concentration, and an adjusted AC frequency. Unfortunately, the current progress in the experiments has already explored the majority of the optimization means so that the potential for further improvement is nearly exhausted. In contrast, for DENA nanowires with a diameter of around 20 nm the particle size limitation has not yet been reached. Therefore, by tailoring the reaction kinetics as described above, it should be possible to manufacture even thinner nanowires.

Due to the versatile applications of metallic nanowires the wish to transfer this technology to different metals arises. Since the DEP approach relies only on the polarizability of the clusters and the presence of an ACEO fluid flow, it can be immediately transferred to virtually any conductive cluster. For base metals it might be necessary to switch to water-free solvents to prevent their oxidization or dissolution. This vast flexibility of the DEP method allows for entirely new applications, like e.g. the co-deposition of different materials.

The substitution of the anionic precursor for the DENA approach comes with serious changes. The field-induced bond weakening, which provides the good controllability of the nanowire growth, requires chemically highly stable complex anions, which only in conjunction with high electric fields undergo a reaction. For platinum and other noble metals, chloro-complexes fulfill this need. However, for various applications also less noble metals like copper and indium are of great interest, as their oxides exhibit semiconducting properties. For these metals chloro-complexes do exist, but they decompose significantly in solution by thermal activation alone. This can be offset only to some extent by lowering the solution temperature. Particular for copper [16, 105] and indium [2] cation-based DENA protocols exist, but the resulting nanowires are much thicker and more branched than what is achievable by anion DENA. Therefore, to grow copper or indium nanowires with the anion DENA method, more stable anionic complexes are needed that have a stronger bond between the central ion and its ligands.

Good candidates for such strong-bonding ligands are polydentate organic anions like e.g. EDTA, EDDS, or NTA, as these ligands form stable complexes with most multivalent metal cations. If needed, the stability of the complexes can be adjusted through the pH of the solution. A second problem one faces when growing nanowires from less noble metals is the dissolving tendency, in particular during the positive voltage half wave. This can be overcome by either employing an inhibition agent, which coats the nanowire during the positive half wave and thereby prevents the dissolution, or by re-complexing cations created during the dissolution. For both approaches the aforementioned polydentate anions should be a good choice. Satisfying these prerequisites, it should be possible to control the nanowire growth by optimizing the voltage signal shape as discussed above.

For a mass-market application of metallic nanowires, a low-cost industrial-scale fabrication technique is needed. To this aim, the growth of nanowires from aqueous solutions is a highly promising technology as it combines a high yield with a minimal process complexity. An additional advantage of the method is that the nanowires grow from electrode to electrode, which spares an extra bonding step. Against this background, the insights on the growth mechanism of nanowires provided by this dissertation mark a major step towards the introduction of nanowire-based products in our everyday life.

Outlook

Future work could address improvements in the modeling to enhance the accuracy of model predictions, experimental studies to verify the modeling and to determine missing or refine existing parameters.

For example, the geometry of the growing nanowire tip is known only approximately. To investigate the tip shape more closely, it is advised to vary the nanowire tip shape until a length growth with a stationary tip geometry is observed. This investigation could also address the unsolved, related problems of wire nucleation, the coexistence of volume and surface wires, tip splitting, and the interruption of nanowire growth. However, this kind of analysis would require the consideration of asymmetric three-dimensional geometries, which strongly increases the computational costs.

A second issue for future works could be to improve the material laws used for the simulation. For example, in the present work, the dielectric constant was considered to be independent from the electric field strength and the ion concentration in the solution. An atomistic modeling of the solution could provide an effective modeling suitable for use in a continuum description.

The modeling of cation-based directed electrochemical nanowire assembly has not been considered in this work, since experimental evidence suggests that the anion-based counterpart yields straighter and thinner nanowires. Nevertheless, a better understanding of the relevant mechanism could result in a significantly improved control, which possibly allows to grow nanowires of comparable quality with the cation DENA process.

Moreover, the present work also raises experimental questions. On the basis of the DENA modeling for anions, a novel AC signal design to grow straight metallic nanowires with a controllable wire diameter has been proposed. The experimental verification of this approach is highly interesting. In particular, a parameter study with the target of identifying the activation energy and the reaction rate constant of the deposition reaction would add a high value, since it allows for a precise design of the nanowire growth protocols.

Similarly, it has been reasoned that employing polydentate organic anions as precursors should enable the growth of nanowires made from less noble metals in the same quality as for the platinum nanowires. To predict the growth of nanowires from these types of precursors more precisely, a systematic experimental investigation of the subject is urgently needed. Only through comparison of experimental and theoretical results, the idea can be developed further.

BIBLIOGRAPHY

[1] G De Micheli. *Nanosystems design and technology*. Springer, 2009.

[2] BN Flanders. Directed electrochemical nanowire assembly: precise nanostructure assembly via dendritic solidification. *Modern Physics Letters B*, **26**: 2012. doi: `10.1142/S0217984911300018`

[3] V Schmidt et al. Silicon nanowires: a review on aspects of their growth and their electrical properties. *Advanced Materials*, **21**: pp. 2681–2702, 2009. doi: `10.1002/adma.200803754`

[4] H Ditlbacher et al. Silver nanowires as surface plasmon resonators. *Physical Review Letters*, **95**: p. 257403, 2005. doi: `10.1103/PhysRevLett.95.257403`

[5] K Leosson et al. Long-range surface plasmon polariton nanowire waveguides for device applications. *Optics Express*, **14**: pp. 314–319, 2006. doi: `10.1364/OPEX.14.000314`

[6] BH Hong et al. Ultrathin single-crystalline silver nanowire arrays formed in an ambient solution phase. *Science*, **294**: pp. 348–351, 2001. doi: `10.1126/science.1062126`

[7] C Oon and J Thong. In situ nanowire growth for electrical interconnects. *Nanotechnology*, **15**: pp. 687–691, 2004. doi: `10.1088/0957-4484/15/5/048`

[8] G Schindler et al. Electrical characterization of copper interconnects with end-of-roadmap feature sizes. *Solid-State Electronics*, **47**: pp. 1233–1236, 2003. doi: `10.1016/S0038-1101(03)00042-X`

[9] F Favier et al. Hydrogen sensors and switches from electrodeposited palladium mesowire arrays. *Science*, **293**: pp. 2227–2231, 2001. doi: `10.1126/science.1063189`

[10] B Murray et al. Reversible resistance modulation in mesoscopic silver wires induced by exposure to amine vapor. *Analytical Chemistry*, **77**: pp. 5205–5214, 2005. doi: `10.1021/ac050636e`

[11] Y Im et al. Investigation of a single Pd nanowire for use as a hydrogen sensor. *Small*, **2**: pp. 356–358, 2006. doi: `10.1002/smll.200500365`

[12] C Li et al. Molecular detection based on conductance quantization of nanowires. *Applied Physics Letters*, **76**: pp. 1333–1335, 2000. doi: `10.1063/1.126025`

[13] A Bogozi et al. Molecular adsorption onto metallic quantum wires. *Journal of the American Chemical Society*, **123**: pp. 4585–4590, 2001. DOI: `10.1021/ja004335s`

[14] W Xing et al. A chemically-responsive nanojunction within a silver nanowire. *Nano Letters*, **12**: pp. 1729–1735, 2012. DOI: `10.1021/nl300427w`

[15] S Aravamudhan, NS Ramgir, and S Bhansali. Electrochemical biosensor for targeted detection in blood using aligned Au nanowires. *Sensors and Actuators B: Chemical*, **127**: pp. 29–35, 2007. DOI: `10.1016/j.snb.2007.07.008`

[16] C Schmädicke et al. P2. 4-Fabrication of copper nanowires from aqueous solution. *Proceedings SENSOR 2013*, pp. 720–723, 2013. DOI: `10.5162/sensor2013/P2.4`

[17] M Zheng et al. Ordered indium-oxide nanowire arrays and their photoluminescence properties. *Applied Physics Letters*, **79**: pp. 839–841, 2001. DOI: `10.1063/1.1389071`

[18] Y Cui et al. Nanowire nanosensors for highly sensitive and selective detection of biological and chemical species. *Science*, **293**: pp. 1289–1292, 2001. DOI: `10.1126/science.1062711`

[19] S Itoua and C Joachim. Fabrication and AFM characterization of gold wires of less than 50 nm width buried in a SiO_2 substrate. *Nanotechnology*, **3**: pp. 10–15, 1992. DOI: `10.1088/0957-4484/3/1/003`

[20] J Chen, H Hsu, and HN Lin. Fabrication of metal nanowires by atomic force microscopy nanoscratching and lift-off process. *Nanotechnology*, **16**: pp. 1112–1115, 2005. DOI: `10.1088/0957-4484/16/8/020`

[21] A Nerowski et al. Dielectrophoretic growth of platinum nanowires: concentration and temperature dependence of the growth velocity. *Langmuir*, **28**: pp. 7498–7504, 2012. DOI: `10.1021/la300302n`

[22] KD Hermanson et al. Dielectrophoretic assembly of electrically functional microwires from nanoparticle suspensions. *Science*, **294**: pp. 1082–1086, 2001. DOI: `10.1126/science.1063821`

[23] KH Bhatt and OD Velev. Control and modeling of the dielectrophoretic assembly of on-chip nanoparticle wires. *Langmuir*, **20**: pp. 467–476, 2004. DOI: `10.1021/la0349976`

[24] H Pohl. *Dielectrophoresis: the behavior of neutral matter in nonuniform electric fields*. Cambridge University Press, 1978.

[25] C Cheng et al. Self-assembly of metallic nanowires from aqueous solution. *Nano Letters*, **5**: pp. 175–178, 2005. DOI: `10.1021/nl048240q`

[26] JK Kawasaki and CB Arnold. Synthesis of platinum dendrites and nanowires via directed electrochemical nanowire assembly. *Nano Letters*, **11**: pp. 781–785, 2011. DOI: `10.1021/nl1039956`

[27] J Richter et al. Construction of highly conductive nanowires on a DNA template. *Applied Physics Letters*, **78**: pp. 536–538, 2001. DOI: `10.1063/1.1338967`

[28] M Reches and E Gazit. Casting metal nanowires within discrete self-assembled peptide nanotubes. *Science*, **300**: pp. 625–627, 2003. DOI: `10.1126/science.1082387`

[29] SR Nicewarner-Pena et al. Submicrometer metallic barcodes. *Science*, **294**: pp. 137–141, 2001. DOI: `10.1126/science.294.5540.137`

[30] E Menke et al. Lithographically patterned nanowire electrodeposition. *Nature Materials*, **5**: pp. 914–919, 2006. DOI: `10.1038/nmat1759`

[31] T Jung et al. One-dimensional metal structures at decorated steps. *Applied Physics A*, **61**: pp. 467–474, 1995. DOI: `10.1007/BF01540248`

[32] P Gambardella et al. One-dimensional metal chains on Pt vicinal surfaces. *Physical Review B*, **61**: pp. 2254–2262, 2000. DOI: `10.1103/PhysRevB.61.2254`

[33] MP Zach, KH Ng, and RM Penner. Molybdenum nanowires by electrodeposition. *Science*, **290**: pp. 2120–2123, 2000. DOI: `10.1126/science.290.5499.2120`

[34] J Shui and JC Li. Platinum nanowires produced by electrospinning. *Nano Letters*, **9**: pp. 1307–1314, 2009. DOI: `10.1021/nl802910h`

[35] SK Gray and T Kupka. Propagation of light in metallic nanowire arrays: finite-difference time-domain studies of silver cylinders. *Physical Review B*, **68**: p. 045415, 2003. DOI: `10.1103/PhysRevB.68.045415`

[36] X Xiong et al. Directed assembly of gold nanoparticle nanowires and networks for nanodevices. *Applied Physics Letters*, **91**: p. 063101, 2007. DOI: `10.1063/1.2763967`

[37] N Ranjan et al. Dielectrophoretic growth of metallic nanowires and microwires: theory and experiments. *Langmuir*, **26**: pp. 552–559, 2009. DOI: `10.1021/la902026e`

[38] N Ranjan, H Vinzelberg, and M Mertig. Growing one-dimensional metallic nanowires by dielectrophoresis. *Small*, **2**: pp. 1490–1496, 2006. DOI: `10.1002/smll.200600350`

[39] B Ozturk et al. Single-step growth and low resistance interconnecting of gold nanowires. *Nanotechnology*, **18**: p. 175707, 2007. DOI: `10.1088/0957-4484/18/17/175707`

[40] B Ozturk, I Talukdar, and B Flanders. Synthesis of platinum dendrites and nanowires via directed electrochemical nanowire assembly. *Nanotechnology*, **18**: p. 365302, 2007. DOI: `10.1088/0957-4484`

[41] B Ozturk. *Structural and transport properties of directly assembled nanowires*. ProQuest, 2007.

[42] J Newman and KE Thomas-Alyea. *Electrochemical systems, 3rd edition*. John Wiley & Sons, 2004.

[43] P Debye and E Hückel. The theory of electrolytes. I. Lowering of freezing point and related phenomena. *Physikalische Zeitschrift*, **24**: pp. 185–206, 1923.

[44] MZ Bazant, K Thornton, and A Ajdari. Diffuse-charge dynamics in electrochemical systems. *Physical Review E*, **70**: p. 021506, 2004. DOI: `10.1103/PhysRevE.70.021506`

[45] MZ Bazant et al. Towards an understanding of induced-charge electrokinetics at large applied voltages in concentrated solutions. *Advances in Colloid and Interface Science*, **152**: pp. 48–88, 2009. DOI: `10.1016/j.cis.2009.10.001`

[46] L Olesen, M Bazant, and H Bruus. Strongly nonlinear dynamics of electrolytes in large AC voltages. *Physical Review E*, **82**: p. 011501, 2010. DOI: `10.1103/PhysRevE.82.011501`

[47] Y Suh and S Kang. Asymptotic analysis of ion transport in a nonlinear regime around polarized electrodes under AC. *Physical Review E*, **77**: p. 031504, 2008. DOI: `10.1103/PhysRevE.77.031504`

[48] Y Suh and S Kang. Numerical prediction of AC electro-osmotic flows around polarized electrodes. *Physical Review E*, **79**: p. 046309, 2009. DOI: `10.1103/PhysRevE.79.046309`

[49] MZ Bazant. "AC electro-osmotic flow" in: *Encyclopedia of Microfluidics and Nanofluidics*. Springer, 2008. Pp. 8–14

[50] A Ramos et al. AC electric-field-induced fluid flow in microelectrodes. *Journal of Colloid and Interface Science*, **217**: pp. 420–422, 1999. DOI: `10.1006/jcis.1999.6346`

[51] NG Green et al. Fluid flow induced by nonuniform AC electric fields in electrolytes on microelectrodes. I. Experimental measurements. *Physical Review E*, **61**: pp. 4011–4018, 2000. DOI: `10.1103/PhysRevE.61.4011`

[52] NG Green et al. Fluid flow induced by nonuniform AC electric fields in electrolytes on microelectrodes. III. Observation of streamlines and numerical simulation. *Physical Review E*, **66**: p. 026305, 2002. DOI: `10.1103/PhysRevE.66.026305`

[53] A Ajdari. Pumping liquids using asymmetric electrode arrays. *Physical Review E*, **61**: pp. 45–48, 2000. DOI: `10.1103/PhysRevE.61.R45`

[54] NG Green et al. Electrothermally induced fluid flow on microelectrodes. *Journal of Electrostatics*, **53**: pp. 71–87, 2001. DOI: `10.1016/S0304-3886(01)00132-2`

[55] A Ramos et al. Pumping of liquids with traveling-wave electroosmosis. *Journal of Applied Physics*, **97**: pp. 084906–084906, 2005. DOI: `10.1063/1.1873034`

[56] A Castellanos et al. Electrohydrodynamics and dielectrophoresis in microsystems: scaling laws. *Journal of Physics D: Applied Physics*, **36**: pp. 2584–2597, 2003. DOI: `10.1088/0022-3727/36/20/023`

[57] LH Olesen, H Bruus, and A Ajdari. AC electrokinetic micropumps: the effect of geometrical confinement, Faradaic current injection, and nonlinear surface capacitance. *Physical Review E*, **73**: p. 056313, 2006. DOI: `10.1103/PhysRevE.73.056313`

[58] A Brown, C Smith, and A Rennie. Pumping of water with AC electric fields applied to asymmetric pairs of microelectrodes. *Physical Review E*, **63**: p. 016305, 2000. DOI: `10.1103/PhysRevE.63.016305`

[59] N Loucaides, A Ramos, and G Georghiou. Dielectrophoretic and AC electroosmotic trapping of DNA: numerical simulation incorporating fluid dynamics and steric particle effects. *Journal of Electrostatics*, **69**: pp. 111–118, 2011. DOI: `10.1016/j.elstat.2011.01.004`

[60] WH Yeo et al. Rapid detection of Mycobacterium tuberculosis cells by using microtip-based immunoassay. *Analytical and Bioanalytical Chemistry*, **393**: pp. 1593–1600, 2009. DOI: `10.1007/s00216-008-2591-x`

[61] A González et al. Fluid flow induced by nonuniform AC electric fields in electrolytes on microelectrodes. II. A linear double-layer analysis. *Physical Review E*, **61**: pp. 4019–4028, 2000. DOI: `10.1103/PhysRevE.61.4019`

[62] JB Freund. Electro-osmosis in a nanometer-scale channel studied by atomistic simulation. *The Journal of Chemical Physics*, **116**: p. 2194, 2002. DOI: `http://dx.doi.org/10.1063/1.1431543`

[63] MV FEDOROV and AA KORNYSHEV. Towards understanding the structure and capacitance of electrical double layer in ionic liquids. *Electrochimica Acta*, **53**: pp. 6835–6840, 2008. DOI: `10.1016/j.electacta.2008.02.065`

[64] R QIAO and N ALURU. Ion concentrations and velocity profiles in nanochannel electroosmotic flows. *The Journal of Chemical Physics*, **118**: p. 4692, 2003. DOI: `10.1063/1.1543140`

[65] L ELDING. Stepwise dissociation of tetrachloroplatinate (II) ion in aqueous solution. 6. Rates of formation and equilibria of chloro aqua complexes of platinum(II). *Acta Chemica Scandinavica*, **24**: pp. 1527–1540, 1970. DOI: `10.3891/acta.chem.scand.24-1331`

[66] L ELDING. Stabilities of platinum (II) chloro and bromo complexes and kinetics for anation of the tetraaquaplatinum (II) ion by halides and thiocyanate. *Inorganica Chimica Acta*, **28**: pp. 255–262, 1978. DOI: `10.1016/S0020-1693(00)87444-7`

[67] L WU, B SCHWEDERSKI, and D MARGERUM. Stepwise hydrolysis kinetics of tetrachloroplatinate (II) in base. *Inorganic Chemistry*, **29**: pp. 3578–3584, 1990. DOI: `10.1021/ic00343a054`

[68] JV QUAGLIANO and L SCHUBERT. The trans effect in complex inorganic compounds. *Chemical Reviews*, **50**: pp. 201–260, 1952. DOI: `10.1021/cr60156a001`

[69] S SHIRONITA et al. Preparation of nano-sized platinum metal catalyst using photo-assisted deposition method on mesoporous silica including single-site photocatalyst. *Applied Surface Science*, **254**: pp. 7604–7607, 2008. DOI: `10.1016/j.apsusc.2008.01.120`

[70] A NEROWSKI et al. Bottom-up synthesis of ultrathin straight platinum nanowires: electric field impact. *Nano Research*, **6**: pp. 303–311, 2013. DOI: `10.1007/s12274-013-0303-0`

[71] B SHELIMOV et al. Application of NMR to interfacial coordination chemistry: A 195Pt NMR study of the interaction of hexachloroplatinic acid aqueous solutions with alumina. *Journal of the American Chemical Society*, **121**: pp. 545–556, 1999. DOI: `10.1021/ja982515k`

[72] W HAYNES, D LIDE, and T BRUNO. *CRC Handbook of Chemistry and Physics*. CRC Handbook of Chemistry and Physics CRC Press, 2012.

[73] C KIELY et al. Spontaneous ordering of bimodal ensembles of nanoscopic gold clusters. *Nature*, **396**: pp. 444–446, 1998. DOI: `10.1038/24808`

[74] P ATKINS and A HÖPFNER. *Physikalische Chemie*. Vol. 1 Wiley VCH Verlag GmbH, 2002.

[75] MK BUCZKOWSKA. *Synthesis, characterization, antitumor and antimicrobial activities of heterocyclic transition metal complexes*. PhD thesis. Ernst-Moritz-Arndt-Universität Greifswald, 2011.

[76] D LIDE. *Handbook of chemistry and physics*. CRC Press, 1995.

[77] THE NATIONAL INSTITUTE OF STANDARDS AND TECHNOLOGY (NIST) *NIST Standard Reference Database* 2011 URL: `http://webbook.nist.gov/`

[78] Y MARCUS. A simple empirical model describing the thermodynamics of hydration of ions of widely varying charges, sizes, and shapes. *Biophysical Chemistry*, **51**: pp. 111–127, 1994. DOI: `10.1016/0301-4622(94)00051-4`

[79] B GIERHART et al. Frequency dependence of gold nanoparticle superassembly by dielectrophoresis. *Langmuir*, **23**: pp. 12450–12456, 2007. DOI: `10.1021/la701472y`

[80] GS FULCHER. Analysis of recent measurements of the viscosity of glasses. *Journal of the American Ceramic Society*, **8**: pp. 339–355, 1925. DOI: `10.1111/j.1151-2916.1925.tb16731.x`

[81] J HOLZWARTH and L STROHMAIER. Einfluß der Konzentration von Kationen auf die Geschwindigkeit der Elektronenübertragung zwischen Metallkomplexionen. *Berichte der Bunsengesellschaft für physikalische Chemie*, **77**: pp. 1145–1151, 1973. DOI: `10.1002/bbpc.19730771220`

[82] R CAMPION et al. Kinetics of electron exchange between hexacyanoferrate (II) and (III) ions. *Inorganic Chemistry*, **6**: pp. 672–681, 1967. DOI: `10.1021/ic50050a009`

[83] L PETER et al. The influence of alkali metal cations on the rate of the Fe (CN) 64-/Fe (CN) 63-electrode process. *Journal of Electroanalytical Chemistry*, **71**: pp. 31–50, 1976. DOI: `10.1016/S0022-0728(76)80288-4`

[84] P PHAM et al. "Numerical simulation of the electrical double layer based on the Poisson-Boltzmann models for AC electroosmosis flows" in: *Excerpt from the Proceedings of the COMSOL Users Conference 2007, Grenoble*. 2007.

[85] MS KILIC, MZ BAZANT, and A AJDARI. Steric effects in the dynamics of electrolytes at large appplied voltages. I. Double-layer charging. *Physical Review E*, **75**: p. 021502, 2007. DOI: `10.1103/PhysRevE.75.021502`

[86] J BIKERMAN. XXXIX. Structure and capacity of electrical double layer. *Philosophical Magazine Series 7*, **33**: pp. 384–397, 1942. DOI: `10.1080/14786444208520813`

[87] GESTIS DATABASE *Potassium chloride* URL: `http://gestis.itrust.de/` (visited on 03/13/2013)

[88] A STOGRYN. Equations for calculating the dielectric constant of saline water (correspondence). *IEEE Transactions on Microwave Theory and Techniques*, **19**: pp. 733–736, 1971. DOI: `10.1109/TMTT.1971.1127617`

[89] C YEH and ML BERKOWITZ. Dielectric constant of water at high electric fields: molecular dynamics study. *The Journal of Chemical Physics*, **110**: pp. 7935–7942, 1999. DOI: `10.1063/1.478698`

[90] E GONGADZE et al. Spatial variation of permittivity of an electrolyte solution in contact with a charged metal surface: a mini review. *Computer Methods in Biomechanics and Biomedical Engineering*, pp. 1–18, 2012. DOI: `10.1080/10255842.2011.624769`

[91] J LÓPEZ-GARCÍA, M ARANDA-RASCÓN, and J HORNO. Electrical double layer around a spherical colloid particle: the excluded volume effect. *Journal of Colloid and Interface Science*, **316**: pp. 196–201, 2007. DOI: `10.1016/j.jcis.2007.07.054`

[92] I BORUKHOV, D ANDELMAN, and H ORLAND. Steric effects in electrolytes: a modified Poisson–Boltzmann equation. *Physical Review Letters*, **79**: pp. 435–438, 1997. DOI: `10.1103/PhysRevLett.79.435`

[93] CW OUTHWAITE, LB BHUIYAN, and S LEVINE. Theory of the electric double layer using a modified Poisson–Boltzman equation. *Journal of the Chemical Society, Faraday Transactions 2*, **76**: pp. 1388–1408, 1980. DOI: `10.1039/F29807601388`

[94] JG SIMMONS. Generalized formula for the electric tunnel effect between similar electrodes separated by a thin insulating film. *Journal of Applied Physics*, **34**: pp. 1793–1803, 1963. DOI: `10.1063/1.1702682`

[95] CP2K PROJECT *About CP2K Open Source Molecular Dynamics* June 2015 URL: `http://www.cp2k.org/`

[96] HJ G HENKELMAN G JÓHANNESSON. Progress on theoretical chemistry and physics. *Kluwer Academic Publishers*, pp. 269–300, 2000.

[97] A NEROWSKI et al. Effect of waveform of AC voltage on morphology and crystallinity of electrochemically assembled platinum nanowires. *Langmuir*, **30**: pp. 5655–5661, 2014. DOI: `10.1021/la5002946`

[98] J CÉA. Approximation variationnelle des problèmes aux limites. *Annales de l'Institut Fourier*, **14**: pp. 345–444, 1964.

[99] PC HAMMER, OJ MARLOWE, and AH STROUD. Numerical integration over simplexes and cones. *Mathematical Tables and Other Aids to Computation*, **10**: pp. 130–137, 1956.

[100] K PAN. "Correction of Gauss Legendre quadrature over a triangle" in: *Multimedia Technology (ICMT), 2011 International Conference on*. IEEE 2011. Pp. 5787–5790 DOI: `10.1109/ICMT.2011.6002583`

[101] DDF GRIFFITHS and DDJ HIGHAM. *Numerical methods for ordinary differential equations: initial value problems*. Springer, 2010.

[102] K ATKINSON, W HAN, and DE STEWART. *Numerical solution of ordinary differential equations*. vol. 108 John Wiley & Sons, 2011.

[103] J BUTCHER. General linear methods for ordinary differential equations. *Mathematics and Computers in Simulation*, **79**: pp. 1834–1845, 2009. DOI: `10.1016/j.matcom.2007.02.006`

[104] F ILINCA and JF HÉTU. Finite element solution of three-dimensional turbulent flows applied to mold-filling problems. *International Journal for Numerical Methods in Fluids*, **34**: pp. 729–750, 2000. DOI: `10.1002/1097-0363(20001230)34:8<729::AID-FLD79>3.0.CO;2-P`

[105] C SCHMAEDICKE et al. Copper nanowires synthesis by directed electrochemical nanowire assembly. *RSC Advances*, 2014. DOI: `10.1039/C4RA04853A`

[106] M POETSCHKE et al. Modeling graphene-based nanoelectromechanical devices. *Physical Review B*, **81**: p. 193404, 2010. DOI: `10.1103/PhysRevB.81.193404`

[107] M POETSCHKE. "Multi-scale simulations of mechanical properties and growth mechanisms of nanowires" in: *1st Workshop of the ECEMP International Graduate School*. 2010. Pp. 71–79

[108] T KAWAI et al. Mechanically-induced transport switching effect in graphene-based nanojunctions. *Physical Review B*, **83**: p. 241405, 2011. DOI: `10.1103/PhysRevB.83.241405`

[109] MH RÜMMELI et al. Graphene: Piecing it together. *Advanced Materials*, **23**: pp. 4471–4490, 2011.

[110] C ROCHA et al. "1 Tailoring the Physical Properties of Graphene" in: *Graphene: Synthesis and Applications*. CRC Press, 2011. Pp. 1–25

[111] M POETSCHKE. "Simulation of fluid flow during nanowire growth from solution" in: *2nd Workshop of the ECEMP International Graduate School*. 2011. Pp. 163–171

[112] M Poetschke. "Simulation of platinum nanowire growth from solution: a comparative analysis of growth velocities" in: *3rd Workshop of the ECEMP International Graduate School*. 2012. Pp. 179–188

[113] M Poetschke, M Bobeth, and G Cuniberti. Ion fluxes and electro-osmotic fluid flow in electrolytes around a metallic nanowire tip under large applied AC voltage. *Langmuir*, **29**: pp. 11525–11534, 2013. doi: `10.1021/la401928m`

[114] C Schmadicke et al. "A novel electrochemical synthesis route for copper nanowire formation" in: *Sensors, 2013 IEEE*. IEEE 2013. Pp. 1–4 doi: `10.1109/ICSENS.2013.6688365`

[115] B Mortazavi, M Pötschke, and G Cuniberti. Multiscale modeling of thermal conductivity of polycrystalline graphene sheets. *Nanoscale*, **6**: pp. 3344–3352, 2014. doi: `10.1039/C3NR06388G`

ACKNOWLEDGEMENT

Zum Abschluss meiner Dissertation ist es mein Anliegen mich bei Allen zu bedanken, die mir geholfen haben, dieses Ziel zu erreichen. Einige Personen haben diesen Weg jedoch besonders intensiv mit begleitet und ich möchte Sie daher an dieser Stelle hervorheben.

Zuerst natürlich Dir, Giovanni, als meinem Doktorvater, gilt mein besonderer Dank für die gute Betreuung und stete Unterstützung während der gesamten Zeit.

Weiterhin danke ich Dir, Manfred, für die zahlreichen Diskussionen, in denen so manch unerklärliches Phänomen dann letztlich doch verständlich wurde. Auch die tatkräftige Unterstützung beim Konzipieren und (Um-)Schreiben der Paper hat mir sehr geholfen.

Für die fruchtvolle Zusammenarbeit und für die vielen Stunden im Labor, die Ihr für die gemeinsame Sache investiert habt, danke ich Euch, Cindy und Alexander.

Unvergessen sind auch die vielen gemeinsamen Stunden mit den Büro- und Sysadminkollegen, Robert, Hagen und Alexander. Die zahlreichen Fachdiskurse und insbesondere das offene Ohr, wenn es galt Fehler zu finden, waren mir eine äußerst wertvolle Hilfe.

Für Deine Unterstützung bei den DFT und CP2K Berechungen bin ich Dir dankbar, Arezoo.

Quirina und Lokamani, so manch kniffeliger Satz der Arbeit hätte es ohne Eure Hilfe vermutlich nie in ein einigermaßen verständliches Englisch geschafft; vielen Dank dafür.

I also want to thank you, Bohayra, for bringing me in touch with this totally different research and publication culture of yours. Working together with you was a truely memorable experience.

Dem Zentrum für Informationsdienste und Hochleistungsrechnen (ZIH) der TU Dresden danke ich für die zur Verfügung gestellte Rechenzeit.

Ferner möchte ich dem European Centre for Emerging Materials and Processes (ECEMP) für das erhaltene Stipendium und die exzellenten Forschungsrahmenbedingungen danken. Natürlich danke ich auch den organisatorischen Köpfen hinter der Internationalen Graduiertenschule, Prof. Gude und Dr. Ottow, für ihre gute Arbeit.

Bei den Mitstreitern aus der Internationalen Gradiertenschule, vor allem bei Dir, Carsten, möchte ich mich für die schöne gemeinsame Zeit bedanken, insbesondere auch außerhalb des Büros.

Besonders und von ganzem Herzen danke ich meiner Familie und meiner Lebensgefährtin Andrea für die seelisch-moralische Unterstützung, die ständige Motivation, ihr Verständnis und ihre Geduld, auch in den schwierigen Phasen.

LIST OF PUBLICATIONS

M Poetschke, C Rocha, LF Torres, S Roche, and G Cuniberti. Modeling graphene-based nanoelectromechanical devices. *Physical Review B*, **81**: p. 193404, 2010. DOI: `10.1103/PhysRevB.81.193404`

M Poetschke. "Multi-scale simulations of mechanical properties and growth mechanisms of nanowires" in: *1st Workshop of the ECEMP International Graduate School*. 2010. Pp. 71–79

T Kawai, M Poetschke, Y Miyamoto, C Rocha, S Roche, and G Cuniberti. Mechanically-induced transport switching effect in graphene-based nanojunctions. *Physical Review B*, **83**: p. 241405, 2011. DOI: `10.1103/PhysRevB.83.241405`

MH Rümmeli, CG Rocha, F Ortmann, I Ibrahim, H Sevincli, F Börrnert, J Kunstmann, A Bachmatiuk, M Pötschke, M Shiraishi, et al. Graphene: Piecing it together. *Advanced Materials*, **23**: pp. 4471–4490, 2011.

C Rocha, M Rümmeli, I Ibrahim, H Sevincli, F Börrnert, J Kunstmann, A Bachmatiuk, M Pötschke, W Li, S Makharza, et al. "1 Tailoring the Physical Properties of Graphene" in: *Graphene: Synthesis and Applications*. CRC Press, 2011. Pp. 1–25

M Poetschke. "Simulation of fluid flow during nanowire growth from solution" in: *2nd Workshop of the ECEMP International Graduate School*. 2011. Pp. 163–171

A Nerowski, M Poetschke, M Bobeth, J Opitz, and G Cuniberti. Dielectrophoretic growth of platinum nanowires: concentration and temperature dependence of the growth velocity. *Langmuir*, **28**: pp. 7498–7504, 2012. DOI: `10.1021/la300302n`

M Poetschke. "Simulation of platinum nanowire growth from solution: a comparative analysis of growth velocities" in: *3rd Workshop of the ECEMP International Graduate School*. 2012. Pp. 179–188

M Poetschke, M Bobeth, and G Cuniberti. Ion fluxes and electro-osmotic fluid flow in electrolytes around a metallic nanowire tip under large applied AC voltage. *Langmuir*, **29**: pp. 11525–11534, 2013. doi: `10.1021/la401928m`

C Schmadicke, M Potschke, L David, and G Cuniberti. "A novel electrochemical synthesis route for copper nanowire formation" in: *Sensors, 2013 IEEE*. IEEE 2013. Pp. 1–4 doi: `10.1109/ICSENS.2013.6688365`

A Nerowski, M Pötschke, U Wiesenhütter, J Nicolai, U Cikalova, A Dianat, A Erbe, J Opitz, M Bobeth, L Baraban, and G Cuniberti. Effect of waveform of AC voltage on morphology and crystallinity of electrochemically assembled platinum nanowires. *Langmuir*, **30**: pp. 5655–5661, 2014. doi: `10.1021/la5002946`

B Mortazavi, M Pötschke, and G Cuniberti. Multiscale modeling of thermal conductivity of polycrystalline graphene sheets. *Nanoscale*, **6**: pp. 3344–3352, 2014. doi: `10.1039/C3NR06388G`

C Schmaedicke, M Poetschke, LD Renner, L Baraban, M Bobeth, and G Cuniberti. Copper nanowires synthesis by directed electrochemical nanowire assembly. *RSC Advances*, 2014. doi: `10.1039/C4RA04853A`